HIGH TEMPERATURE CORROSION OF ADVANCED CERAMIC MATERIALS FOR HOT GAS FILTERS AND HEAT EXCHANGERS

C. E. Crossland, D. L. Shelleman, K. E. Spear and R. E. Tressler
The Pennsylvania State University
226 Steidle Bldg
University Park, PA 16802

ABSTRACT

A vertical flow-through furnace has been built to study the effect of corrosion on the morphology and mechanical properties of ceramic hot gas filters. Sections of 3M Type 203 and DuPont Lanxide SiC-SiC filter tubes were sealed at one end and suspended in the furnace while being subjected to a simulated coal combustion environment at 870°C. X-ray diffraction and electron microscopy is used to identify phase and morphology changes due to corrosion while burst testing determines the loss of mechanical strength after exposure to the combustion gases. Additionally, a thermodynamic database of gaseous silicon compounds is currently being established so that calculations can be made to predict important products of the reaction of the environment with the ceramics. These thermodynamic calculations provide useful information concerning the regimes where the ceramic may be degraded by material vaporization.

To verify the durability and predict lifetime performance of ceramic heat exchangers in coal combustion environments, long-term exposure testing of stressed (internally pressurized) tubes must be performed in actual coal combustion environments. We have designed a system that will internally pressurize 2" OD by 48" long ceramic heat exchanger tubes to a maximum pressure of 200 psi while exposing the outer surface of the tubes to coal combustion gas at the Combustion and Environmental Research Facility (CERF) at the Pittsburgh Energy and Technology Center (PETC). Water-cooled, internal o-ring pressure seals were designed to accommodate the existing 6" by 6" access panels of the CERF. Tubes will be exposed for up to a maximum of 500 hours at temperatures of 2500 and 2600°F with an internal pressure of 200 psi. If the tubes survive, their retained strength will be measured using the high temperature tube burst test facility at Penn State University. Fractographic analysis will be performed to identify the failure source(s) for the tubes.

INTRODUCTION

This project consists of two separate study areas. Part 1 details the corrosion and resulting changes in the mechanical properties of candidate hot gas filters exposed to a flow-through type combustion environment. Additionally, thermochemical modeling will be employed in an effort to predict system responses under various environments. ChemSage[1] can be used to study the phase equilibrium of systems over numerous pressure and temperature ranges. The objective for Part 2 of this program is to access the long-term (500 hours) durability of candidate ceramic heat exchangers subjected to the combined effects of stress (internal gas pressure of 200 psi) and hot corrosion via coal combustion environment.

EXPERIMENTAL PROCEDURE

Based on results from earlier flow-over tests on 3M's Type 203 filters (SiC matrix-Nextel fiber composite) and DuPont Lanxide's SiC-SiC composite filters with Nicalon fibers, a reactor was developed to allow for flow-through experiments on 18" sealed sections of filters coated with ash collected at the Tidd plant. The vertical flow-through reactor (Figure 1) consists of a 6 inch I.D. SiC furnace tube fixed at the exhaust end by a stainless steel cylinder to support the filter sections. The inlet gas flow of 30% O_2, 15% H_2O, 3300 ppm SO_2, 1100 ppm HCl, 10 ppm NaCl and 55% air is forced to flow through the filter material. These tests are carried out with the inlet gas flow rate between 1 and 5 slm at temperatures up to 870°C and time periods of 50, 100 and 200 hours. After exposure to the corrosive environment, any phase or morphological changes will be studied with x-ray diffraction and scanning electron microscopy. The residual strength of the filters will be measured by internal pressurized burst testing.

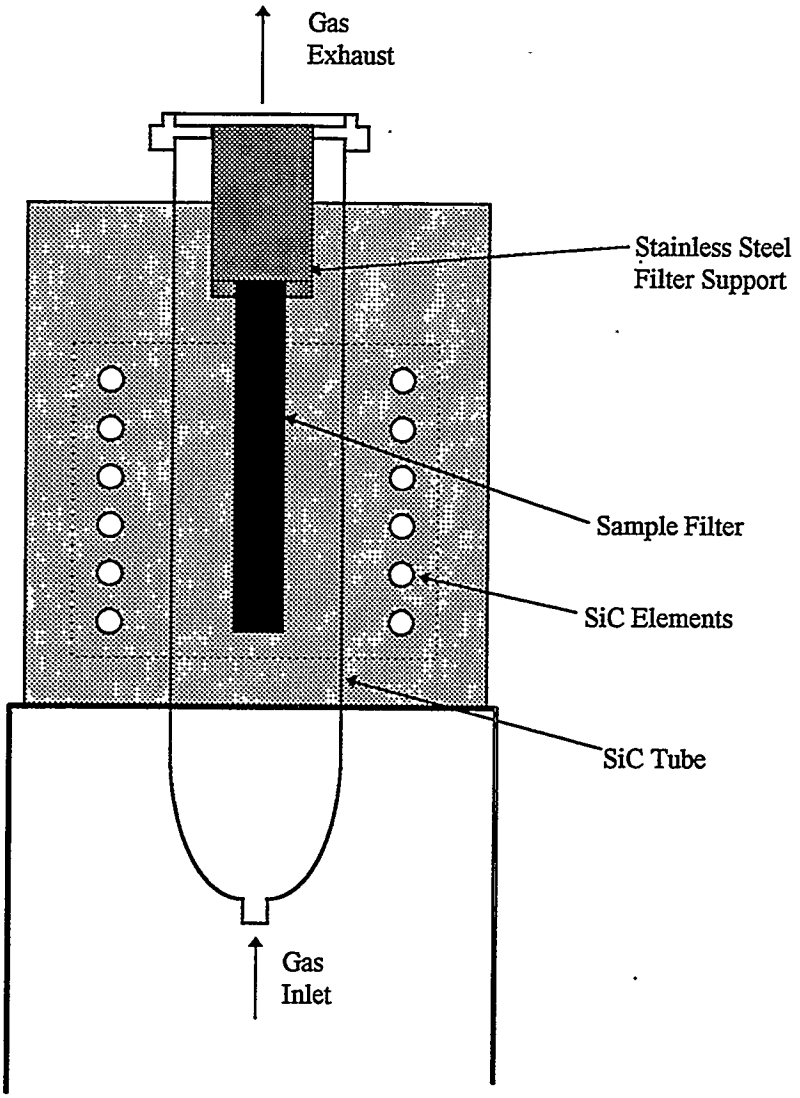

Figure 1: Vertical flow-through reactor designed for corrosion studies of ceramic filters

A database has been set up for the Si-O-H-Cl-Na-C-N-Ar system by incorporating thermodynamic data from MICROTHERM[2] and Allendorf et al.[3] By utilizing this database with ChemSage, the reaction of SiC with oxidizing and reducing atmospheres can be predicted over a range of temperatures and at extended pressures not easily duplicated by experiment.

Part II of this program began in February of this year. The objective of the program is to assess the durability of candidate ceramic heat exchangers subjected to the combined effects of stress and hot corrosion. This will be accomplished by designing a system that will internally pressurize ceramic tubes while the outer surface is exposed to coal combustion gases. A pressure system has been designed to fit the existing 6" by 6" access panels of the Combustion and Environmental Research Facility (CERF) at the Pittsburgh Energy and Technology Center (PETC) (see Figure 2). Two open-ended tubes (2" OD by 1.625" ID by 48" in length) will be exposed at the same time for a maximum of 500 hours at temperatures ranging from 2200 to 2600°F with an internal pressure of 200 psig N_2. If the tubes survive the exposure to coal combustion, their retained strength will be measured using the Tube Burst Test Apparatus[4] at Penn State University. Fractographic analysis will be performed on the tube fragments to identify, if possible, the source(s) of failure for the tubes.

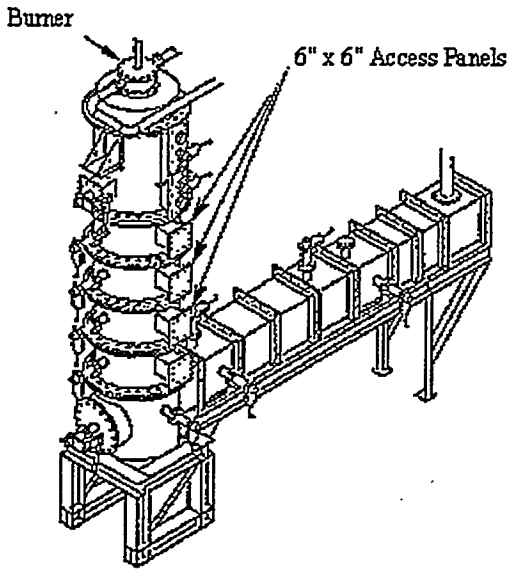

Figure 2: A system is being designed to fit the existing 6" by 6" access panels of the CERF at PETC to internally pressurize (200 psig of N_2 gas) 2" OD by 48" long ceramic tubes while the outer surface is exposed to coal combustion gases at temperatures ranging from 2200 to 2600°F for up to 500 hours

RESULTS

Work thus far can be separated into two sections: 1) experimental results from initial flow-through test and 2) thermochemical modeling of pressurized fluidized bed combustors (PFBC). The results from the flow-through test include x-ray diffraction, scanning electron microscopy and internal pressurized burst testing. The corrosion of SiC was studied in oxidizing, reducing and carbonizing conditions by thermochemical modeling of existing PFBCs.

Flow-Through Test

An initial flow-through test has been conducted on a section of 3M Type 203 filter at 870°C and 5 slm for 50 hours. Figure 3 contains a scanning electron micrograph of the inner surface of the filtering layer of the as-received 3M filter. The filtering layer consists of a mat of chopped Nextel 312 fibers with a CVI layer of SiC. The fiber surfaces appear smooth with spherical features on the order of 5 microns. Figure 4 shows the inner surface of the filtering layer after exposure. The mat now consists of 1 micron diameter fibrils extending from the chopped fiber surface.

Constant volume x-ray powder diffraction of the filtering layer of the as-received 3M filter revealed the presence of alpha SiC. The SiC is likely a mix of polytypes but the x-ray pattern most closely matches that of the 15R polytype (JCPDS file number 39-1196). X-ray on the exposed 3M filtering layer revealed an amorphous or glassy component and several low-angle peaks in addition to the SiC peaks found in the as-received 3M filter (Figure 5). The low-angle peaks seem to indicate the presence of trace amounts of tridymite.

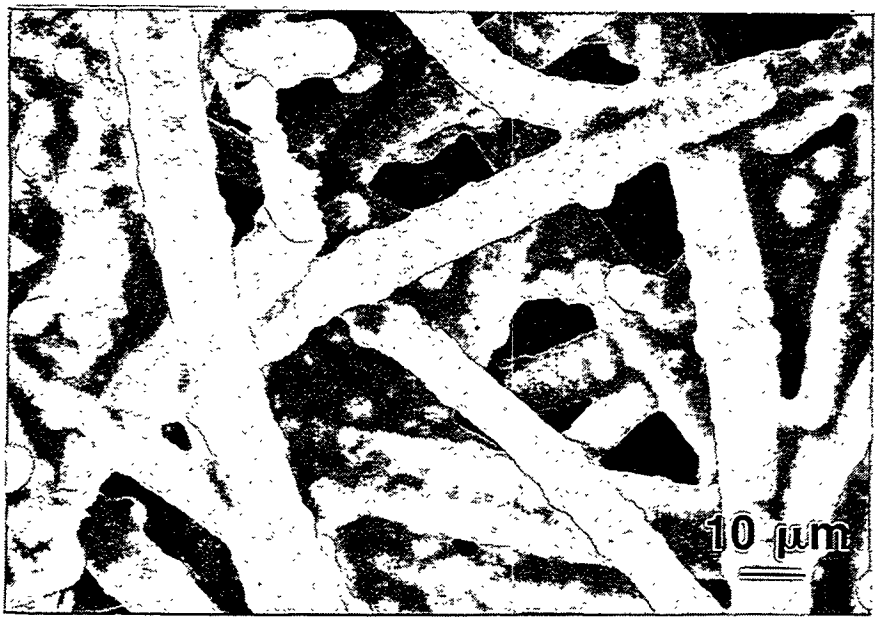

Figure 3: Filtering Layer of 3M Type 203 Filter As-Received

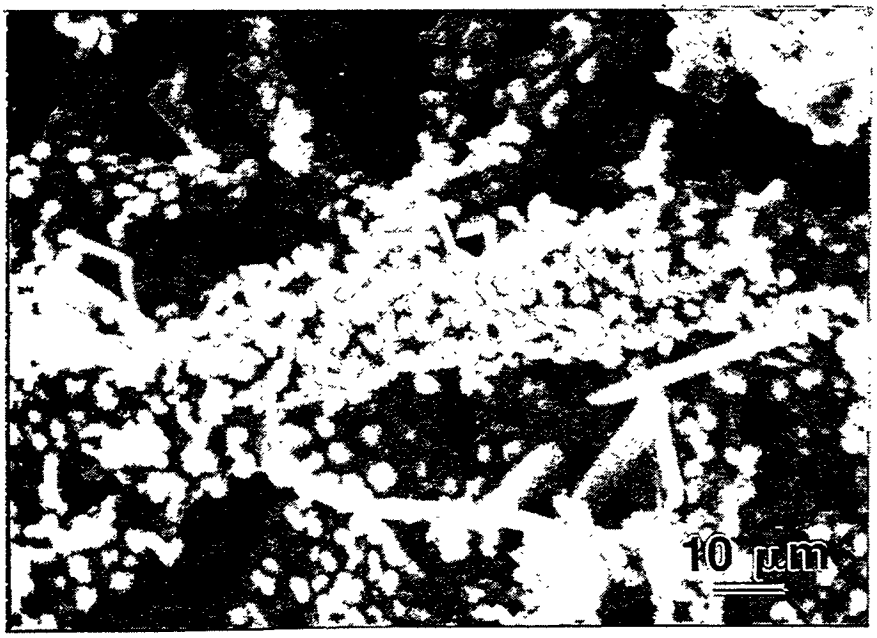

Figure 4: Filtering Layer of 3M Type 203 Filter After Exposure at 870°C for 50 Hours

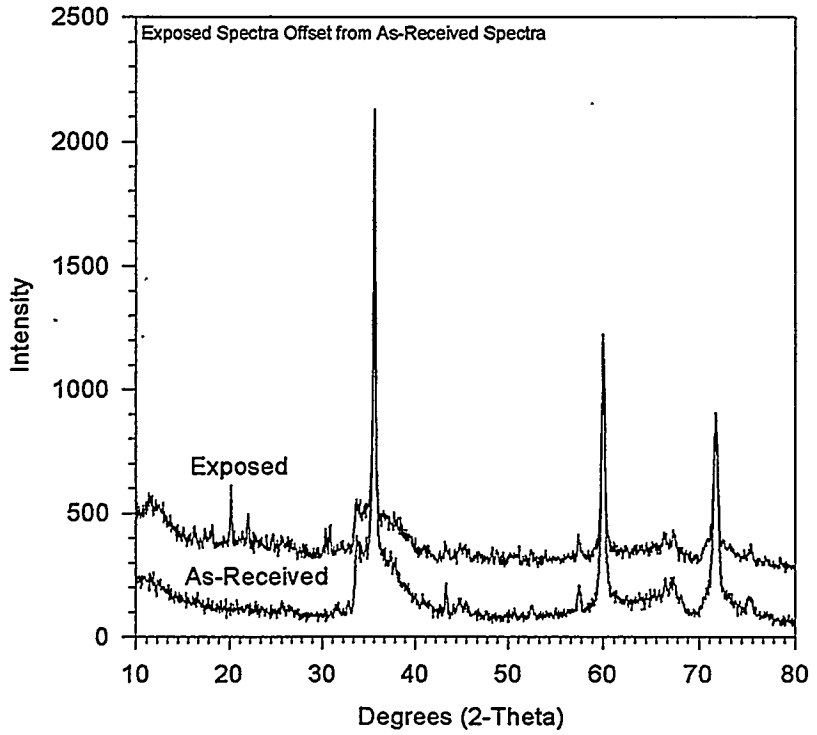

Figure 5: X-ray Diffraction of As-Received and Exposed Filtering Layer from 3M Type 203 Filter

As-received and exposed 3M filter materials were cut into 4" sections for internal pressurized burst testing. To pressurize the tubes from these materials, 3 inch rubber plugs were made and centered 0.5 inches from each end to minimize edge effects. The ends of the plugs were then compressed at a crosshead speed of 5 mm/min until the tube sections failed. Results indicate that the exposed filter maintained approximately 85 % of its initial strength.

Thermochemical Modeling

Previous investigatiors have studied and analyzed the Si-O-H system over a range of temperatures and pressures.[5-8] They proposed that temperature, pressure and H_2O (g) partial pressure would be the biggest determinants as to which silicon species would dominate in the gaseous phase. $Si(OH)_4$, $Si_2O(OH)_6$, $SiO(OH)$ and $SiO(OH)_2$ are among the silicon gases believed to be present in appreciable amounts over a broad temperature (600 - 1675 K) and pressure range (1 - 9000 atm). Among these, $Si(OH)_4$ (g) is thought to be the most dominate over the temperature and pressure ranges that combustion systems typically operate.

Six combustion systems were examined with ChemSage under normal operating conditions as summarized in Table 1. ChemSage calculates the equilibrium of products based upon the initial input of temperature, pressure and reactant species composition. A series of calculations were made to simulate the conversion of SiC to SiO_2. Figure 6 is a schematic of the reaction routes which can occur during corrosion of SiC, SiC/SiO_2 and SiO_2 (top of Figure 6). Regions I, II and III are the equilibrium conditions that can exist after the reaction is complete (bottom of Figure 6). SiC, SiO_2, carbon and the product gases are in equilibrium in Region I. This equilibrium can be reached by an initial system of SiC or SiC/SiO_2. In Region II, all of the SiC has been removed at equilibrium and only carbon, SiO_2 and the product gases remain. This region is only reached by an inital SiC/SiO_2 system. Region III consists of 100 % silica. All of the SiC and carbon have been removed from the system. An SiC/SiO_2 or pure SiO_2 system can reach this equilibrium. Figures 7 through 12 have the equilibrium regions labeled at the top of each graph. The x-axis on each figure represents the initial percentage of SiC and SiO_2. The far left of each graph represents 100 % SiC while the far right indicates 100 % SiO_2. Each data point is equal to a decrease of 5 % SiC and a corresponding increase of 5 % SiO_2.

Figures 7 through 12 show the predicted equilibrium for each system as SiC is converted to SiO_2. In all of the systems, $Si(OH)_4$ (g) is the dominant silicon gas present after a layer of silica has formed on the SiC. This agrees with the previous studies[5,6,8]. However, there is no appreciable $Si(OH)_4$ (g) product when SiC is still present. Active oxidation of SiC results in the formation of SiO_2 and the removal of silicon by SiO, SiS and SiH_4 gases. The presence of sulfur seems to have a great impact on the removal of silicon from the system. Even a small amount of sulfur (20 ppm) as in the Pinon Pine combustor (Figures 10 and 11) can seriously affect the removal of silicon from SiC. The Argonne National Laboratory reducing combustor (Figure 8) is the only system studied that does not include sulfur. As a result, the partial pressure of the dominant silicon containing gas (SiO) in region "A" is several orders of magnitude lower than any silicon containing gas in the other systems. Also of significance is the prediction of free carbon formation in all of the systems under conditions where SiC is still present. This is due to the reducing atmosphere encountered in all of the systems after the conversion of SiC to SiO_2.

The Pinon Pine system is of particular interest since the reducing conditions are the same except for the difference in pressure. When SiC is still present in the system at equilibrium, an increase in pressure from 1 to 10 atm causes a jump in SiH_4 (g) production by two orders of magnitude overtaking SiS (g) as the dominant silicon gas. However, the total removal of silicon only increases by approximately one order of magnitude assuming the gas phase reaches equilibrium. However, once a layer of silica forms, the $Si(OH)_4$ gas jumps three orders of magnitude for the same pressure increase.

	Argonne National Lab	Argonne National Lab	Penn State	Pinon Pine	Pinon Pine	Wilsonville Facility
Condition	Oxidizing	Reducing	Oxidizing	Reducing	Reducing	Carbonizing
Temperature	850°C	650°C	870°C	750°C	750°C	816°C
Pressure	1 atm	1 atm	1 atm	1 atm	10 atm	11.6 atm
N_2	72.4 %	50 %	-	48.66 %	48.66 %	52.60 %
CO_2	13.5 %	6.9 %	-	5.45 %	5.45 %	23.7 %
CO	-	8.8 %	-	23.89 %	23.89 %	6.8 %
O_2	3.7 %	-	30 %	-	-	-
H_2O	10.5 %	24 %	15 %	5.51 %	5.51 %	12.5 %
H_2	-	9.4 %	-	14.57 %	14.57 %	0.5 %
SO_2	250 ppm	-	3300 ppm	-	-	-
H_2S	-	-	-	20 ppm	20 ppm	0.08 %
NaCl	50 ppm	50 ppm	10 ppm	-	-	30 ppm
CH_4	-	-	-	1.35 %	1.35 %	1.6 %
NH_3	-	-	-	0.02 %	0.02 %	0.08 %
Other	-	-	HCl - 1100 ppm Air - Balance	Ar - 0.56 %	Ar - 0.56 %	COS - 0.015 % C_{2+} - 2.1 %

Table 1: Operating Conditions and Gas Compositions for Combustion Systems

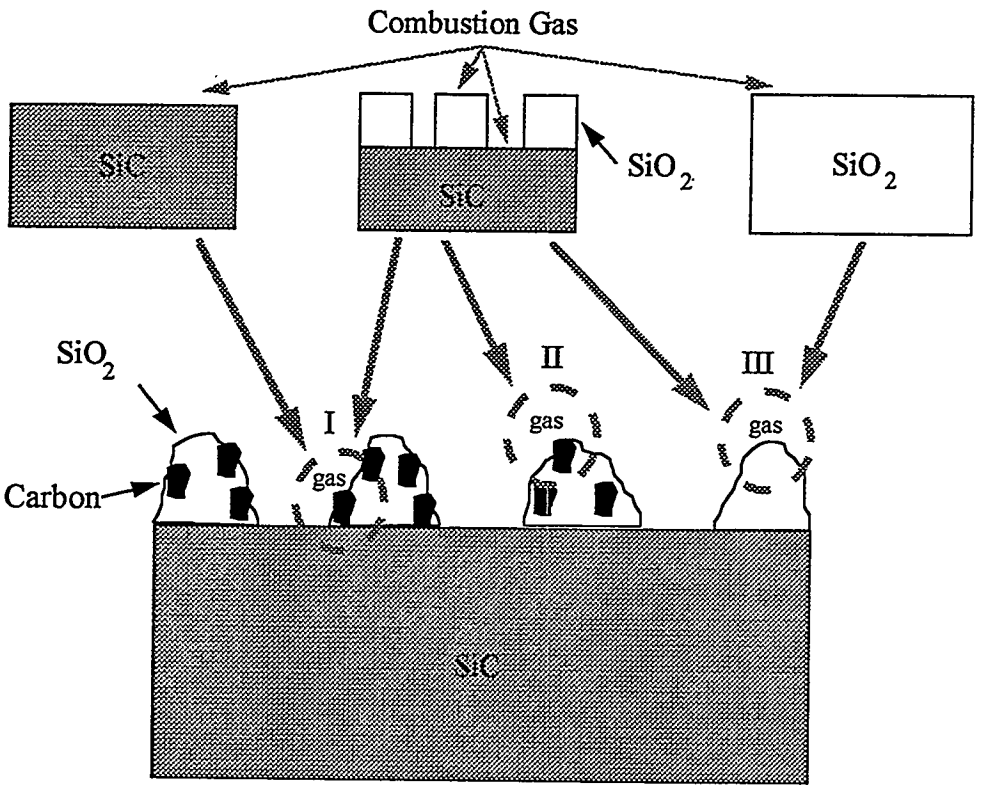

Figure 6: Schematic of Reaction Routes for Combustion Gas with SiC, SiC/SiO_2 and SiO_2

CONCLUSIONS

Flow-through tests on candidate ceramic filters are underway and preliminary results indicate that the filtering layer of the 3M Type 203 SiC material undergos a morphological change as well as the formation of a glassy phase. Internal pressurized burst testing reveals a decrease in the strength of the filter of approximately 15 %.

Thermochemical modeling of this and other combustion systems in use suggests that $Si(OH)_4$ gas is the primary source of silicon loss once a scale of silica has formed on the SiC. This should not discount the fact that significant silicon transport may also occur directly from the SiC body by SiO (g), SiH_4 (g) and particularly SiS (g) when sulfur is present. Further work needs to be done both experimentally and theoretically to fully understand the transport of silicon from the SiC/SiO2 system.

Simulating a combustion system with thermochemical modeling gives us the opportunity to study three areas inparticular. First, it allows us to determine the dominant gaseous species of a system. Second, oxide (SiO_2) and nonoxide (SiC) phases can be easily compared. Third, we can vary the pressure to decide how to simulate a high pressure run (10 atm) at 1 atmosphere.

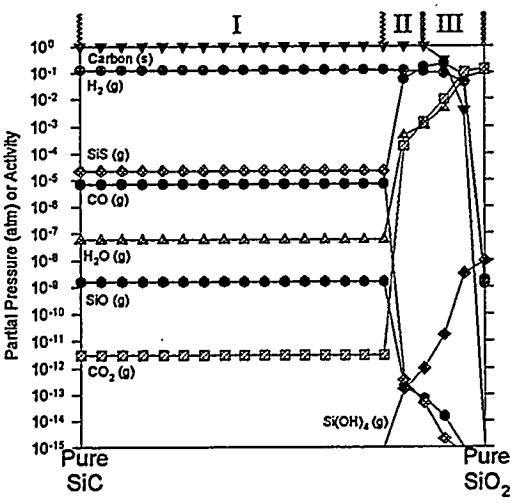

Figure 7: Predicted Partial Pressures and Activities of Product Species During Reaction of SiC with an Oxidizing Environment at 850°C and 1 atm (Argonne National Laboratory)

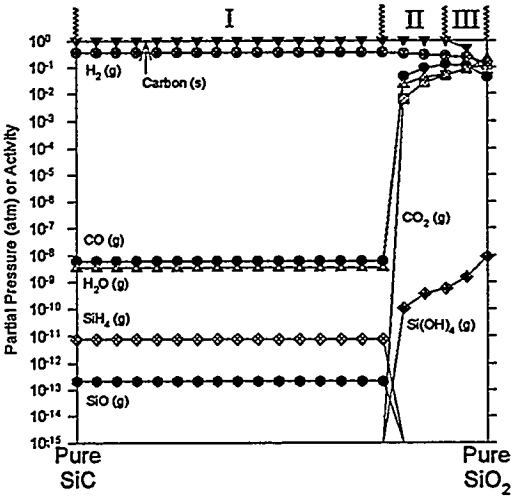

Figure 8: Predicted Partial Pressures and Activities of Product Species During Reaction of SiC with a Reducing Environment at 650°C and 1 atm (Argonne National Laboratory)

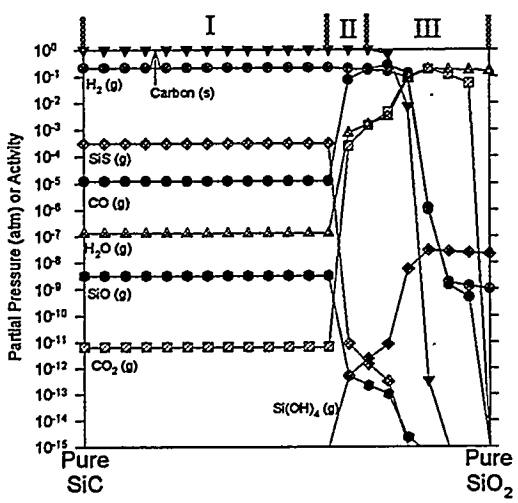

Figure 9: Predicted Partial Pressures and Activities of Product Species During Reaction of SiC with an Oxidizing Environment at 870°C and 1 atm (Penn State)

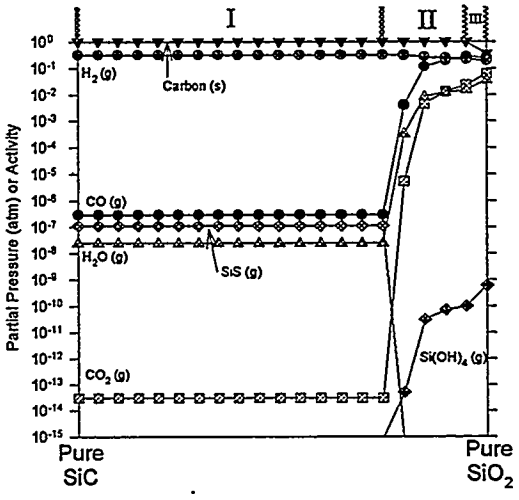

Figure 10: Predicted Partial Pressures and Activities of Product Species During Reaction of SiC with a Reducing Environment at 750°C and 1 atm (Pinon Pine)

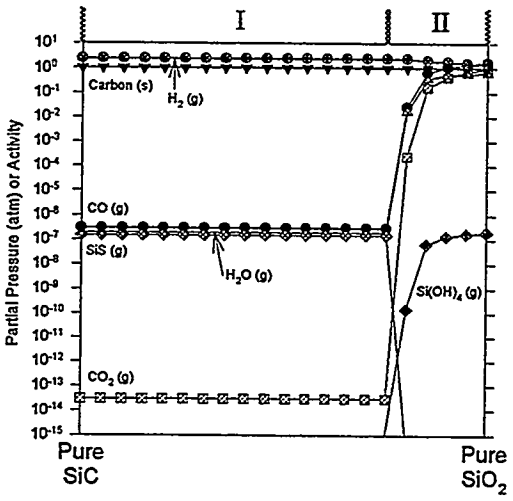

Figure 11: Predicted Partial Pressures and Activities of Product Species During Reaction of SiC with a Reducing Environment at 750°C and 10 atm (Pinon Pine)

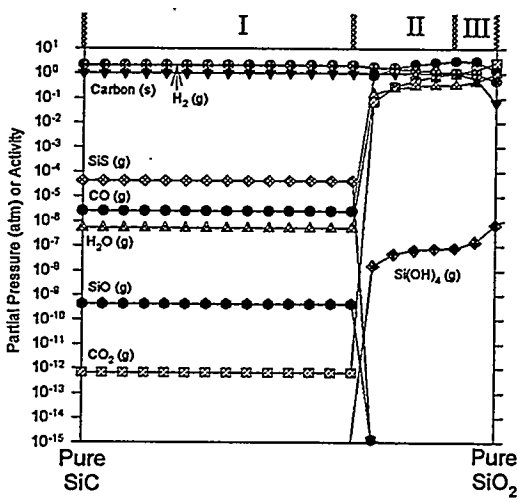

Figure 12: Predicted Partial Pressures and Activities of Product Species During Reaction of SiC with a Carbonizing Environment at 816°C and 11.6 atm (Wilsonville Facility)

1. G. Eriksson, ChemSage Application Software for Thermochemical Calculations, Version 3.0.1, © GTT TECHNOLOGIES, 1994.

2. B. Cheynet, MICROTHERM Thermodynamic Databank System for Inorganic Substances, © Thermodata, 1989.

3. M.D. Allendorf, C. F. Melius, P. Hoo, M. R. Zachariah, "Theoretical Study of the Termochemistry of Molecules in the Si-O-H System," Journal of Physical Chemistry, Vol. 99, pp. 15285 (1995).

4. D.L. Shelleman, O.M. Jadaan, D.P. Butt, R.E. Tressler, J.R. Hellmann, and J.J. Mecholsky, Jr., "High Temperature Tube Burst Test Apparatus," Journal of Testing and Evaluation, JTEVA, Vol. 20, No. 4, July 1992, pp. 275-284.

5. O. H. Krikorian, "Thermodynamics of the Silica-Steam System," Symposium on Engineering with Nuclear Explosives, 14-16 January 1970, Las Vegas, NV 1970 (Unpublished), Vol. 1, pp. 481.

6. A. Hashimoto, "The Effect of H_2O Gas on Volatilities of Planet-Forming Major Elements: I. Experimental Determination of Thermodynamic Properties of Ca-, Al-, and Si-Hydroxide Gas Molecules and its Application to the Solar Nebula," Geochimica et Cosmochimica Acta, Vol. 56, pp. 511-532 (1992).

7. D. L. Hildenbrand and K. H. Lau, "Thermochemistry of Gaseous SiO(OH), $SiO(OH)_2$, and SiO_2," Journal of Chemistry and Physics, Vol. 101, No. 7, pp. 6076-6079 (1994).

8. E. J. Opila and R. E. Hann, Jr., "Paralinear Oxidation of CVD SiC in Water Vapor," submitted to the Journal of the American Ceramic Society, January 1996.

EFFECT OF HEAT TREATMENT AT 1150°C ON CREEP-RUPTURE PROPERTIES OF ALLOY FA-180

C. G. McKamey and P. J. Maziasz

Metals and Ceramics Division
Oak Ridge National Laboratory
Oak Ridge, TN 37831-6115

ABSTRACT

The alloy FA-180, with a composition of Fe-28Al-5Cr-0.5Nb-0.8Mo-0.025Zr-0.05C-0.005B (at.%), is of interest because of its improved creep-rupture resistance when compared to alloy FA-129 (Fe-28Al-5Cr-0.5Nb-0.2C). At a temperature of 593°C and under a stress of 207 MPa, the creep-rupture life of FA-129 heat treated for 1 h at 750°C is about 20 h while the FA-180 alloy lasts approximately 100 h. Heat treatment at 1150°C has been shown to further improve the creep life of FA-180 and creep-rupture lives of approximately 2000 h have been attained. This strengthening was attributed to the presence of fine matrix and grain boundary Zr-rich MC precipitates that were produced by the heat treatment. The current study continues our investigation of the effect of heat treatment at 1150°C on the improvement of creep-rupture life in alloy FA-180. As part of our effort to understand the strengthening mechanisms involved with heat treatment at 1150°C, transmission electron microscopy was used to correlate the microstructure with the improved creep resistance. Results indicate that heat treatment at 1150°C for 1 h, followed by rapid quenching in water or mineral oil, produces even further improvements in the creep-rupture life of this alloy. A specimen being tested at 593°C and 207 MPa was stopped after over 6000 h of life, while another specimen lasted over 1600 h at 650°C and 241 MPa. The microstructure of the oil-quenched specimen contained many dislocation loops which were not present in the air-cooled specimens. These loops pinned dislocations during creep testing at temperatures of 593-700°C, resulting in a stabilized deformation microstructure and increased creep-rupture strength.

INTRODUCTION

Past studies have shown that binary Fe_3Al possesses low creep-rupture strength compared to many other alloys, with creep-rupture lives of less than 5 h being reported for tests conducted at 593°C and 207 MPa.[1,2] The combination of poor creep resistance and low room-temperature tensile ductility due to a susceptibility to environmentally-induced dynamic hydrogen embrittlement[3-5] has limited use of these alloys for structural applications despite their generally excellent corrosion behavior.[6] With regard to the ductility problem, alloy development efforts have produced significant improvements, with ductilities of 10-20% and tensile yield strengths as high as 500 MPa being reported.[7,8] Likewise, initial improvements in creep resistance have been realized through small additions of Mo, Nb, and Zr.[1,9-13]

In recent years, further creep strengthening has been produced by using heat treatments to control the microstructure.[14,15] As shown in Fig. 1, for an Fe-28Al-5Cr (at.%) alloy containing additions of Mo, Nb, Zr, C, and B (designated alloy FA-180), a 1-h 1150°C heat treatment produced creep lives of over 2000 h for tests conducted at 593°C and 207 MPa. Especially interesting is the sharp dependence of creep strength on heat treating temperature, which is illustrated by the data in Fig. 1. In earlier studies, transmission electron microscropy revealed the presence of fine precipitates which appeared to pin dislocations.[14] This, together with an activation energy for creep of approximately 150 kcal/mole (a value which is about twice that obtained earlier[1] for the binary alloy heat treated at 750°C) and high creep exponents of 7-12 (ref. 15), indicated that the observed strengthening was being produced by a precipitation mechanism. The general conclusion was that the 1150°C heat treatment resulted in the dissolution of coarse particles remaining from the melting and casting process, and then reprecipitation of finer Zr-based precipitates during cooling or the early stages of creep produced the strengthening.

The current research effort is focused on reaching a better understanding of the relationship between microstructure and strengthening mechanism(s) for this alloy and heat treatment. This paper summarizes those efforts.

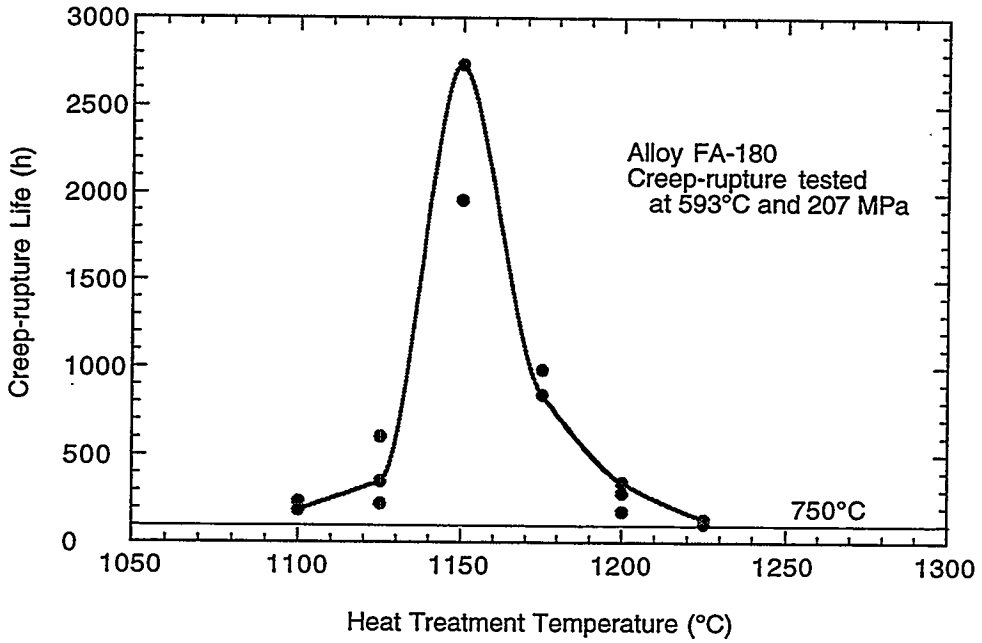

Fig. 1. Creep-rupture life as a function of heat treatment temperature (for 1 h anneals) for tests conducted on alloy FA-180 at 593°C and 207 MPa.

EXPERIMENTAL PROCEDURES

The alloy composition used in this study was Fe-28Al-5Cr (at.%) with 0.5% Nb, 0.8% Mo, 0.025% Zr, 0.05% C, and 0.005% B (Oak Ridge National Laboratory designation FA-180). It was prepared by arc-melting and drop-casting into a chilled copper mold. Fabrication to 0.8-mm-thick sheet was accomplished by hot-rolling, beginning at 1000°C and finishing at 600-650°C. After a stress relief heat treatment of 1 h at 700°C, flat tensile specimens (0.8 x 3.18 x 12.7 mm) were mechanically punched from the rolled sheet. Before creep-rupture testing, specimens were further annealed in air for 1 h at 1150°C and then were either air cooled to room temperature or were quenched in oil or water.

Creep-rupture tests were performed in air at temperatures between 593 and 750°C under stresses of 138 to 276 MPa (20-40 ksi). In order to obtain creep exponents and activation energies, minimum creep rates (MCR) were measured as the slope of the linear portion of the test curve and the data were plotted to a power-law equation. The results for quenched specimens were compared to earlier published data on air-cooled specimens.[15]

Optical metallography and scanning electron microscopy (SEM) were used to study the microstructures and fracture modes. Analytical electron microscopy (AEM) using either a Philips CM30 (300 kV) or a CM12 [120 kV, with ultra-thin-window x-ray energy dispersive spectrometry (XEDS) detector] electron microscope was performed on samples cut from the gage portion of selected test specimens.

RESULTS AND DISCUSSION

Creep-rupture tests were conducted on specimens cooled by different methods from the 1150°C heat treatment temperature and the data are presented in Table I. The creep-rupture lives of the rapidly cooled specimens are compared in Fig. 2 with the life of a specimen that had been cooled in air from the 1150°C heat treatment temperature and then tested at 593°C. The more rapidly cooled specimens (oil or water quenched) exhibited the best resistance to creep. Even though the air-cooled specimen had exhibited a very good rupture life of approximately 1959 h when tested at 593°C and 207 MPa, a specimen that had been quenched in oil showed no signs of rupturing (no increase in the very low, steady-state creep rate) after 6480 h, at which time the test was stopped. Likewise, the water quenched specimen that was tested at 650°C under a stress of 241 MPa ruptured after 1637 h, while another specimen that had been cooled more slowly in air and tested at the same conditions lasted less than 3 h. The strengthening mechanism, therefore, appears to be different for quenched versus air

Table I. Creep-Rupture Data for Alloy FA-180 as a Function of the Method Used for Cooling from the 1150°C Heat Treatment

Method of Cooling	Creep-rupture Test Conditions	Life (h)	Elongation (%)	MCR (/s)
air	593°C, 207 MPa	1959	10	8.3×10^{-7}
oil quench	593°C, 207 MPa	>6480	5	2.8×10^{-8}
air	650°C, 241 MPa	2.7	42	2.2×10^{-3}
water quench	650°C, 241 MPa	1637	9	2.2×10^{-7}

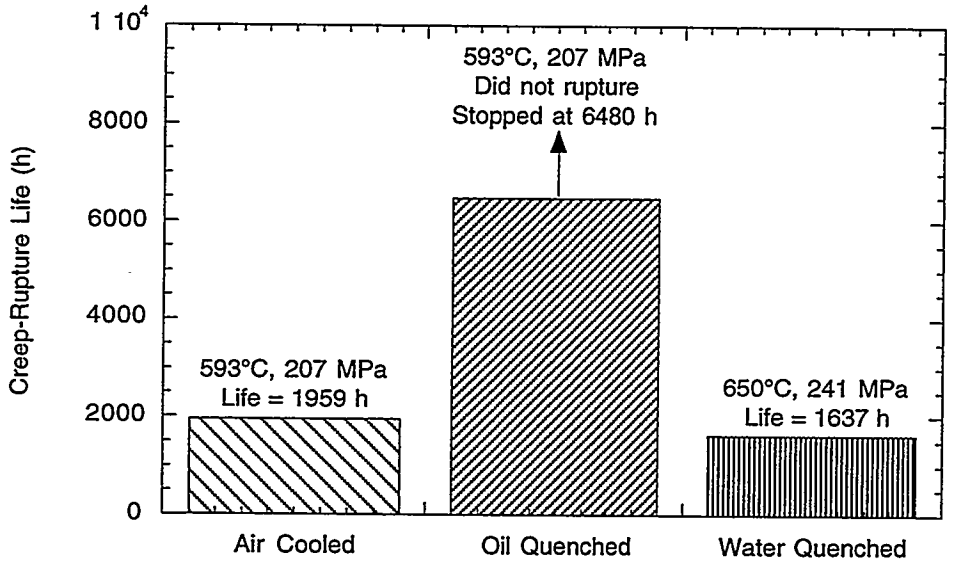

Fig. 2. Creep-rupture life of air-cooled versus quenched specimens of alloy FA-180.

cooled specimens, although the quenching medium itself does not appear to be the cause of that effect.

Creep tests were conducted as a function of temperature and stress in order to determine if the activation energies for creep (Q) and the creep exponents (n) were the same in both the air-cooled and oil-quenched conditions. The results are shown in Figs. 3 and 4. At a stress of 207 MPa (30 ksi), the activation energy for creep in the oil-quenched specimens was determined to be 76.6 kcal/mole, compared to a Q of 141.1 kcal/mole for air-cooled specimens. (The value of Q reported here for the air cooled specimens is slightly different from that reported earlier[15] because it was derived from more data points.) This significant difference in activation energy suggests that a

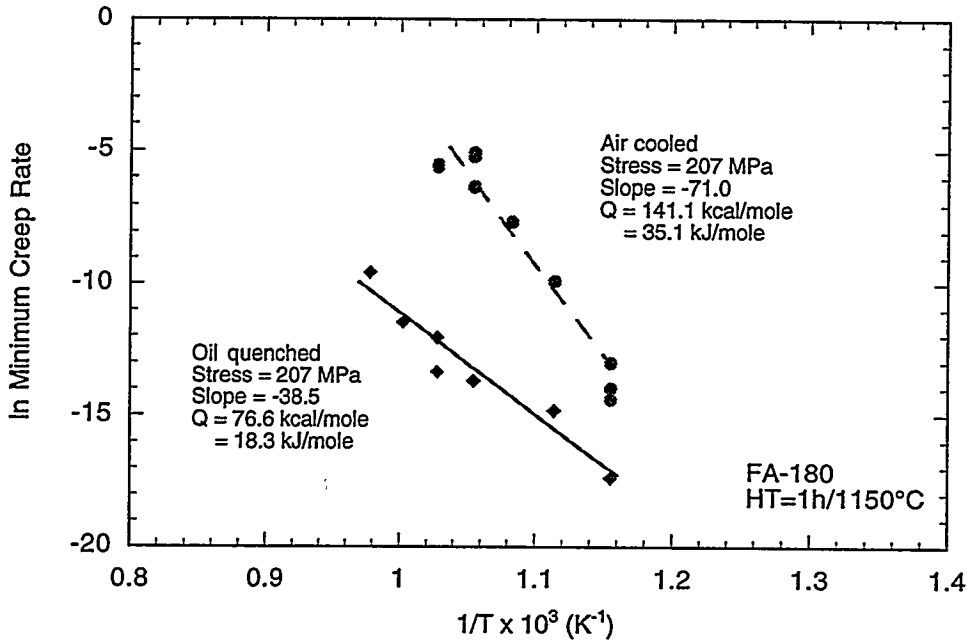

Fig. 3. Minimum creep rate versus temperature data for air cooled versus oil quenched specimens of alloy FA-180 heat treated at 1150°C. All tests were conducted at a stress of 207 MPa (30 ksi).

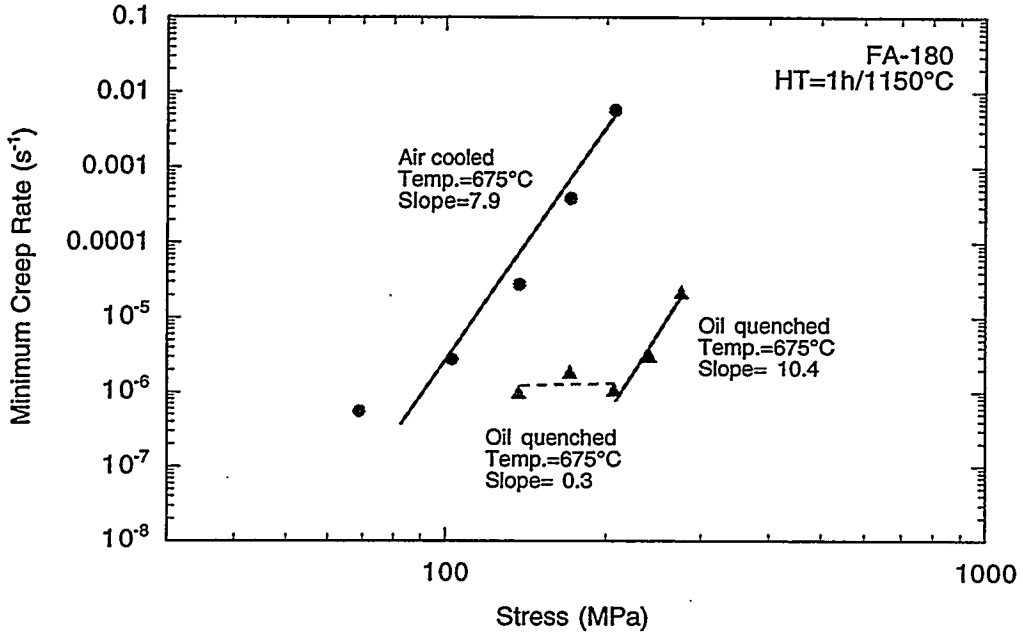

Fig. 4. Minimum creep rate versus stress data for air cooled versus oil quenched specimens of alloy FA-180 heat treated at 1150°C. All tests were conducted at 675°C.

different rate-controlling mechanism is active in the oil-quenched specimens. A plot of minimum creep rate versus stress (Fig. 4) shows a distinct break at approximately 200 MPa, with the creep exponent increasing at higher stresses. This behavior is indicative of a change in the rate-controlling creep mechanism with stress and is common in the data for many precipitate-hardened alloys.[16,17] The creep exponent of 10.4 shown in Fig. 4 for the oil-quenched specimens and the creep exponent for the air cooled specimens, which was earlier calculated to be 7.9 (ref. 15), are both indicative of alloys which have been hardened by precipitates or some other dislocation-pinning mechanism.[18,19]

Transmission electron microscopy was used to study the microstructure of the oil-quenched specimen that had been tested for 6480 h at 593°C. The micrograph in Fig. 5 shows that the creep-tested specimen contained networks of two-fold dislocations and many dislocation loops. At a higher magnification (Fig. 6), a few fine precipitates were also visible. Closer examination of the loops (Fig. 7) indicated that they were square or rectangular in shape and were restricted to the orthogonal habit planes (either <110> of <100>). Additionally, the dislocation segments in the loops appeared to be single rather than 2-fold and the four segments of each loop were of the same Burgers vector. For comparison, Fig. 8 shows the microstructure of a specimen in the as-heat-treated-and-oil-quenched (untested) condition. The dominant features are the B2 ordered domains and many black dots visible by black-white strain contrast imaging. In this case, by rotating the specimen through several diffracting conditions, most of the black dots visible in the microstructure in Fig. 8 were identified as vacancy dislocation loops, not precipitates. It therefore appears that these fine loops were created in the microstructure as a result of the rapid quench from the 1150°C annealing temperature. This is in contrast to the results from air-cooled specimens reported earlier in which fine Zr-based precipitates that formed during cooling were found to provide some measure of strengthening during creep.[14] Since it is known that vacancies are created in the Fe-Al system by quenching from high temperatures, especially for the B2 structure,[20,21] the identification of these dislocation loops as being vacancy loops is not unreasonable. Vacancy loop nature would also be consistent with their growth during further heat treatment or creep testing. During creep-rupture testing at the temperatures used in this study, the loops provided strengthening by pinning dislocations and grew in size in the process (as indicated by the larger loop size in the as-tested specimen, Fig. 5).

CONCLUSIONS

In earlier studies the creep-rupture strength of Fe_3Al-based alloy FA-180 (Fe-28Al-5Cr-0.5Nb-0.8Mo-0.025Zr-0.05C-0.005B, at.%) was shown to be improved

Fig. 5. TEM micrograph of FA-180 oil-quenched from a heat treatment at 1150°C and creep tested at 593°C for 6480 h.

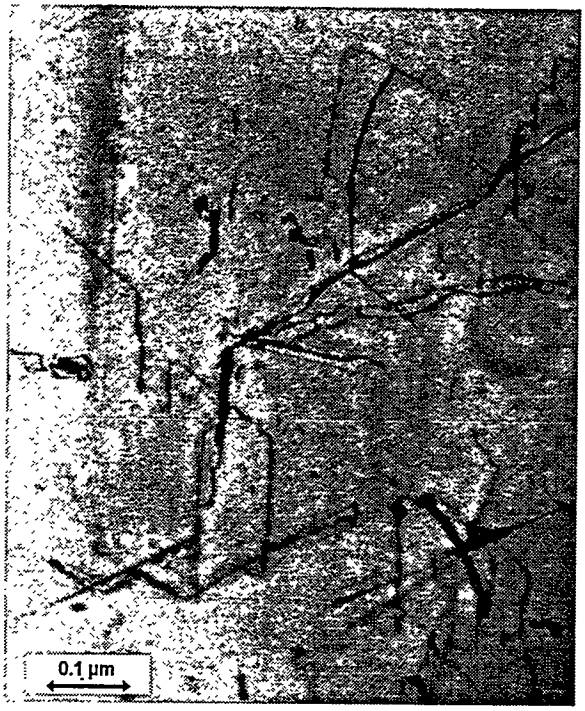

Fig. 6. Higher magnification of Fig. 5 showing presence of fine precipitates.

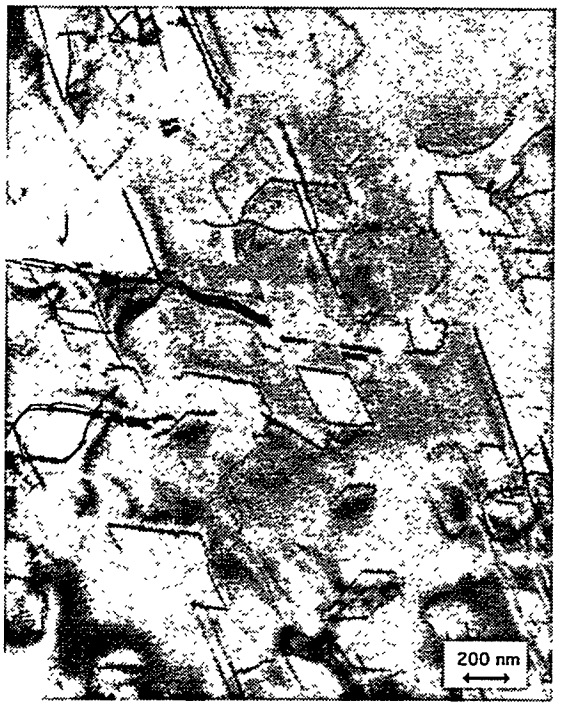

Fig. 7. Higher magnification TEM micrograph of dislocation loops visible in Fig. 5.

Fig. 8. TEM micrograph of alloy FA-180 showing B2 domains and fine dislocation loops (black dots) produced by oil-quenching from a heat treatment at 1150°C.

significantly by heat treating for 1 h at 1150°C. This strengthening was attributed to the dissolution at 1150°C of coarse particles left over from the melting and casting process and reprecipitation during cooling or during testing at 593°C of fine Zr-based matrix and grain boundary precipitates. In this study, creep-rupture tests were conducted on specimens of FA-180 that had been cooled quickly (oil or water quenched) from the 1150°C heat treatment. The results were compared to the previous data on specimens that were cooled more slowly in air. The more rapidly cooled specimens exhibited the best resistance to creep. This additional strengthening was attributed to the formation of dislocation loops as a result of the rapid quench. These loops pinned dislocations and grew slowly during testing at temperatures of 593-700°C, resulting in a stabilized deformation microstructure.

ACKNOWLEDGEMENTS

This research was sponsored by the U.S. Department of Energy, Office of Fossil Energy, Advanced Research and Technology Development Materials Program, and by the Assistant Secretary for Energy Efficiency and Renewable Energy, Office for Industrial Technologies, Advanced Industrial Materials Program, under contract DE-AC05-96OR22464 with Lockheed Martin Energy Research Corp.

REFERENCES

1. C. G. McKamey, P. J. Maziasz, and J. W. Jones, *J. Mater. Res.*, **7(8)** (1992), 2089-2106.
2. C. G. McKamey, J. H. DeVan, P. F. Tortorelli, and V. K. Sikka, *J. Mater. Res.*, **6(8)** (1991), pp. 1779-1805.
3. C. T. Liu, C. G. McKamey, and E. H. Lee, *Scripta Metall. Mater.*, **24(2)** (1990), 385-90.
4. C. T. Liu and C. G. McKamey, *High Temperature Aluminides and Intermetallics*, ed. S. H. Whang, C. T. Liu, D. P. Pope, and J. 0. Stiegler, (TMS, Warrendale, PA, 1990), pp. 133-151.
5. C. G. McKamey and C. T. Liu, *Proceedings of ADVMAT/91, First International Symposium on Environmental Effects on Advanced Materials*, edited by R. D. Kane, (Houston, TX: NACE, 1992), paper no. 17-1.
6. P. F. Tortorelli and J. H. DeVan, in *Processing, Properties, and Applications of Iron Aluminides*, edited by J. H. Schneibel and M. A. Crimp (TMS, Warrendale, PA, 1994), pp. 257-70.
7. *V. K. Sikka, SAMPE Quart.*, **22(4)** (1991), 2-10.
8. V. K. Sikka, S. Viswanathan, and C. G. McKamey, *Structural Intermetallics*, eds. R. Darolia, J. J. Lewandowski, C. T. Liu, P. L. Martin, D. B. Miracle, and M. V. Nathal, (Warrendale, PA: The Metallurgical Society, 1993), 483-91.
9. P. J. Maziasz and C. G. McKamey, *Mater. Sci. & Eng.*, **A152** (1992), 322-34.
10. D. M. Dimiduk, M. G. Mendiratta, D. Banerjee, and H. A. Lipsitt, *Acta Metall.*, **36** (1988), 2947-58.
11. P. J. Maziasz, C. G. McKamey, and C. R. Hubbard, *Alloy Phase Stability and*

Design, eds. G. M. Stocks, D. P. Pope, and A. F. Giamei (MRS, Pittsburgh, PA, 1990), pp. 349-55.

12. C. G. McKamey, P. J. Maziasz, G. M. Goodwin, and T. Zacharia, *Mat. Sci. & Eng.*, **A174** (1994), 59-70.

13. D. G. Morris, M. Nazmy, and C. Noseda, *Scripta Metall. Mater.* **31**, 173 (1994).

14. C. G. McKamey and P. J. Maziasz, in *Processing, Properties, and Applications of Iron Aluminides*, edited by J. H. Schneibel and M. A. Crimp (TMS, Warrendale, PA, 1994), pp. 147-58.

15. C. G. McKamey, Y. Marrero-Santos, and P. J. Maziasz, in *High Temperature Ordered Intermetallic Alloys VI*, edited by J. A. Horton, I. Baker, S. Hanada, R. D. Noebe, and D. S. Schwartz (MRS, Pittsburgh, 1995), pp. 249-254.

16. O. D. Sherby and P. M. Burke, *Prog. Mater. Sci.* **13**, 325 (1968).

17. R. Lagneborg and B. Bergman, *Met. Sci. J.* **10**, 20 (1976).

18. K. Sadananda, H. Jones, C. R. Feng, and A. K. Vasudevan, in *High Temperature Ordered Intermetallic Alloys IV*, edited by L. A. Johnson, D. P. Pope, and J. O. Stiegler (MRS, Pittsburgh, 1991), pp. 1019-25.

19. I. Jung, M. Rudy, and G. Sauthoff, *High Temperature Ordered Intermetallic Alloys II*, edited by N. S. Stoloff, C. C. Koch, C. T. Liu, and O. Izumi (MRS, Pittsburgh, 1987), pp. 263-74.

20. P. Nagpal and I. Baker, *Metall. Trans.* **21A**, 2281 (1990).

21. A. Ball and R. E. Smallman, *Acta Metall.* **16**, 233 (1968).

The Influence of Composition on Environmental Embrittlement of Iron Aluminides

D. A. Alven and N. S. Stoloff
Rensselaer Polytechnic Institute
Troy, New York 12180-3590

Abstract

The effects of water vapor in air and hydrogen gas on the tensile and fatigue crack growth behavior of Fe_3Al alloys has been studied at room temperature. Fe-28a%Al-5a%Cr alloys to which either Zr alone or Zr and C have been added have been tested in controlled humidity air environments as well as in 1.3 atm hydrogen or oxygen gas and in vacuum. As with other Fe_3Al alloys, oxygen produces the lowest crack growth rates as well as the highest critical stress intensities and tensile ductility in each of the alloys tested. However, while Zr lowers crack growth rates in the Paris regime, there is no apparent beneficial effect on crack growth thresholds. Hydrogen gas also produces unusual results. While crack growth rates are very high in hydrogen in the Paris regime for all alloys, hydrogen only lowers the crack growth threshold relative to air in ternary Fe-28Al-5Cr; it does not lower the threshold in the Zr-containing alloys. Fracture path tends to be transgranular in all alloys and environments. The results will be discussed in the light of possible effects of Zr on oxide formation.

Introduction

Iron aluminides are currently being considered for use in applications where excellent corrosion resistance, moderate strength at temperatures up to 500°C, and low cost are desired. Binary iron aluminides do not possess high ductility at room temperature in air; however, when tested in vacuum or gaseous oxygen environments iron aluminides have demonstrated ductility of greater than 10% (1, 2, 3). This indicates that Fe_3Al is an inherently ductile material and the low ductility in air is due to an environmental interaction.

The purpose of this research was to examine the changes in mechanical properties of several Fe_3Al,Cr intermetallic alloys in various environments. The tensile behavior and fatigue crack growth resistance were examined and the resulting data will be discussed in the light of the role of hydrogen in embrittlement of the iron-aluminum alloys.

Experimental Procedure

Alloy Composition and Heat Treatment

The composition of the alloys examined in this study are shown in Table 1. All alloys were fabricated at the Oak Ridge National Laboratory (ORNL) by vacuum induction melting, extrusion, and in the case of plate material either hot or warm rolling to the final thickness. The annealing parameters for B2 order consisted of a 700°C anneal for 1 hour with a mineral oil quench, which was then repeated.

Table 1. Composition of Iron Aluminide Alloys (Atomic %)

	ternary	1%ZrC	0.5%ZrC	0.5%Zr
Fe	67.0	65.95	66.45	66.5
Al	28.0	28.0	28.0	28.0
Cr	5.0	5.0	5.0	5.0
Zr	-	1.0	0.5	0.5
C	-	0.05	0.05	-
Grain Size	180μm	Partially recrystallized	Partially recrystallized	Partially recrystallized

Tensile Tests

Tensile specimens were either cylindrical with a 12.7mm long by 5.7mm diameter gauge section or sheet with a 5mm by 1.2mm by 0.5mm gauge section. All tension specimens were polished to a 0.3μm finish and ultra-sonically cleansed in acetone prior to testing. Testing was carried out in a servo-hydraulic MTS machine fitted with a vacuum chamber or a screw-driven Instron. The strain rate used in all test was 3×10^{-4}/sec. All test were conducted at room temperature.

When testing in oxygen or hydrogen gas, the environmental chamber was first evacuated to $< 6.6 \times 10^{-4}$ Pa using a diffusion pump fitted with a cold trap. The appropriate gas was then admitted to the chamber at a pressure of 2300 Pa over atmospheric pressure for 1 hour prior to testing.

Fatigue Crack Growth Tests

Fatigue crack growth test were performed at room temperature in air, hydrogen , oxygen gas, and vacuum. When testing in an environment the evacuation procedure was the same as with the tensile tests. For constant humidity tests the chamber was first evacuated then compressed air was bubbled through a closed beaker containing an aqueous solution of potassium acetate, which produced 21%rH.

Compact tension specimens were used in all fatigue tests and were cut by electro discharge machining such that the crack propagation direction was perpendicular to the rolling direction. The ternary, 0.5%Zr, and 0.5%ZrC specimens were 31.75mm x 30.5mm x 4.8mm thick, while the 1%ZrC specimens were 28.7mm x 27.6mm x 3.6mm thick due to plate materials supplied by ORNL. Crack length was monitored via the d.c. potential drop method. Calibration curves were created relating crack length to potential drop by optically measuring the crack length with a traveling microscope. The R-ratio (minimum to maximum stress)was 0.5 in order to minimize crack closure effects and the frequency was 20Hz.

Experimental Results

Tensile Experiments

Tensile data for the iron aluminides examined are listed in Table 2. Alloy 0.5%ZrC had the highest ductility and UTS of all alloys tested. Oxygen provided the highest ductility and UTS for the Ternary alloy while 0.5%ZrC had the same values of ductility and UTS in air and oxygen. Increasing the amount of Zr to 1a% resulted in a decrease of both the ductility and UTS, while the removal of C als decreased the ductility and UTS, but not as severely.

Figures 1(a) - 1(d) show the fracture surfaces of all the alloys tested in air. Fractographic features were found to be insensitive to environment in both the ternary and the 0.5%ZrC alloys. The fracture mode was observed to be mixed transgranular

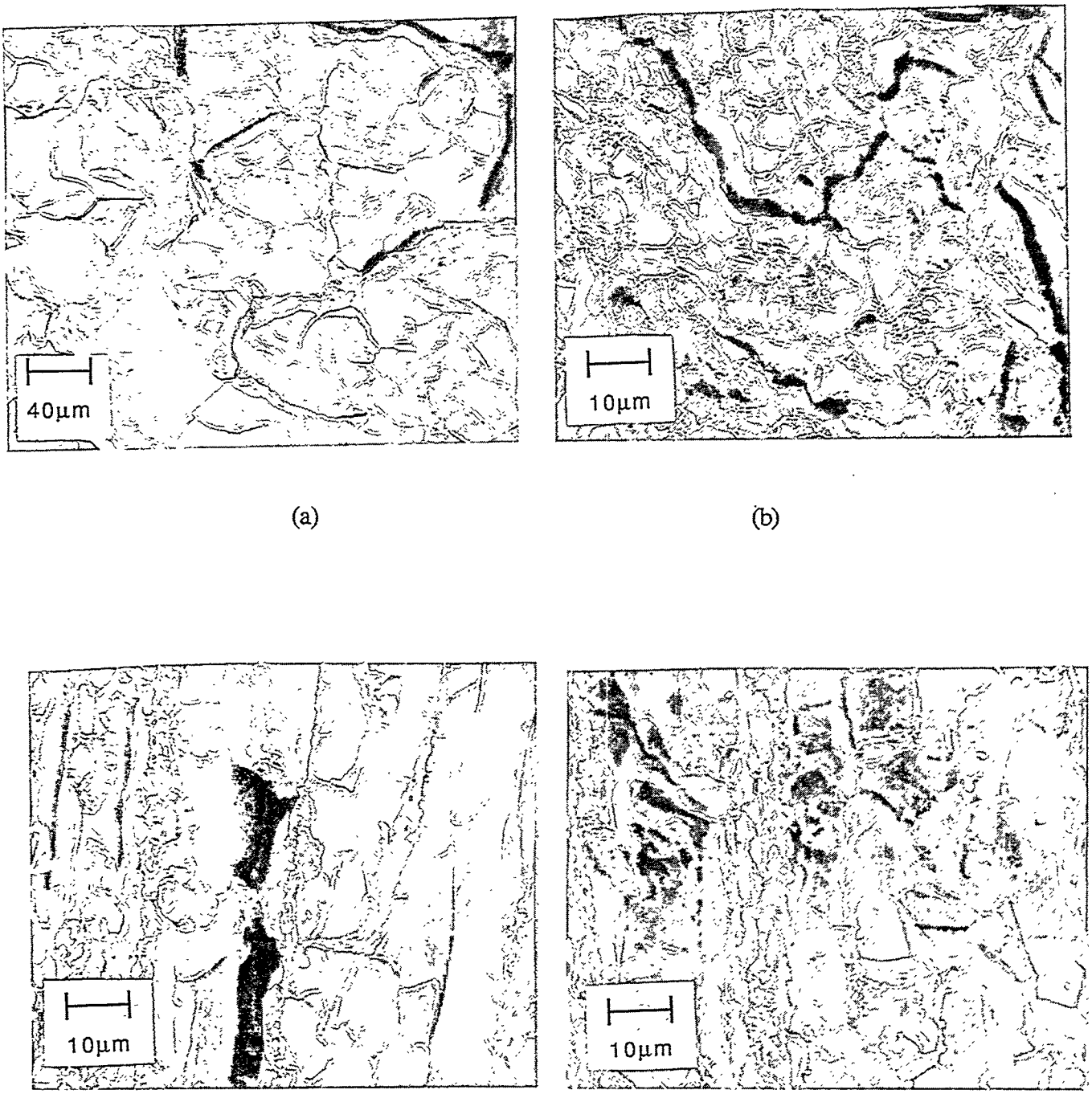

Fig. 1. Fracture Surfaces of the (a) Ternary Alloy, (b) 0.5%ZrC Alloy, (c) 0.5%Zr Alloy and (d) 1%ZrC Alloy Tested in Tension at 25°C in Air

cleavage and intergranular fracture in the ternary alloy with a switch to transgranular cleavage and dimpled rupture in the 0.5%ZrC and 0.5%Zr alloys. The fracture mode reverted back to mixed transgranular cleavage and intergranular fracture in the 1%ZrC alloy.

Table 2. Tensile Properties of the Iron Aluminides

Alloy	Air			O_2			H_2		
	YS (MPa)	UTS (MPa)	Ductility (%)	YS (MPa)	UTS (MPa)	Ductility (%)	YS (MPa)	UTS (MPa)	Ductility (%)
Ternary	500	980	10.2	510	1180	12.8	500	740	4.2
0.5%ZrC	690	1460	13.8	680	1460	13.1	680	1200	6.1
0.5%Zr *	670	1000	8.2	-	-	-	-	-	-
1%ZrC *	510	880	5.3	-	-	-	-	-	-

* Average of three tests

Fatigue Crack Growth Experiments

Fatigue crack growth curves are shown in Figures 2, 3, 4, and 5 for the iron aluminides studied. Table 2 lists the threshold and critical stress intensities, as well as the stress intensity necessary to produce a crack growth rate of 10^{-7} m/cycle. The slope in the Paris regime is not reported since a linear region in the da/dN vs. ΔK curves could not always be defined.

Table 2. FCG Data for the Iron Aluminides

Alloy	Environment	ΔK (10^{-7}) (MPa$\sqrt{m}$)	ΔK_{TH} (MPa$\sqrt{m}$)	ΔK_C (MPa$\sqrt{m}$)
Ternary	Air (30% rH)	20.3	16.9	26.4
Ternary	O_2	38.4	24.2	42.4
Ternary	Vacuum	32.6	29.2	39.1
Ternary	H_2	15.1	14.2	19.9
0.5%ZrC	Air (21% rH)	29.0	18.0	59.4
0.5%ZrC	O_2	42.3	18.6	68.7
0.5%ZrC	Vacuum	29.0	23.2	38.0
0.5%ZrC	H_2	21.1	19.8	42.8
0.5%Zr	Air (21% rH)	28.1	18.7	39.0
0.5%Zr	O_2	43.3	20.0	48.9
0.5%Zr	Vacuum	32.6	32.5	46.1
0.5%Zr	H_2	21.2	20.5	38.9
1%ZrC	Air (21% rH)	22.8	16.2	27.6
1%ZrC	O_2	35.9	23.0	36.8
1%ZrC	Vacuum	30.4	26.9	35.1
1%ZrC	H_2	21.2	20.5	38.9

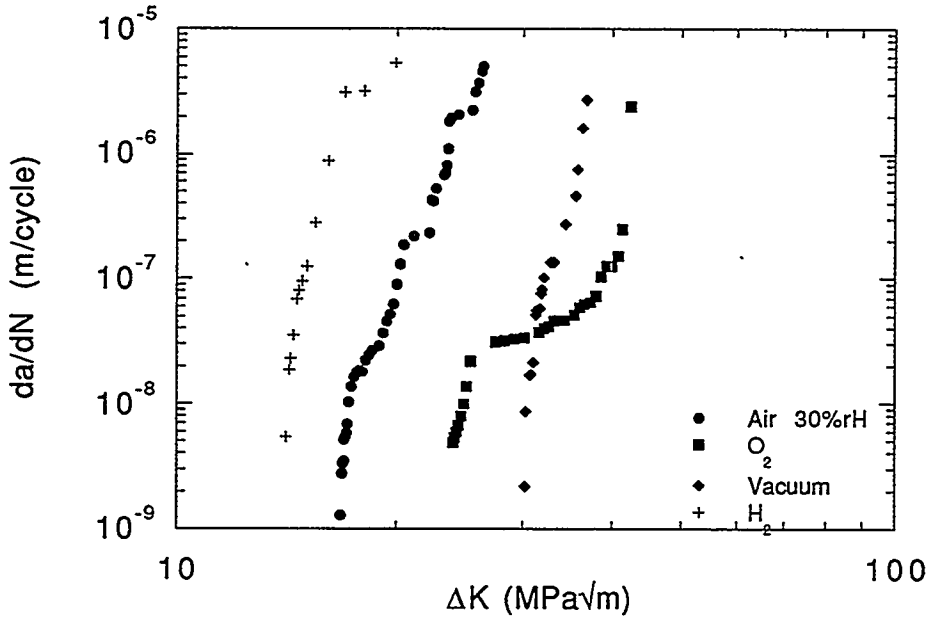

Figure 2. Fatigue Crack Growth Curves for the Ternary Alloy at 25°C.

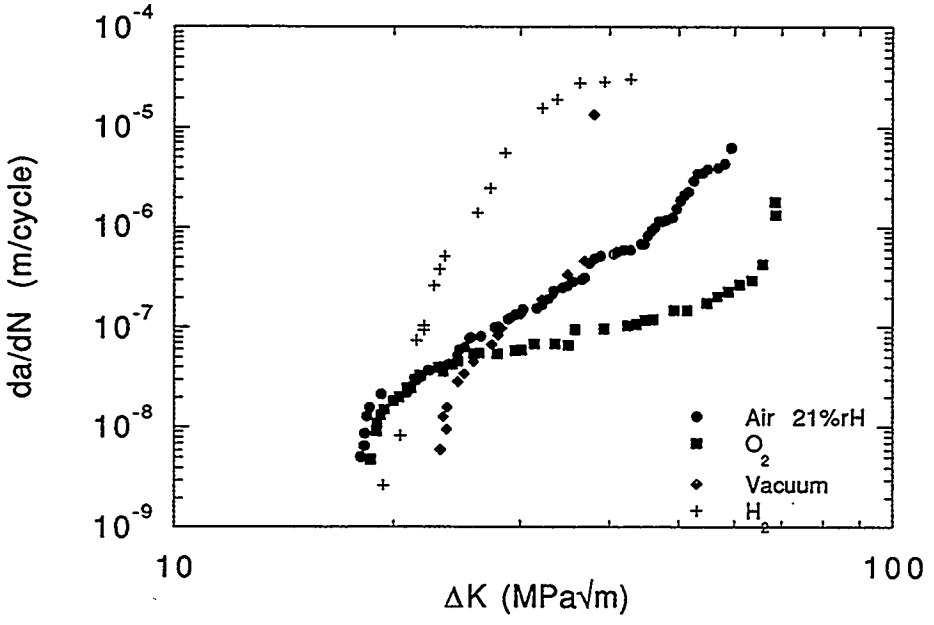

Figure 3. Fatigue Crack Growth Curves for the 0.5%ZrC alloy at 25°C.

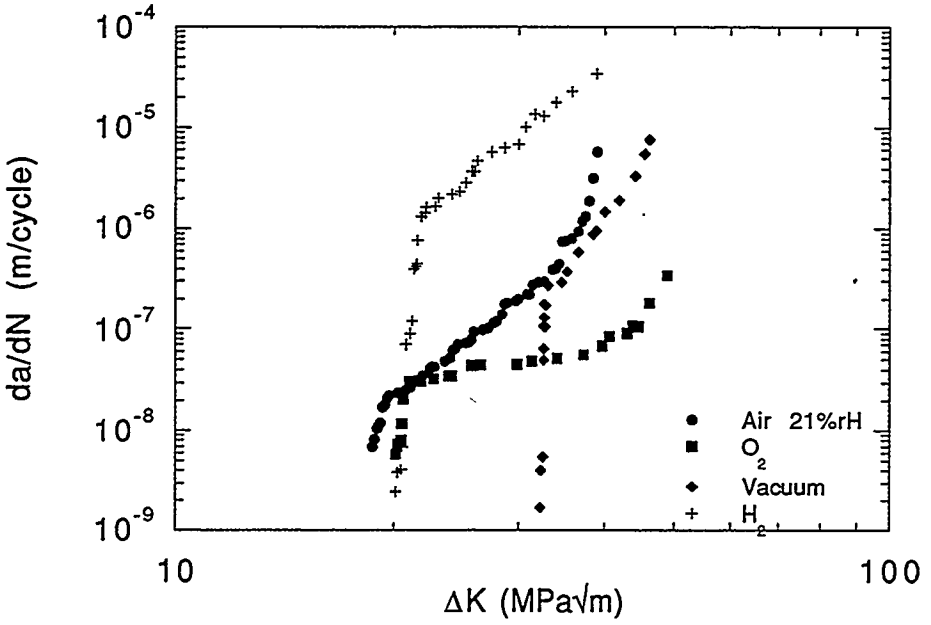

Figure 4. Fatigue Crack Growth Curves for the 0.5%Zr Alloy at 25°C.

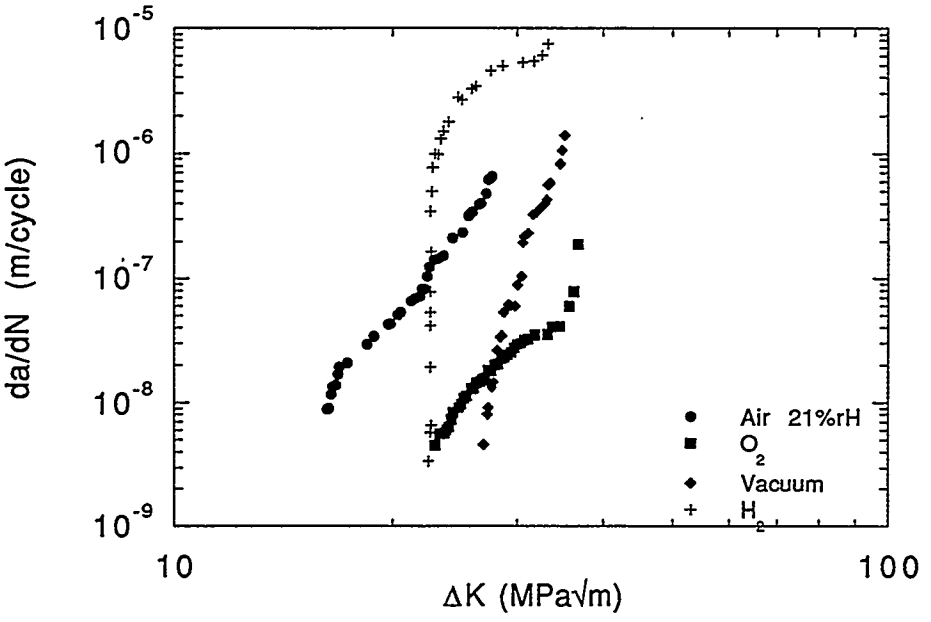

Figure 5. Fatigue Crack Growth Curves for the 1%ZrC Alloy at 25°C.

In all alloys tested oxygen provides the lowest crack growth rates. The 0.5%ZrC alloy has the highest critical stress intensity values in all environments, except vacuum, of the alloys studied. The addition of carbon to the 0.5%Zr alloy does not affect the crack growth rates but significantly increases the fracture toughness. The increase in Zr content to 1a% is detrimental to the crack growth resistance while increasing the threshold stress intensities in all environments except air. In all Zr-containing alloys the threshold stress intensity when tested in hydrogen gas was found to be higher than in air.

Figures 6(a) - 6(d) show the fracture surfaces of the fatigued specimens. The fracture surfaces were found to be insensitive to environment for all alloys. The ternary alloy exhibited mixed transgranular cleavage and intergranular fracture, while the fracture mode of the 0.5%ZrC alloy was transgranular, by what appears to be a tearing mechanism. The 1%ZrC alloy failed by a mixed transgranular tearing and intergranular fracture mode, while the0.5%Zr alloy failed by mostly transgranular tearing.

Discussion

The increased tensile elongation of the ternary alloy in oxygen as compared to air demonstrates the embrittling effect of moisture in laboratory air, which is consistent with previous findings on Fe_3Al,Cr (4, 5). The 0.5%ZrC alloy exhibits similar elongations in air and oxygen while the elongation is reduced in hydrogen. For the Zr-containing alloys the elongation is reduced when the C is removed and further reduced when the Zr content is increased to 1a% with the C content maintained at 0.05a%. This suggests that a small amount of Zr can increase the intrinsic ductility of Fe_3Al,Cr alloys.

The fatigue crack growth behavior of all alloys clearly show the embrittling effect of hydrogen whether it is present as hydrogen gas or water vapor in air. The lowest crack growth rates were found in oxygen for all alloys. The difference in critical stress intensity in the Zr-containing alloys between air and oxygen (about 21%) was much less

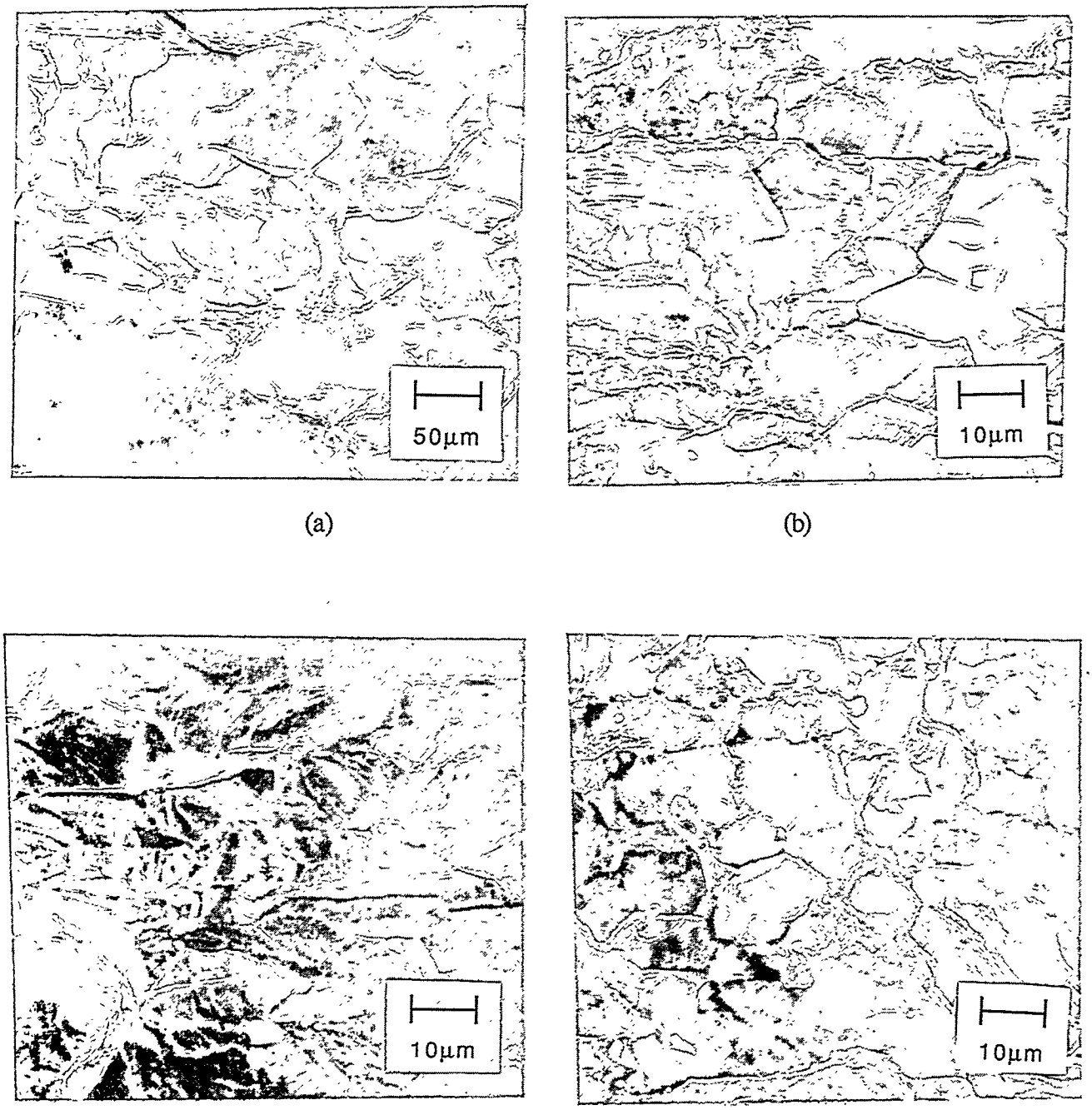

Fig. 6. Fracture Surfaces of (a) Ternary Alloy, (b) 0.5%ZrC Alloy, (c) 0.5%Zr Alloy and (d) 1%ZrC Alloy Fatigued at 25°C in Air

than in the ternary alloy (36%) which indicates that Zr-containing alloys are less susceptible to moisture-induced embrittlement.

The threshold stress intensities are affected by Zr additions. The addition of 1a% Zr is only beneficial in hydrogen; in all other environments there is no difference when compared to the ternary alloy. In air and in hydrogen 0.5a% Zr raises the threshold stress intensity by 6% and 28% respectively, while in oxygen it lowers the threshold stress intensity by 23% when compared to the ternary alloy.

An interesting effect of the addition of Zr was on the fatigue crack growth resistance in hydrogen. In all Zr-containing alloys the threshold stress intensity is higher in hydrogen gas than in air while the crack growth rate is much higher. The threshold stress intensity also exhibits no change from oxygen to hydrogen for all Zr-containing alloys .

The low crack growth rates in the 0.5%Zr alloys were the most surprising results of this investigation. It has been reported that Zr can influence the oxide formation in iron aluminides at elevated temperatures (6), but it remains to be determined if a similar effect takes place on fresh fracture surfaces at room temperature.

Another explanation by which Zr could affect the crack growth rate is either as a grain boundary strengthener and/or a trap for H so that the later can not reach the crack-tip region. The addition of 0.5a% Zr results in a change from mixed transgranular cleavage and intergranular fracture to transgranular tearing, which could point to both an increase in the strength of grain boundaries as well as trapping of H before it reaches the potential flaw sites of the cleavage planes. Zr additions have been found to increase tensile ductilities in Ni_3Al alloys (7, 8, 9) but the fracture mode was unchanged. Further work is in progress to try to identify the mechanism for improved crack growth resistance of Zr-containing alloys.

Conclusions

The addition of small amounts of Zr to Fe_3Al,Cr alloys results in lower crack growth rates. The beneficial effect of Zr is limited, since the addition of 1a% Zr results in higher crack growth rates, similar to those for the ternary alloy. The addition of C appears to only affect the fracture toughness of Fe_3Al,Cr alloys. Zr additions also result in increased threshold values in hydrogen when compared to air, while the crack growth rate at higher ΔK was higher in hydrogen.

Acknowledgements

The authors are grateful to the Department of Energy, Fossil Energy Program for providing financial support under Martin Marietta Energy Subcontract No. 19X-SF521C. The authors are also grateful for helpful discussions with Dr. V. K. Sikka of ORNL and to Dr. Sikka for providing the alloys.

References

1. C. T. Liu, E. H. Lee and C. G. McKamey, Scr. Metall., vol. 23, pp. 875-880 (1989).

2. A. Castagna, Ph.D. Thesis, Rensselaer Polytechnic Institute (1995).

3. A. Castagna, P. J. Maziasz and N. S. Stoloff, I. Baker, R. Darolia, J. D. Whittenberger, M. H. Yoo, Eds., High Temperature Ordered Intermetallic Alloys V (MRS Symp. Proc., Pittsburgh, 1993), vol. 288, pp. 1043-1048.

4. C. G. McKamey, J. A. Horton and C. T. Liu, J. Mater. Res., vol. 4, pp. 1156-1163 (1989).

5. C. G. McKamey and C. T. Liu, Scr. Metall., vol. 24, pp. 2119-2122 (1990).

6. P. F. Tortorelli, . (Oak Ridge National Laboratory, private communication, 1995),

7. E. P. George, C. T. Liu and D. P. Pope, Scripta Metall., vol. 27, pp. 365-370 (1992).

8. E. P. George, C. T. Liu and D. P. Pope, Scripta Metall., vol. 28, pp. 857-862 (1993).

9. E. P. George, C. T. Liu and D. P. Pope, in Structural Intermetallics R. Darolia, J. J. Lewandowski, C. T. Liu, P. L. Martin, D. B. Miracle, M. V. Nathal, Eds. (TMS, Warrendale, PA, 1993) pp. 431-436.

EFFECTS OF TITANIUM AND ZIRCONIUM ON IRON ALUMINIDE WELDMENTS

R. P. Burt*, G. R. Edwards*, and S. A. David**

*Center for Welding, Joining, and Coatings Research
Colorado School of Mines
Golden, CO 80401

**Oak Ridge National Laboratory
Metals and Ceramics Division
Oak Ridge, TN 37831

ABSTRACT

Iron aluminides form a coarse fusion zone microstructure when gas-tungsten arc welded. This microstructure is susceptible to hydrogen cracking when water vapor is present in the welding environment. Because fusion zone microstructural refinement can reduce the hydrogen cracking susceptibility, titanium was used to inoculate the weld pool in iron aluminide alloy FA-129. Although the fusion zone microstructure was significantly refined by this method, the fracture stress was found to decrease with titanium additions. This decrease is attributed to an increase in inclusions at the grain boundaries.

INTRODUCTION

Iron aluminides have good strength, oxidation resistance, and corrosion resistance at high temperatures. However, using these alloys for structural applications has been limited due to the poor weldability of these materials. Iron aluminides form a coarse fusion zone microstructure which is susceptible to hydrogen cracking when gas-tungsten arc (GTA) welded in the presence of water vapor. Previous research has demonstrated that the resistance to hydrogen cracking can be improved by refining the fusion zone microstructure in iron aluminide weldments.

Fasching used magnetic arc oscillation to refine the fusion zone microstructure in iron aluminide alloy FA-129 weldments[1]. When welded in an inert environment, arc oscillation effectively refined the fusion zone microstructure, and the refined microstructures demonstrated improved fracture stress and ductility when slow strain rate tensile tested in the presence of water vapor. Water vapor was then added to the welding environment to determine if the improved properties of the refined fusion zone decreased the susceptibility to hydrogen cracking. However, each different water vapor concentration present during welding required unique parameters for effective magnetic arc oscillation fusion zone refinement. Recent work has focused on finding a refinement method less sensitive to the welding environment. This paper reports the effect of weld pool inoculation on the properties of alloy FA-129.

EXPERIMENTAL PROCEDURE

Ingots of alloy FA-129 were melted and cast under vacuum at Oak Ridge National Laboratory with the composition shown in Table 1. The ingots were extruded and then hot rolled at 650°C to a nominal thickness of 760μm. After a 2-hr anneal at 650°C, the sheet was pickled in a solution of 20 parts water, 2 parts nitric acid, and one part hydrofluoric acid to remove the oxide layer.

Table 1 Iron aluminide alloy FA-129 composition

	Fe	Al	Cr	Nb	C
wt. pct.	66.3	28.0	5.00	0.50	0.20
at. pct.	77.7	15.9	5.45	0.97	0.05

Welding coupons were sheared from the sheet to be used for either metallographic analysis (51mm x 51mm) or tensile testing (76mm x 51mm). A groove was machined into the coupons using a bandsaw with no lubrication, and the coupons were then given a final cleaning with methanol prior to welding. Titanium powder (99.5%, <44μm) was deposited in the groove and covered with a 430μm protective cap made of FA-129 as well. The final sample configuration is shown in Figure 1.

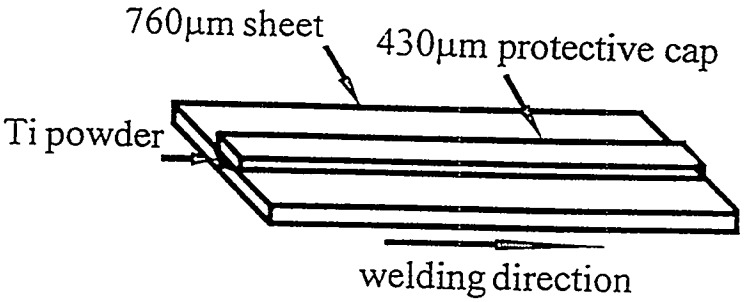

Fig. 1. Schematic diagram of welding coupon used for inoculation study.

A series of GTA welds were made in an argon filled glovebox to determine the effects of heat input and titanium concentration on the fusion zone microstructure. Table 2 summarizes the matrix used.

Table 2 Range of test variables

	Low	High
Heat Input (J/mm)	118	142
Titanium Addition (mg/10mm)	2	6

For metallographic analysis of the weldments, samples were mounted, ground, and polished using standard metallographic techniques. The etchant used to observe the fusion zone microstructure was 60 ml methanol, 40 ml nitric acid, and 20 ml hydrochloric acid. The average fusion zone grain size was determined by using a Leco image analyzer to measure the length, width, and thickness of the fusion zone grains. The average grain size reported is the average of the three measurements.

For inclusion analysis, an etchant of 96 ml water, 2 ml nitric acid, and 2 ml hydrofluoric acid was used. Inclusion fractions were determined by performing point counting on micrographs taken from several locations in the fusion zone. Inclusions were classified as either being located in the matrix or at a grain boundary.

Tensile testing samples were also welded in an inert environment. After welding, the coupons were sheared to a width of 25 millimeters, ground to a uniform thickness across the weldment, and a reduced section was ground into the specimen at the fusion zone (Figure 2). The epoxy beads were added to prevent slipping of the extensometer during tensile testing.

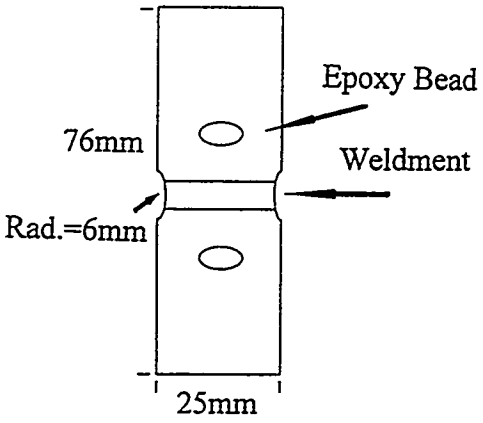

Fig. 2. Schematic of sample used for slow strain rate tensile testing.

Slow strain rate tensile testing (2.78×10^{-6} s^{-1}) was performed on an M.T.S. fitted with a Plexiglas chamber to control the testing environment. Water vapor was added to the chamber by bubbling argon through deionized water to obtain testing environments which varied the water vapor concentration from 300 to 9000 ppm. A humidity meter was used to measure the actual water vapor concentration in the chamber during the tensile test. The load and strain data were collected on a P.C. during the test. Fracture stress was determined by dividing the maximum load by the cross-sectional area of the fractured sample.

RESULTS AND DISCUSSION

The addition of titanium to the weld pool effectively refined the fusion zone microstructure. The average grain size in the fusion zone was found to be dependent upon three parameters: travel speed, heat input, and titanium concentration. Initial welding was performed at 4 mm/s. At this travel speed a molten ball was observed to develop in front of the weld pool, which was then pushed ahead of the arc. No fusion zone refinement was observed. When the travel speed was decreased to 2 mm/s, and the welding current was adjusted such that the heat input was not changed, a typical weld pool was formed and the fusion zone was refined.

The lowest heat input used in the study, 118 J/mm, was chosen because it was the minimum value which gave full penetration during welding. However, at the low heat input, fusion zone refinement was not uniform down the weld length and was not consistent from weld to weld. At the higher heat input value, 142 J/mm, fusion zone refinement was uniform throughout the weld and repeatable from weld to weld.

Finally, the fusion zone microstructure was dependent upon titanium concentration. With no titanium addition, the fusion zone microstructure consisted of large columnar grains meeting at a well defined centerline. The average unrefined fusion zone grain size was 530μm. With the lowest titanium addition, the microstructure was a mixture of columnar grains, located at the edge of the fusion zone, and more equiaxed grains at the weld centerline. With higher titanium additions, the fusion zone was completely uniform with fine, equiaxed grains.

The results of the initial tests are shown in Table 3. Given the more consistent results obtained when the higher heat input of 142 J/mm was used with a travel speed of 2 mm/s, these parameters were used when welding coupons for tensile samples. The high and low titanium additions were kept the same for the tensile sample testing. Using energy dispersive spectroscopy, it was determined that the addition of 2mg/10mm of titanium resulted in 0.8 weight percent titanium in the fusion zone and an average fusion zone grain size of 370μm. Similarly, a 6mg/10mm titanium addition resulted in 1.2 weight

percent titanium in the fusion zone and an average fusion zone grain size of 70μm. Figure 3 shows the microstructures obtained using the above parameters. These represent the microstructures used for slow strain rate tensile testing.

Table 3 Effect of welding parameters on fusion the fusion zone microstructure with titanium inoculation

Heat Input (J/mm)	Ti Addition (mg/10mm)	Avg. Fusion Zone Grain Size (μm)	Aspect Ratio (length/width)	Uniform Refinement
118	2	215	2.6	No
118	6	280	2.9	No
142	2	370	3.6	Yes
142	6	70	1.6	Yes

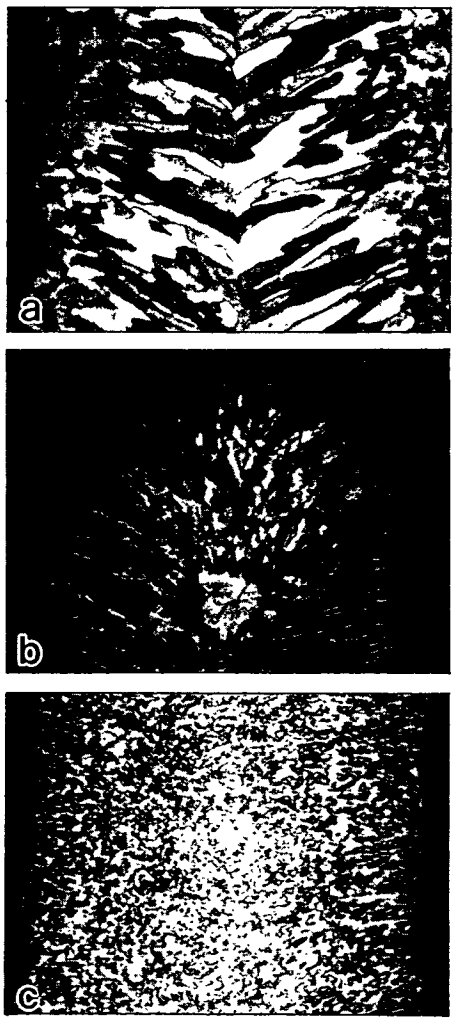

Fig. 3. Fusion zone microstructure of titanium inoculated welds. a) 0% Ti, b) 0.8% Ti, c) 1.2% Ti (14X)

The effects of titanium additions and welding parameters on the fusion zone microstructure are not unexpected. Titanium additions were made with the expectation that the particles would dissolve and precipitate out as carbides and possibly oxides or intermetallics during solidification. These inclusions would then provide heterogeneous nucleation sites in the weld pool. Weld pool conditions are more favorable for these reactions with a slower travel speed. Decreasing the travel speed, while holding the heat input constant by adjusting either the welding current or voltage, gives more time for reactions in the weld pool. If the heat input is increased, the weld pool conditions are also more favorable due to the improved reaction kinetics.

Slow strain rate tensile testing, however, did not give expected results. With increasing titanium concentration, decreasing average grain size, the fracture stress decreased (Figure 4). The fracture stress measured for the unrefined weldments were consistent with Fasching's study[1], consequently, the decrease does not appear to be a material heat effect or a result of the tensile sample configuration (no reduced section was used in Fasching's study).

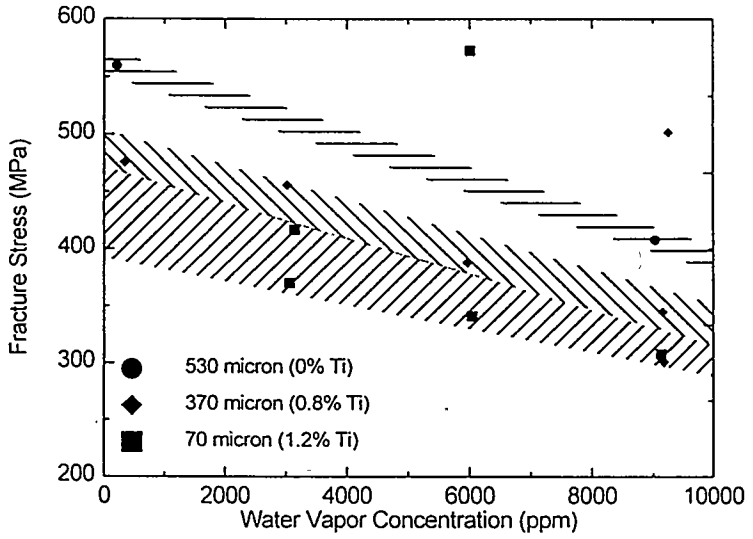

Fig. 4. Fracture stress of titanium inoculated welds as a function of titanium concentration and water concentration.

The effect of titanium on the fusion zone inclusion distribution appears to be the cause of the decrease in fracture stress. The overall fraction of inclusions measured in the fusion zone was independent of titanium concentration. Inclusions constituted approximately 6 percent of the fusion zone microstructure. However, when titanium was added to the weld, the fraction of inclusions at the grain

boundaries increased. In the unrefined weld, 15 percent of the inclusions were located at the grain boundaries. With 0.8 and 1.2 weight percent titanium in the fusion zone, 43 and 50 percent of the inclusions were found at the grain boundaries, respectively. Figure 5 shows the typical inclusion distribution as a function of titanium concentration. At 1.2 weight percent titanium, numerous grain boundaries were almost completely coated with inclusions.

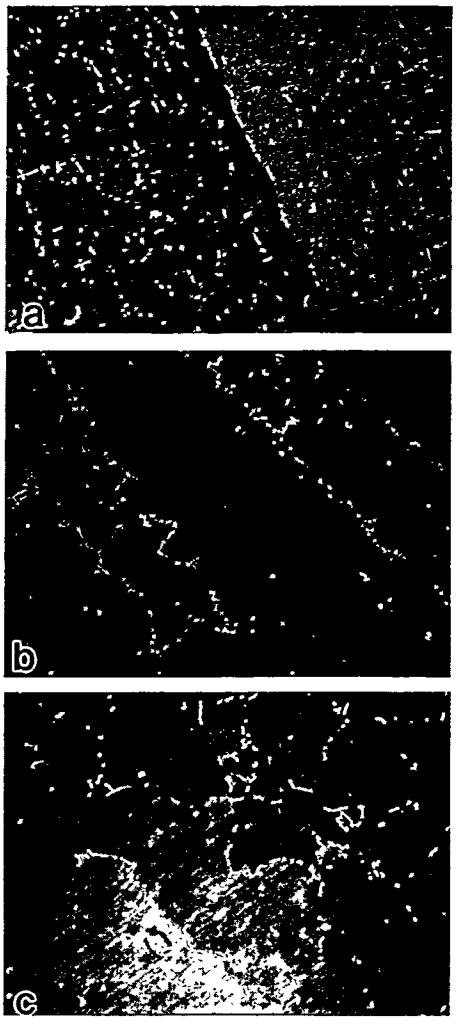

Fig. 5. Inclusion distribution in titanium inoculated welds. a) 0% Ti, b) 0.8% Ti, c) 1.2% Ti (700X)

Given the intrinsically brittle behavior of iron aluminides, fracture initiation is what must be controlled. Fracture is initiated at the weakest point in the weldment and the initiated crack becomes unstable when a critical length is reached. The inclusions located at the grain boundaries may be low stress crack initiation sites. With an applied stress, the interface between the inclusion at the grain boundary and the matrix can be broken, creating a critical crack, which in turn, causes the sample to fail. Inclusions may also be broken by the applied stress, again creating a critical crack. Figure 6 shows both failed interfaces as well a fractured inclusion observed in an inoculated weldment.

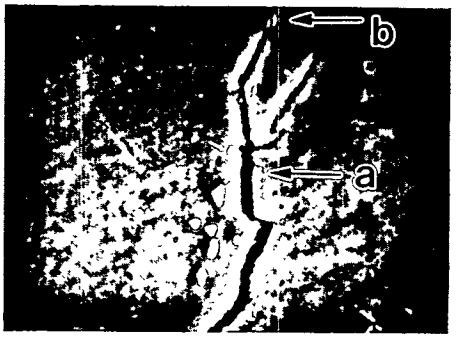

Fig. 6. Weld pool inclusions associated with fracture.
a) Failed inclusion/matrix interface b) Cracked inclusion (3500X)

A final possible effect of titanium may be an increase in porosity which is related to an increased hydrogen content in the weld pool. At thermodynamic equilibrium, the water, hydrogen, and oxygen concentrations are given by the relationship given in Equation 1.

$$[H_2O] = k\,[H]^2[O] \qquad [1]$$

As titanium and aluminum form oxides in the weld pool, the oxygen concentration decreases and the hydrogen concentration increases to maintain the equilibrium equation given in Equation 1. The increased hydrogen could cause higher porosity levels in the fusion zone. Figure 7 shows porosity observed in the area of inclusions in an inoculated fusion zone. Large pores can act as stress concentrators or in an extreme case, the pore diameter may approach the critical crack length.

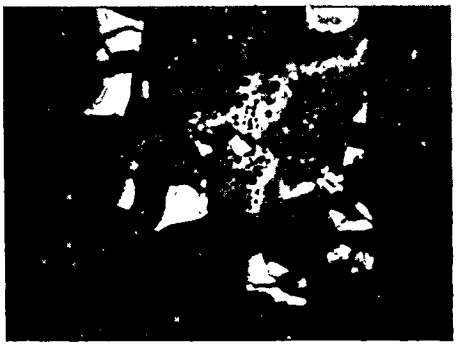

Fig. 7. Porosity in inoculated fusion zone. (2100X)

CONCLUSIONS

The following conclusions can be reached from the results of the study:

1. Titanium additions effectively refine the fusion zone microstructure in FA-129 weldments.
2. The average fusion zone grain size in FA-129 inoculated welds decreases with increasing titanium concentration.
3. Slow travel speeds, regardless of heat input, are required for titanium inoculation to effectively refine the fusion zone microstructure.
4. Higher heat inputs improve the fusion zone microstructure uniformity when welding with a slow travel speed.
5. Titanium additions change the distribution of inclusions in FA-129 welds.
6. During slow strain rate tensile testing, the fracture stress of the fusion zone decreases with increasing titanium concentration.

CURRENT WORK

Work currently focuses on determining the weldability and mechanical properties of zirconium-containing iron aluminides. Work done at Oak Ridge National Laboratory has shown that the zirconium and carbon concentration in a base alloy of iron, aluminum, and chromium greatly affect the mechanical properties of the alloy[2]. To determine the effect of zirconium and carbon on weldment properties, two heats of material were cast with the following compositions (all atomic percents): Fe - 28.0% Al - 5.00% Cr and Fe - 28.0% Al - 5.00% Cr - 0.50% Zr - 0.05% C. Welds have been made on tensile samples in an inert environment for slow strain rate (2.78×10^{-6} s^{-1}) tensile testing in atmospheres of varying water vapor concentration (approximately 0 - 9000ppm).

Preliminary results show that the addition of zirconium and carbon increases the fracture stress of the weldments and that neither the ternary alloy nor the zirconium-containing alloy have shown a fracture sensitivity to the water vapor concentration present during slow strain rate tensile testing. This may indicate less susceptibility of the alloys to hydrogen cracking. With FA-129, the fracture stress decreased with increasing water vapor concentration.

With the zirconium addition, the fracture behavior is the same as seen in alloy FA-129. Once a crack is nucleated, crack growth becomes unstable and the sample completely fractures. In the ternary alloy, however, once a crack is initiated the sample does not fail, allowing the M.T.S. to adjust the applied load. The crack then propagates in a stable manner across the sample. Without a reduced section added to the tensile sample, the ternary alloy fails along the weld centerline, while the zirconium-containing alloy fails in the heat affected zone/fusion line region.

The greatest issue with the zirconium-containing alloy is its weldability. Hot cracking has been observed more frequently than was seen with alloy FA-129 or is currently experienced with the ternary alloy. Future work should therefore focus on determining the effect of zirconium and carbon concentrations on the hot cracking susceptibility of the alloys.

REFERENCES

1. A. A. Fasching, "Grain Refinement and Hydrogen Embrittlement in Iron Aluminide Alloy FA-129 Weldments," Thesis #T-4686, Colorado School of Mines, Golden, CO, May 1995.

2. V. K. Sikka, Oak Ridge National Laboratory, Unpublished data.

EVALUATION OF IRON ALUMINIDE WELD OVERLAYS FOR EROSION-CORROSION RESISTANT BOILER TUBE COATINGS IN LOW NOx BOILERS

J.N. DuPont, S. W. Banovic, and A.R. Marder

Energy Research Center

Lehigh University

Bethlehem, PA 18015

ABSTRACT

Low NOx burners are being installed in many fossil fired power plants in order to comply with new Clean Air Regulations. Due to the operating characteristics of these burners, boiler tube sulfidation corrosion is often enhanced and premature tube failures can occur. Failures due to oxidation and solid particle erosion are also a concern. A program was initiated in early 1996 to evaluate the use of iron aluminide weld overlays for erosion/corrosion protection of boiler tubes in Low Nox boilers. Composite iron/aluminum wires will be used with the Gas Metal Arc Welding (GMAW) process to prepare overlays on boiler tubes steels with aluminum contents from 8 to 16wt%. The weldability of the composite wires will be evaluated as a function of chemical composition and welding parameters. The effect of overlay composition on corrosion (oxidation and sulfidation) and solid particle erosion will also be evaluated. The laboratory studies will be complemented by field exposures of both iron aluminide weld overlays and co-extruded tubing under actual boiler conditions.

INTRODUCTION

Under new clean air regulations, electric utility companies will be required to operate under boiler conditions which reduce NOx emissions. The new operating conditions use a fuel-rich reducing gas to lower NOx emissions. The boiler environment created by this approach often inhibits the formation of protective surface oxide scales in localized regions of the boiler and promotes sulfide scale formation, thus accelerating boiler tube corrosion rates. This new operating environment places a greater need on high performance coatings for boiler tube life extension. Through sponsorship of an electric utility consortium, research has been initiated to evaluate commercially available stainless steel and nickel based weld overlay coatings for erosion and corrosion protection in these low NOx boiler environments. Recent research on the corrosion and erosion of iron aluminide weld overlays indicates these alloys are also an excellent candidate for this application[1,2]. Therefore, the program was expanded in early 1996 through sponsorship of the Fossil Energy Advanced Research and Technology Development (AR&TD) Program to include the evaluation of iron aluminide weld overlays with deposit aluminum contents from 8 to 16 wt% Al. The main objectives of this research are to: 1) Develop wires for GMAW overlay applications and 2) Develop overlay compositions with good sulfidation resistance that are readily weldable.

DISCUSSION OF CURRENT ACTIVITIES

Wire Fabrication

The deposition of weld overlays on boiler tube waterwalls often requires application of very large surface areas under field conditions. Thus, a high deposition rate process such as GMAW must be utilized. Although iron aluminide consumables

can be prepared in rod and powder form for use with the Gas Tungsten Arc Welding (GTAW) and Plasma Arc Welding (PAW) processes, these processes typically operate at low deposition rates due to their inherently low thermal efficiency [3,4]. Therefore, a technique is required for fabricating spooled wire for the GMAW process. Preparation of small diameter iron aluminide wires for GMAW is impractical due to relatively low ductility. A composite wire fabrication technique has been devised and implemented by Stoody Company of Bowling Green, KY. With this process, a commercially pure aluminum wire is wrapped in a low carbon steel sheath and drawn to the final diameter. Additional alloying elements (e.g., Cr and Zr) can be added between the aluminum core wire and steel sheath during the drawing process. A typical wire prepared with this technique containing 22wt%Al - 8wt%Cr - 0.40wt%Zr is shown in Figure 1. At this early stage in the program, four additional wire compositions are being fabricated (Table 1) for future studies on corrosion, erosion, and weldability.

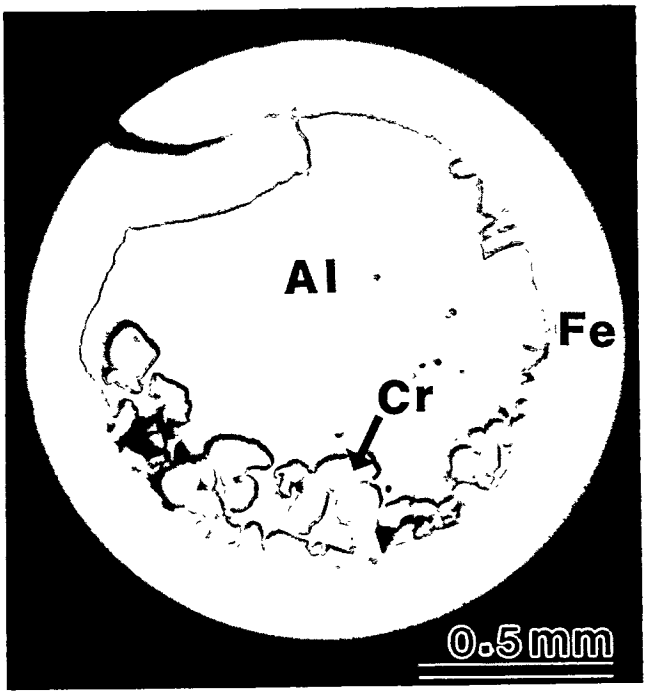

Figure 1. Cross-sectional photomacrograph of composite Fe-Al-Cr-Zr wire used to deposit weld overlays with the GMAW process.

Table 1. Chemical composition of composite iron/aluminum wires selected for weldability and corrosion studies.

Overlay/Wire Number	Al (wt%)	Cr (wt%)	Mo (wt%)	C (wt%)	B (wppm)	Zr (wt%)
Wire-1	21.3	0	0.4	0.1	25-50	0.25
Wire-2	21.3	6.7	0.4	0.1	25-50	0.25
Wire-3	10.5	0	0.4	0.1	25-50	0.25
Wire 4	10.5	6.7	0.4	0.1	25-50	0.25

FUTURE WORK

The alloys listed in Table 1 will be utilized to prepare GMAW weld overlays with varying compositions. The erosion resistance of each overlay will be evaluated at 500°C using particle impact angles of 30° and 90°. Weldability (resistance to hydrogen cracking) will be evaluated as a function of overlay composition and welding parameters (e.g., preheat, interpass temperature, postweld heat treatment temperature). The corrosion resistance will be evaluated quantitatively using thermo-gravimetric techniques in an H_2-H_2S containing gas. Qualitative long term corrosion evaluations will also be conducted in tube furnaces under identical conditions. The results of these studies will be compared to results of similar research being conducted on commercially available stainless steel and nickel based weld overlays.

REFERENCES

1. 5. J.H. DeVan and P.F. Tortorelli, Paper No. 127, Corrosion 92, NACE, 1992.

2. B.F. Levin, J.N. DuPont, and A.R. Marder, Weld Overlay Coatings for Erosion Control, *Proceedings of the TMS Symposium on High Temperature Coatings*, Chicago, Illinois, October 2-6, 1994, pp 325-340.

3. J.N. DuPont and A.R. Marder, Thermal Efficiency of Arc Welding Processes, *Welding Journal,* December, 1995, pp 406s-416s.

4. J.N. DuPont and A.R. Marder, Dilution in Single Pass Arc Welds, accepted for publication in *Metallurgical Transactions B*, June, 1996.

EFFECTS OF SURFACE CONDITION ON AQUEOUS CORROSION AND ENVIRONMENTAL EMBRITTLEMENT OF IRON ALUMINIDES

R. L. Perrin and R. A. Buchanan

Dept. of Materials Science and Engineering
University of Tennessee
Knoxville, TN 37996-2200

ABSTRACT

Effects of retained high-temperature surface oxides, produced during thermomechanical processing and/or heat treatment, on the aqueous-corrosion and environmental-embrittlement characteristics of Fe_3Al-based iron aluminides (FA-84, FA-129 and FAL-Mo), a FeAl-based iron aluminide (FA-385), and a disordered low-aluminum Fe-Al alloy (FAPY) were evaluated. All tests were conducted at room temperature in a mild acid-chloride solution. In cyclic-anodic-polarization testing for aqueous-corrosion behavior, the surface conditions examined were: as-received (i.e., with the retained high-temperature oxides), mechanically cleaned and chemically cleaned. For all materials, the polarization tests showed the critical pitting potentials to be significantly lower in the as-received condition than in the mechanically-cleaned and chemically-cleaned conditions. These results indicate detrimental effects of the retained high-temperature oxides in terms of increased susceptibilities to localized corrosion. In 200-hour U-bend stress-corrosion-cracking tests for environmental-embrittlement behavior, conducted at open-circuit corrosion potentials and at a hydrogen-charging potential of -1500 mV (SHE), the above materials (except FA-385) were examined with retained oxides and with mechanically cleaned surfaces. At the open-circuit corrosion potentials, none of the materials in either surface condition underwent cracking. At the hydrogen-charging potential, none of the materials with retained oxides underwent cracking, but FA-84, FA-129 and FAL-Mo in the mechanically cleaned condition did undergo cracking. These results suggest beneficial effects of the retained high-temperature oxides in terms of increased resistance to environmental hydrogen embrittlement.

INTRODUCTION

The overall objective of this project was to study the effects of retained high-temperature surface oxides, produced during thermomechanical processing and/or heat treatment, on the aqueous-corrosion and environmental-embrittlement characteristics of several Fe_3Al-based iron aluminides, an FeAl-based iron aluminide, and a low-aluminum Fe-Al alloy. Previous aqueous-corrosion studies of these materials by the present authors and colleagues have examined specimens only with cleaned surfaces (i.e., mechanically ground or polished surfaces).[1-4] The high-temperature surface oxides of the present study are not likely to have the same chemistry nor the same morphology (e.g., thermal cracking) as the passive films formed naturally on a clean surface in an aqueous environment. It was hypothesized that

the presence of the high-temperature oxides could modify both the resistance to localized corrosion and the resistance to environmental embrittlement. To address these issues, the project involved cyclic-anodic-polarization testing to evaluate aqueous-corrosion behavior and U-bend stress-corrosion-cracking to evaluate environmental-embrittlement behavior.

In the mild acid-chloride solution employed in this study, which was designed to simulate aggressive atmospheric-corrosion, the alloys evaluated are susceptible, to various degrees, to pitting corrosion. An excellent method for evaluating the relative pitting-corrosion susceptibility involves producing and analyzing cyclic anodic polarization curves. A schematic illustration of such a curve is shown in Figure 1, where certain electrochemical parameters are identified.

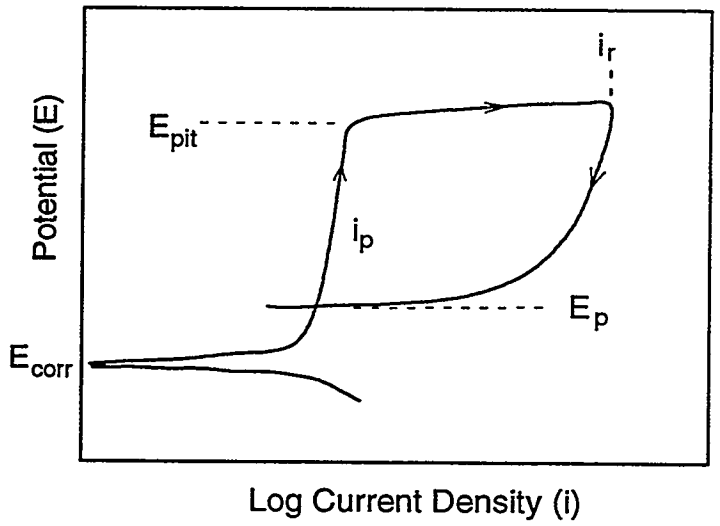

Fig. 1. Schematic illustration of cyclic anodic polarization behavior.

To produce the curve, the corrosion sample first is allowed to stabilize in the electrolyte such that a steady-state, open-circuit, corrosion potential, E_{corr}, is established. Next, with a potentiostatic circuit, the potential of the sample, E, is forced in the positive direction at a given rate while the current density, i, is continuously measured. After the potential has moved away from E_{corr} by a relatively small amount ($\approx$ 50 mV), the current density is directly proportional to the corrosion rate. The potential scan is continued in the positive direction until a predetermined reversing current density, i_r, is reached. At this point, the potential scan direction is reversed, moving in the negative direction, and continued until a very low current density is achieved. In Figure 1, the nearly vertical region in the up-scan portion of the curve, characterized by an average passive current density, i_p, is reflective of passivation, where the material has developed a thin protective oxide/hydroxide passive film, and,

therefore, corrodes at a very low rate over a range of potentials. At the critical pitting potential, E_{pit}, pitting corrosion initiates, with a sharp increase in current density. The pitting corrosion accelerates to i_r, and continues during the down-scan portion of the curve until the protection (or repassivation) potential, E_p, is reached (which corresponds to the cross-over point for the up-scan and down-scan curves). With reference to Figure 1, two of the parameters often used to characterize relative resistance to pitting corrosion are: (1) the magnitude of E_{pit}, with higher values corresponding to greater pitting resistance, and (2) the difference between E_{pit} and E_{corr}, i.e., $(E_{pit} - E_{corr})$, with higher values corresponding to greater pitting resistance.

EXPERIMENTAL PROCEDURES

Cyclic anodic polarization tests were conducted at room temperature in a mild acid-chloride solution (pH = 4, 200 ppm Cl^-) on the following materials: the Fe_3Al-based iron aluminides, FA-84 (Fe-28Al-2Cr-0.05B, at. %), FA-129 (Fe-28Al-5Cr-0.5Nb-0.2C, at. %), and FAL-Mo (Fe-28Al-5Cr-1Mo-0.04B-0.08Zr, at. %), a disordered low-aluminum Fe-Al alloy, FAPY (Fe-16.1Al-5.4Cr-1.1Mo-0.1C, at. %), and an FeAl-based iron aluminide, FA-385 (Fe-35.65Al-0.20Mo-0.05Zr-0.11C, at. %). The FA-84, FA-129, FAL-Mo, and FAPY materials, in as-processed sheet form, were kindly supplied by Dr. Vinod Sikka of the Oak Ridge National Laboratory (ORNL); the FA-385 material, in rod form with a cladding, was kindly supplied by Dr. Philip Maziasz of ORNL.

For the FA-84, FA-129, FAL-Mo, and FAPY materials, the surface conditions evaluated were: (1) as-processed (i.e., with the retained high-temperature oxides characteristic of the prior thermomechanical processing methods), (2) mechanically cleaned (ground through 600-grit SiC paper to remove all high-temperature oxides), and (3) chemically cleaned (immersed in an acid solution until all high-temperature oxides were removed (approximately 30 minutes), then immersed in 10% HNO_3 at 43 °C for one hour as a passivation treatment). Specifically, the thermomechanical processing procedures (accomplished at ORNL) for the as-processed condition were: hot forged 50% at 1000 °C, hot rolled 50% at 800 °C, and warm rolled 70% at 650 °C to a finish thickness of 0.75 mm. The acid solutions employed for chemical cleaning varied with the material, as follows: FA-84, 10% HNO_3 at 43 °C; FA-129, 10% HNO_3 plus 2% HF at room temperature; FAL-Mo, 10% HNO_3 plus 2% HF at 43 °C; and FAPY, no HNO_3/HF/temperature combination was found to satisfactorily remove the oxide and produce a smooth surface. Because of the form of the as-received FA-385 material (rods with protective claddings), it did not have the high-temperature oxides. To create the high-temperature-oxide surface condition, the FA-385 samples were annealed in air at 750 °C for one hour, then air

cooled. This condition will be referred to as the "heat treated" condition, not as the as-processed condition. The mechanically-cleaned condition was accomplished in the same manner as described for the other materials.

Cyclic anodic polarization tests were performed with a standard polarization cell and an EG&G Model 273 potentiostat. Each sample was mounted in epoxy, attached and electrically connected to a sample holder, and placed in a polarization cell containing the mild acid-chloride electrolyte. Stabilization was allowed to occur for at least one hour, after which E_{corr} was measured. The cyclic polarization curve was then generated at a scan rate of 600 mV/h. The reversing current density was 1000 $\mu A/cm^2$.

U-bend stress corrosion cracking tests were performed on the above alloys (except FA-385). Sheet material was cut into 1 cm by 11.9 cm strips and then the thermomechanical oxide was mechanically removed (600-grit SiC). The strips were heat treated in air at 750°C for one hour and then quenched in oil. Half of the strips were mechanically cleaned once again to remove the furnace oxide. The strips were bent to a radius of 15.9 mm, thus forming the U-bend specimen geometry illustrated in Figure 2. Each specimen was fastened into the U-bend shape by means of a polyvinyl chloride bolt so as to eliminate galvanic corrosion effects. The total strain in the bend was determined by the relation (ASTM G 30), $\varepsilon = T/2R$, where T is the specimen thickness and R the bend radius. The total strain placed on the U-bend specimens ranged from 0.024 to 0.037 cm/cm. Due to an inability to reliably produce a chemically-cleaned surface for all alloys, this surface condition was not evaluated. Testing of the U-bend specimens was conducted in the same mild acid-chloride solution employed in the polarization tests.

One series of U-bend tests was conducted at the open-circuit corrosion potential, E_{corr}, which was monitored continuously for 200 hours. A second series of tests was conducted at a hydrogen-charging potential of -1500 mV(SHE) to enhance the production of hydrogen at the specimen surfaces. In this series of tests, the cathodic current density was monitored continuously.

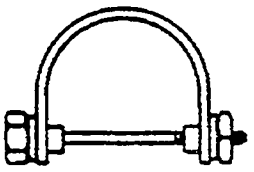

Fig. 2: Schematic geometry of U-bend test specimen.

RESULTS AND DISCUSSION

The cyclic anodic polarization behaviors of FA-84 (28Al-2Cr) in the as-processed, mechanically-cleaned, and chemically cleaned surface conditions are shown in Figure 3. The as-processed condition, relative to the mechanically-cleaned and chemically cleaned conditions, produced a lower pitting potential (E_{pit}), and a higher corrosion potential (E_{corr}). Both the lower E_{pit} value and the lower (E_{pit} - E_{corr}) value for the as-processed (high-temperature oxide) surface condition indicated reduced resistance to pitting corrosion. The decreased passive current density, i_p, for the chemically cleaned surface suggested that the chemical cleaning process enhanced the properties of the passive film, most likely by thickening it.

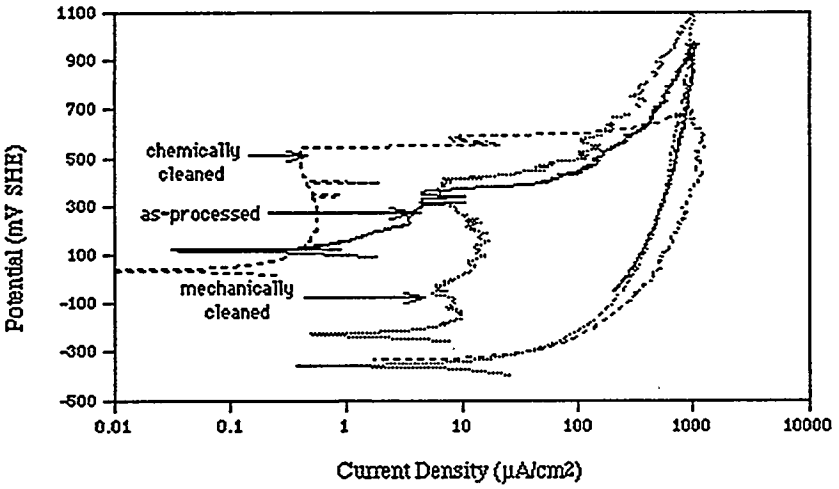

Fig. 3. Cyclic anodic polarization behaviors of FA-84 with as-processed, mechanically-cleaned, and chemically-cleaned surfaces.

As seen in Figure 4 for the FA-129 (28Al-5Cr) alloy, the as-processed surface condition performed poorly with respect to both the mechanically-cleaned and chemically-cleaned surface conditions. The as-processed surface condition showed almost no tendency for passivation. For the as-processed surface, the pitting potential was significantly lower, and the corrosion potential higher, than for the other two conditions which involved removal of the high-temperature oxide. Again, both the lower E_{pit} value and the lower (E_{pit} - E_{corr}) value for the as-processed surface condition indicated reduced resistance to pitting corrosion.

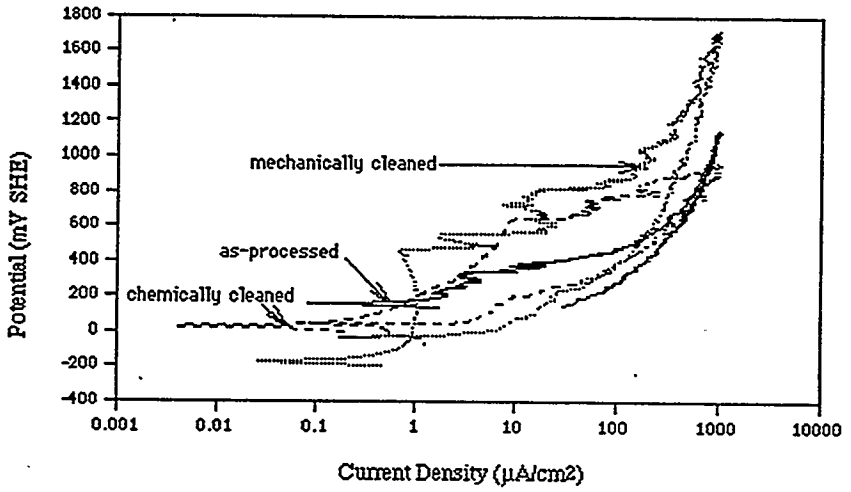

Fig 4. Cyclic anodic polarization behaviors of FA-129 with as-processed, mechanically-cleaned, and chemically-cleaned surfaces.

As seen in Figure 5 for the FAL-Mo (28Al-5Cr-1Mo) alloy, the pitting potential, E_{pit}, for the as-processed surface condition was significantly lower than the E_{pit} values for the mechanically-cleaned and chemically-cleaned surfaces. Also, the range of the passive current density, i_p, was rather small for the as-processed surface condition. It also is noted that the high-temperature oxide on the as-processed surface did not produce a stable i_p, i.e., current-density fluctuations were obvious. The mechanically and chemically cleaned conditions each had certain advantages. The mechanically-cleaned surface had a slightly higher E_{pit} and a lower E_{corr}. However, the chemically cleaned surface had a significantly lower i_p. The lower i_p suggested that there was either a thickening of the passive film or possibly a Cr enrichment of the passive film caused by the chemical cleaning process.

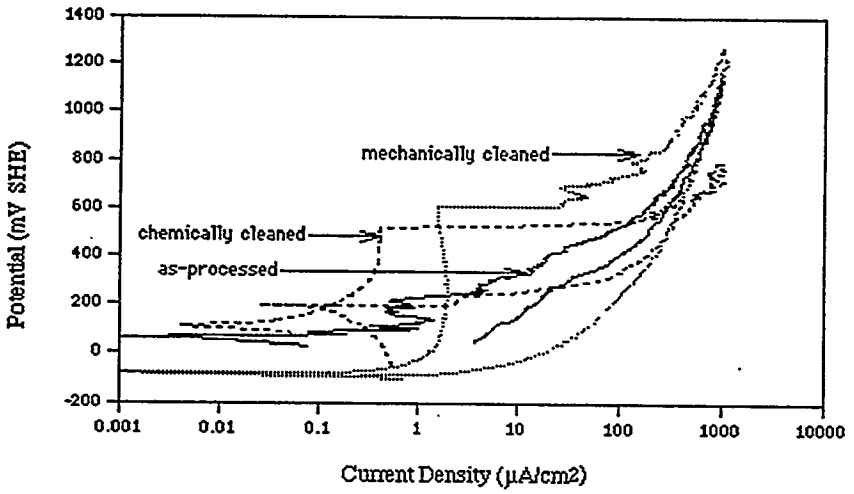

Fig 5. Cyclic anodic polarization behaviors of FAL-Mo with as-processed, mechanically-cleaned, and chemically-cleaned surfaces.

The cyclic anodic polarization behaviors of the disordered alloy, FAPY (16Al-5Cr-1Mo), in the as-processed and mechanically-cleaned surface conditions are shown in Figure 6. A chemically-cleaned surface could not be produced that was sufficiently smooth so as not to promote a surface roughness effect during the polarization test. Once again, the as-processed surface performed poorly in comparison to the mechanically-cleaned surface. The as-processed surface condition produced a much lower E_{pit}, with little indication of a passive current density, i_p, and a much higher E_{corr} value.

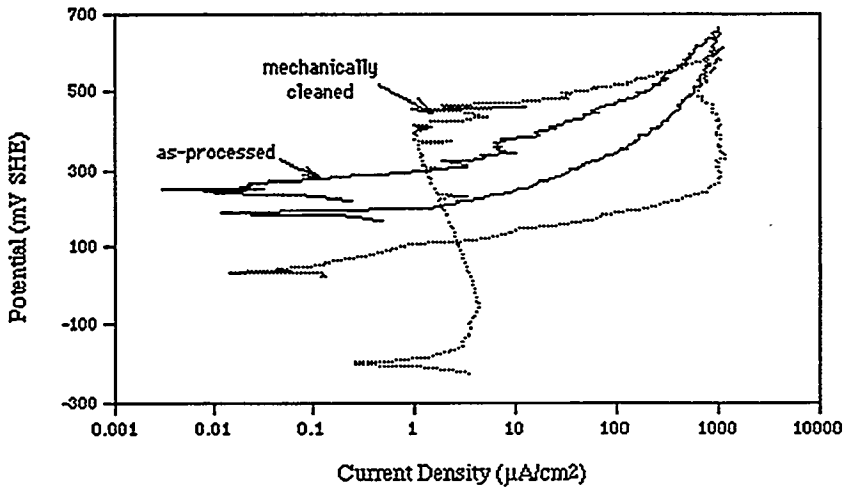

Fig 6. Cyclic anodic polarization behaviors of FAPY with as-processed and mechanically-cleaned surfaces.

As seen in Figure 7 for the FeAl-based iron aluminide, FA-385 (36Al-0.2Mo), the heat-treated high-temperature-oxide surface condition produced a much lower E_{pit}, a much lower i_p, and a higher E_{corr} value than the mechanically-cleaned surface condition. Both the lower E_{pit} value and the lower (E_{pit} - E_{corr}) value for the high-temperature-oxide surface condition indicated reduced resistance to pitting corrosion.

An observation that did not manifest itself directly in the polarization behavior was the appearance of the surfaces of the samples after chemical cleaning. The high-temperature-oxide surfaces of FA-84 and FA-129 were cleaned rather easily in the 10% HNO_3, 2% HF solution but also could be cleaned in a solution containing only 10% HNO_3. However, the oxide surfaces of FAL-Mo and FAPY were slow to clean in the 10% HNO_3, 2% HF solution, and could not be cleaned at all in the 10% HNO_3 solution. Furthermore, after chemical cleaning, the FA-129 and FA-84 samples had shiny smooth surfaces, whereas the FAL-Mo and FAPY samples had shiny rough surfaces. For the FAL-Mo and FAPY samples, the attack of the 10% HNO_3, 2% HF solution was more prominent in areas of exposed base material, i.e., cut faces or where the oxide had flaked off. The difficulties experienced in removal of the

high-temperature oxides apparently can be attributed to the presence of molybdenum in the FAL-Mo and FAPY alloys, which also is partly responsible for the greater aqueous-corrosion resistance exhibited by these alloys.

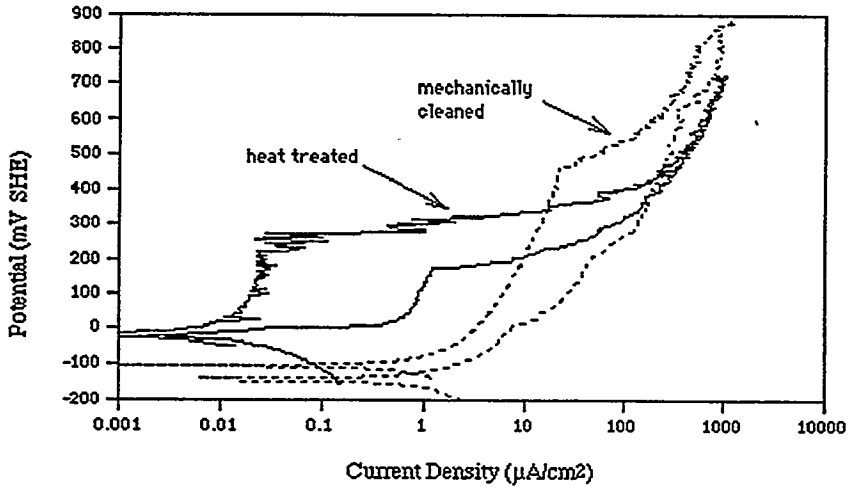

Fig 7. Cyclic anodic polarization behaviors of FA-385 with heat-treated and mechanically-cleaned surfaces.

With regard to the 200-hour U-bend stress-corrosion-cracking tests, the overall results in terms of cracking behavior are shown in Table 1. For the tests conducted at the corrosion potential, E_{corr}, none of the mechanically-cleaned nor furnace-oxide U-bend specimens underwent cracking. For the tests conducted at the hydrogen-charging potential, -1500 mV(SHE), although none of the furnace-oxide specimens underwent cracking, several of the mechanically-cleaned specimens did undergo cracking. Specifically, at the hydrogen-charging potential, specimens of FAL-Mo, FA-129, and FA-84 all experienced cracking in the mechanically-cleaned condition but not in the furnace-oxide condition. These results indicated that under severe hydrogen-producing conditions, the presence of the high-temperature oxides are beneficial in improving the resistance of the materials to environmental embrittlement.

For the U-bend tests conducted at the hydrogen-charging potential, the resultant cathodic current densities for the alloys in the two surface conditions are shown in Table 2 for time periods of 20 and 200 hours. The current densities are directly proportional to the amount of hydrogen cathodically produced at the specimen surfaces, but do not indicate the amount of atomic hydrogen diffusing into the material substrates. Generally (with the exception of FA-84), the cathodic current densities were lower for the furnace-oxide specimens at shorter times, but somewhat higher at longer times. Overall, it appeared that the high-temperature oxides did not prevent, in a major way, the production of

hydrogen at the oxide/solution interface, but rather functioned as barriers in retarding the diffusion of atomic hydrogen through the oxides and into the material substrates, thus reducing the hydrogen-embrittlement effect.

Table 1. 200-hour U-bend-test cracking results.

Alloy	Tests at Corrosion Potential, E_{corr}		Tests at Hydrogen-Charging Potential, -1500 mV SHE	
	Mechanically-Cleaned Surfaces	Furnace-Oxide Surfaces	Mechanically-Cleaned Surfaces	Furnace-Oxide Surfaces
FAL-Mo	No Cracking	No Cracking	Cracked (~190 h)	No Cracking
FA-129	No Cracking	No Cracking	Cracked (~23 h)	No Cracking
FA-84	No Cracking	No Cracking	Cracked (~190 h)	No Cracking
FAPY	No Cracking	No Cracking	No Cracking	No Cracking

Table 2. Cathodic current densities ($\mu A/cm^2$) during hydrogen charging.

Alloy	Mechanically-Cleaned Surfaces		Furnace-Oxide Surfaces	
	At 20 hours	At 200 hours	At 20 hours	At 200 hours
FAL-Mo	306	321	217	405
FA-129	445	425	351	435
FA-84	375	430	780	836
FAPY	327	346	323	499

CONCLUSIONS

Electrochemical aqueous-corrosion studies showed that retained high-temperature surface oxides on iron aluminides (FA-84, FA-129, FAL-Mo, and FA-385) and a related alloy (FAPY), produced during thermomechanical and/or heat treatment processing, caused major reductions in corrosion resistance in a mild acid-chloride electrolyte designed to simulate aggressive atmospheric corrosion. Removal of the oxides by mechanical grinding or chemical cleaning restored the corrosion resistance.

A standard pickling solution employed for stainless steels, nitric plus hydrofluoric acid, worked well for the iron aluminides not containing molybdenum (FA-84 and FA-129), producing a clean, smooth surface. However, for the molybdenum-containing materials (FAL-Mo and FAPY), although this solution was effective in removing the oxide, it produced an unacceptably rough surface.

U-bend stress-corrosion-cracking tests conducted in the mild acid-chloride electrolyte on FA-84, FA-129, FAL-Mo, and FAPY showed that under electrochemical hydrogen-charging conditions, specimens with mechanically-cleaned surfaces underwent cracking, whereas specimens with retained high-temperature furnace-oxide surfaces did not undergo cracking. The results suggest that the high-temperature oxide serves as a hydrogen diffusion barrier and , consequently, is beneficial in terms of improving resistance to environmental embrittlement.

REFERENCES

1. R. A. Buchanan and J. G. Kim, "Fe_3Al-Type Iron Aluminides: Aqueous Corrosion Properties in a Range of Electrolytes and Slow-Strain-Rate Ductilities During Aqueous Corrosion," Final Report, U. S. Dept. of Energy, Fossil Energy AR & TD Materials Program, ORNL/Sub/88-07685CT92/02, National Technical Information Service, Springfield, VA, August, 1992.

2. J. G. Kim and R. A. Buchanan, "Aqueous Corrosion Properties and Slow-Strain-Rate Ductilities of Fe_3Al-Based and Lean-Aluminum Iron Aluminides," Final Report, U. S. Dept. of Energy, Fossil Energy AR & TD Materials Program, ORNL/Sub/88-07685CT92/03, National Technical Information Service, Springfield, VA, August, 1993.

3. J. G. Kim and R. A. Buchanan, "Pitting and Crevice Corrosion of Iron Aluminides in a Mild Acid-Chloride Solution," Corrosion, Vol. 50, No. 9, pp. 658-668, Sept., 1994.

4. J. G. Kim and R. A. Buchanan, "Localized Corrosion and Stress Corrosion Cracking Characteristics of a Low-Aluminum-Content Iron Aluminum Alloy," Final Report, U. S. Dept. of Energy, Fossil Energy AR & TD Materials Program, ORNL/Sub/88-07685CT92/04, National Technical Information Service, Springfield, VA, October, 1994.

PROCESSING AND PROPERTIES OF LOW-ALUMINUM ALLOY FAPY

V. K. Sikka and C. R. Howell

Metals and Ceramics Division
Oak Ridge National Laboratory
P.O. Box 2008
Oak Ridge, Tennessee 37831-6083

F. Hall and J. Valykeo

Hoskins Manufacturing Company
10776 Hall Road
Hamburg, Michigan 48139

ABSTRACT

This paper deals with the melting, processing, properties, and microstructure of three commercially melted heats of Fe-16 at. % Al alloy FAPY. All of the heats were air-induction melted (AIM), two at Hoskins Manufacturing Company (Hamburg, Michigan) and one at United Defense (Anniston, Alabama). One ingot from each of the heats was used for testing at the Oak Ridge National Laboraotry. A 127-mm.-long section from each ingot was used for determining properties and microstructure in the as-cast, cast and hot-processed, and cold-rolled conditions. The fine-grained sheet showed 20% elongation at room temperature.

INTRODUCTION

The FAPY is an Fe-16 at. % Al alloy of nominal composition given in Table 1. The aluminum content of the alloy is such that it remains single phase (α) without the formation of an ordered phase (DO_3). The alloy has good oxidation resistance at temperatures up to 1000°C and has shown significantly superior performance as heating elements when compared to the commonly used nickel-based alloy, NICHROME® (Driver-Harris Company, Harrison, New Jersey). Although wire for the heating elements has been fabricated from small (6.8-kg) laboratory heats, for its commercial applications, the wire needs to be producible from large (545- to 680-kg) air-melted heats. The purpose of this study was to produce commercial-size heats and investigate their mechanical properties and microstructure in the as-cast, hot-worked, and cold-worked conditions. The results of this study are expected to provide: (1) insight into processing steps for large heats into wire under commercial conditions, and (2) the mechanical properties data on commercial-size heats in various product forms.

ALLOY PREPARATION AND PROCESSING

A total of three commercial-size heats were used in this study. Two heats of 545 kg each were air-induction melted (AIM) at Hoskins Manufacturing Company (Hamburg, Michigan) and cast into standard 203-mm tapered ingots. The third heat was processed by AIM at United Defense (Anniston, Alabama). This heat was primarily cast into various sand molds but was also cast into two ingot molds provided by Hoskins. One ingot each from the heats melted at Hoskins and United Defense were sent to the Oak Ridge National Laboratory (ORNL) for processing, property, and microstructural evaluation. The chemical analysis of each heat and the heat numbers are included in Table 1.

Table 1. Comparison of chemical analysis of two FAPY alloy heats made at Hoskins Manufacturing Company and one heat made at United Defense with the target composition

Element	Target	Weight percent		
		Hoskins Manufacturing Company		United Defense Heat 899-40299
		Heat 899-21689	Heat 899-21690	
Al	8.46	8.69	8.45	9.19
Cr	5.50	5.46	5.49	5.31
Zr	0.20	0.20	0.21	0.21
C	0.03	0.054	0.044	0.022
Mo	2.00	2.06	2.10	2.03
Y	0.10	0.13[a]	0.16[a]	0.04[a]
Mn	–	0.34	0.34	0.19
S	–	0.006	0.007	0.011
Nb	–	0.012	0.01	<0.01
B	–	<0.001	<0.001	*b*
N_2	–	0.003	0.002	0.003
O_2	–	0.003	0.003	0.002
Fe	*c*	*c*	*c*	*c*

[a]Estimated.
[b]Not analyzed.
[c]Balance.

A 127-mm-long section of each ingot was cut from the ingot bottom. The macrostructure of the cut sections of each ingot is shown in Fig. 1. The ingots cast at Hoskins were sound but showed a slightly different microstructure. The ingots cast at United Defense showed a crack in the cross section.

A 2-in.-thick slice was cut from the middle section of each of the 127-mm-long ingot sections. The remaining part of the ingot section was used for machining specimens in the as-cast condition. The 51-mm-thick slice was hot-forged 50% at 1150°C. The 25-mm-thick forged plate was hot-rolled at 1000°C to 13--mm-thick plate. This plate was used for machining longitudinal specimens for properties in the hot-rolled condition. A part of the 13-mm-thick plate was hot-rolled at 1000°C to 2.54-mm-thick sheet. This sheet was rolled to 1.3 mm thickness at 600°C, subsequently annealed for 1 h at 800°C, and cold-rolled to 0.76 mm thickness. The cold-rolled sheet was used to punch specimens for testing in the wrought condition.

A square bar of 61- by 61-mms cross section hot-rolled from an ingot at Hoskins was also included for testing.

ORNL Photo 2162-96

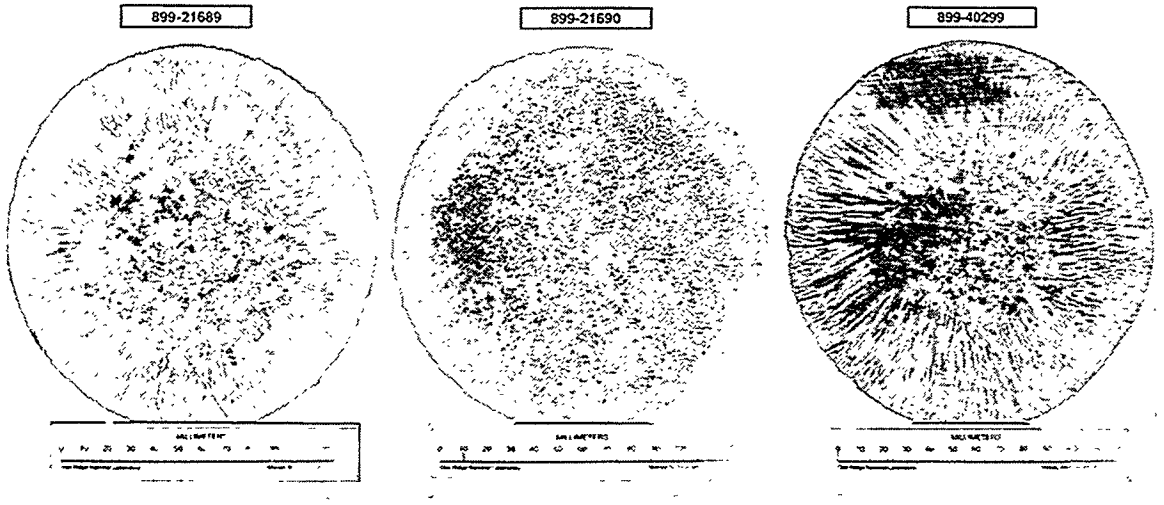

Fig. 1. Macrostructure of sections cut from three ingots of FAPY alloy.

Test bars machined from ingots, hot-rolled plate, hot-rolled bar, and punched from the sheet were all given a 1-h anneal at 800°C in air followed by air cooling prior to testing. In only one case, the sheet specimens were tested in the as-rolled condition, which contained 40% cold-work from the rolling process.

TENSILE TESTING AND PROPERTIES

Tensile tests (one per temperature) were carried out in air at temperatures varying from room temperature to 800°C. The strain rate for bar specimens was $2.7 \times 10^{-3}/s^{-1}$ and $3.3 \times 10^{-3}/s^{-1}$ for sheet specimens. The 0.2% yield strength, ultimate tensile strength, total elongation, and reduction of area for each heat are plotted as a function of test temperature in Figs. 2 and 3. The following observations are made from these figures:

1. The 0.2% yield strength of the as-cast ingot is the lowest from room temperature to 600°C and the highest for the sheet with the hot-rolled plate falling between the two. The cast/forged (bar-rolled) bar from Hoskins showed essentially the same yield strength as the sheet. The yield strength of the as-rolled sheet is significantly higher than the annealed sheet up to 400°C. At 600°C, the difference in yield strength between the cold-worked and annealed conditions is significantly reduced.
2. The ultimate tensile strength showed a clear distinction between the cast, hot-rolled, and cold-rolled sheet. At room temperature, ultimate tensile strength of the cast ingot was the lowest followed by the hot-rolled material and sheet. The cast/forged (bar-rolled) bar was lower in ultimate strength than the sheet. The as-rolled sheet showed substantially higher strength than the annealed sheet. Except for the

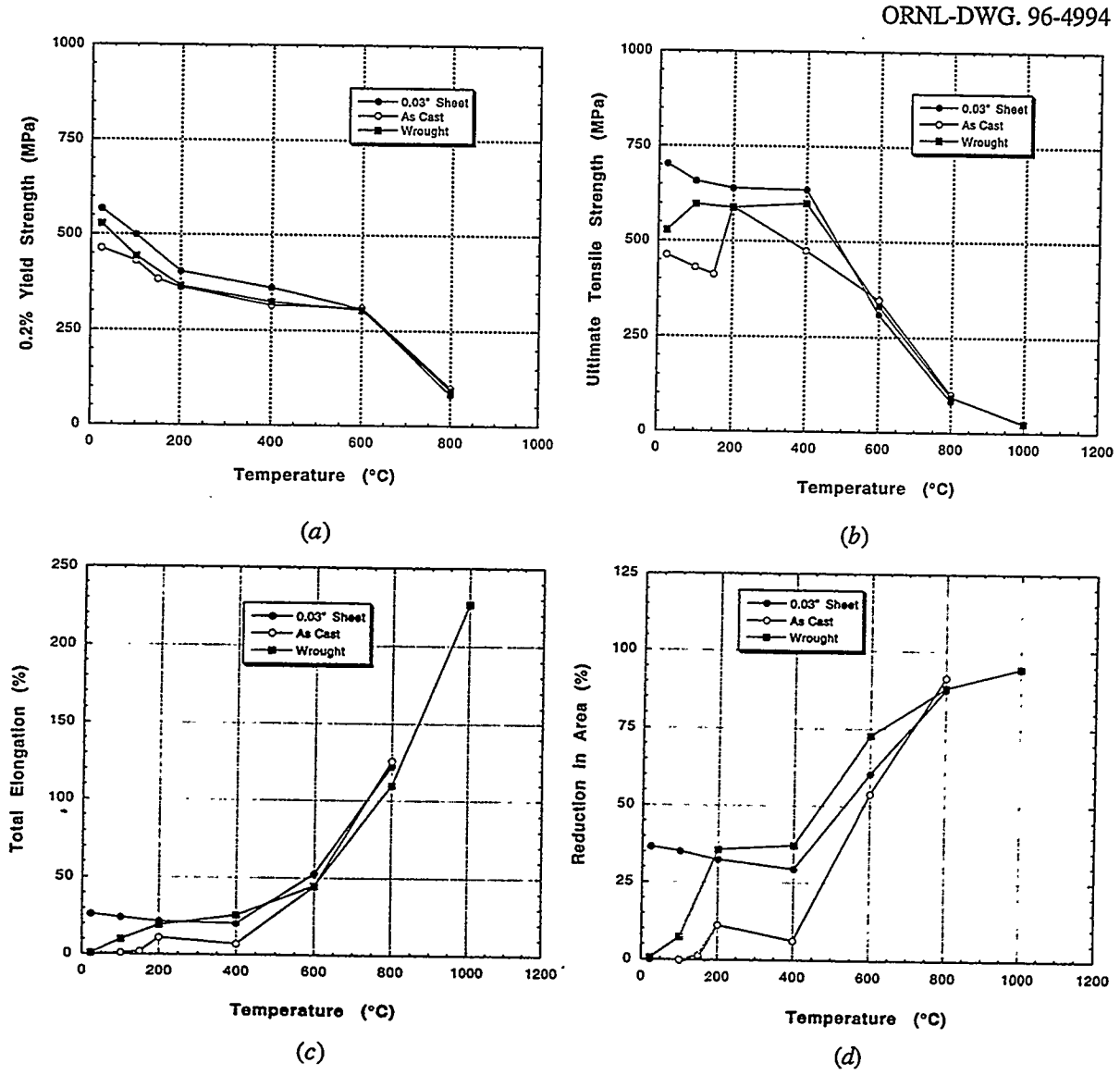

Fig. 2. Plots of tensile properties as a function of test temperature for FAPY heat 899-21690: (*a*) 0.2% yield strength, (*b*) ultimate tensile strength, (*c*) total elongation, and (*d*) reduction of area.

cast ingot, data for other products were well behaved for the entire test temperature range. The cast ingot data showed an unusual trend with temperature in the range from room temperature to < 200°C, where the cast ingot was tested in the brittle range [see the ductility data in Fig. 2(*c-d*)]. Some scatter in the data for the cast ingot may also be due to the variability in grain size from specimen to specimen.

3. The total elongation plots show that the cast ingot has the least ductility at room temperature and remains very low up to 150°C. It only increases to a reasonable level of 10% at 200°C. For the hot-rolled plate, ductility was very low at room temperature but increased to 10% at 100°C, and matched the

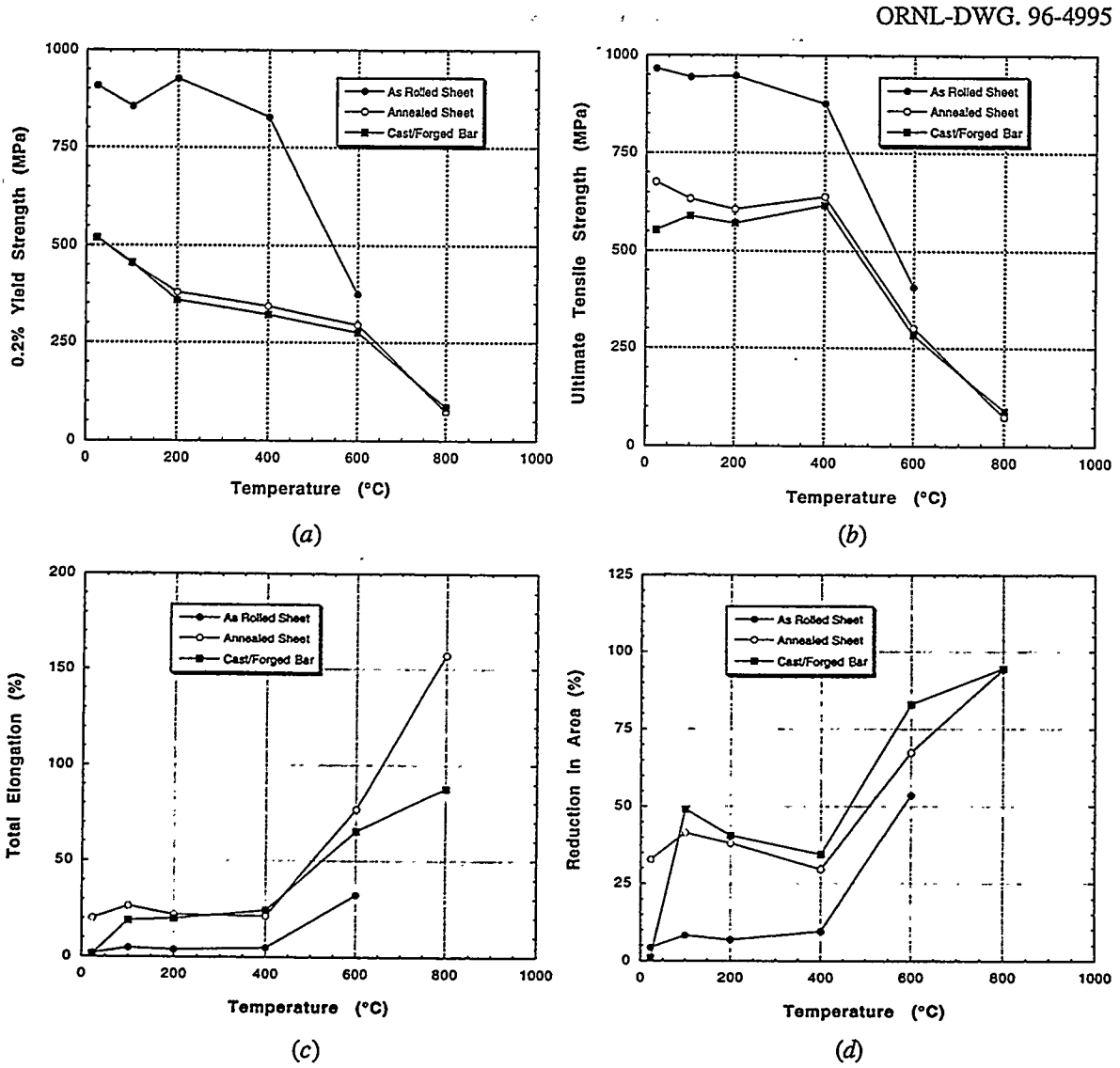

Fig. 3. Plots of tensile properties as a function of test temperature for FAPY heat 899-21689: (*a*) 0.2% yield strength, (*b*) ultimate tensile strength, (*c*) total elongation, and (*d*) reduction of area.

sheet ductility at 200°C. The cast/forged (bar-rolled) bar processed at Hoskins showed low ductility at room temperature, but it reached 20% at 100°C, which is nearly double the value for the plate hot rolled at ORNL. The annealed sheet showed approximately 20% value at room temperature, with no trends of brittle- (ductility of 51%) to-ductile (ductile defined as ≥ 10% elongation) transition. The as-rolled sheet with 40% cold-work showed values of 5% up to 600°C, where most of the cold-work appears to have recovered. It should be noted that the reduction in ductility of the as-rolled sheet is a consequence of cold-work (ductility exhaustion) and is different than the brittle-to-ductile trend observed for the cast and

hot-worked conditions. At 800°C, the FAPY alloy is very ductile in cast, hot-worked, and cold-rolled sheet. At 1000°C, the sheet approached the ductility values in the superplastic range (≥ 200%).

4. The reduction of area plots in Figs. 2 and 3(*d*) show trends very similar to those described above for total elongation with the exception that the brittle-to-ductile trends are clearer in these plots.

Optical microstructures of as-cast, cast and hot-rolled, and cold-rolled sheet are compared for heat 899-21690 of FAPY in Figs. 4 and 5. The microstructures in Fig. 5 are at low magnification, and those in Fig. 5 are at high magnification. These photomicrographs show that processing refines the grain size. The grain size (measured by line intersection method) of the cast ingot of 305 μm was reduced to 254 μm by hot-forging and hot-rolling to 0.5-in.-thick plate. However, hot-rolling to 2.5 mm thickness followed by warm-rolling at 600°C to 1.3 mm thickness and annealing at 800°C for 1 h followed by cold-rolling 40% to 0.76-mm thickness reduced the grain size to 13 μm (23 times finer than that of the cast ingot). The grain refinement is due to recrystallization of warm- and cold-rolled sheet. The as-cast microstructure in the photomicrographs also showed decoration of grain boundaries with precipitates and some particles in the matrix, and hot-forging and hot-rolling removed most of the particles from the grain boundaries, with some precipitates still present in the matrix.

ORNL Photo 2163-96

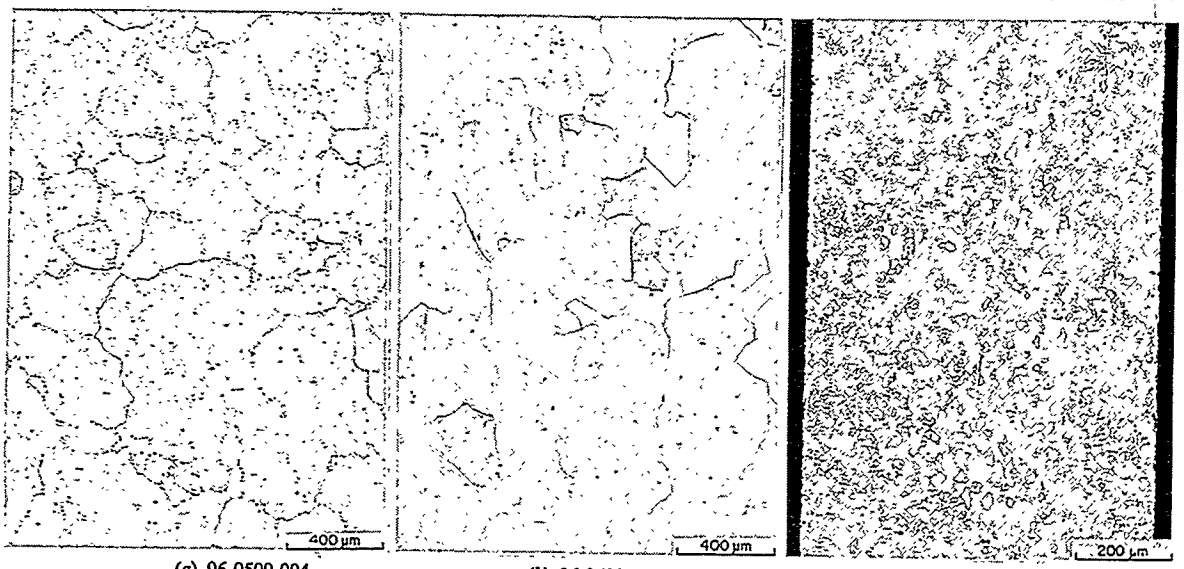

(*a*) 96-0509-004 (*b*) 96-0508-004 (*c*) 96-0507-004

Fig. 4. Comparison of low-magnification optical micrographs of: (*a*) as-cast, (*b*) cast and hot-worked, and (*c*) cold-rolled FAPY samples of heat 899-21690. The grain sizes in three conditions are 305, 254, and 13 μm, respectively.

ORNL Photo 2164-96

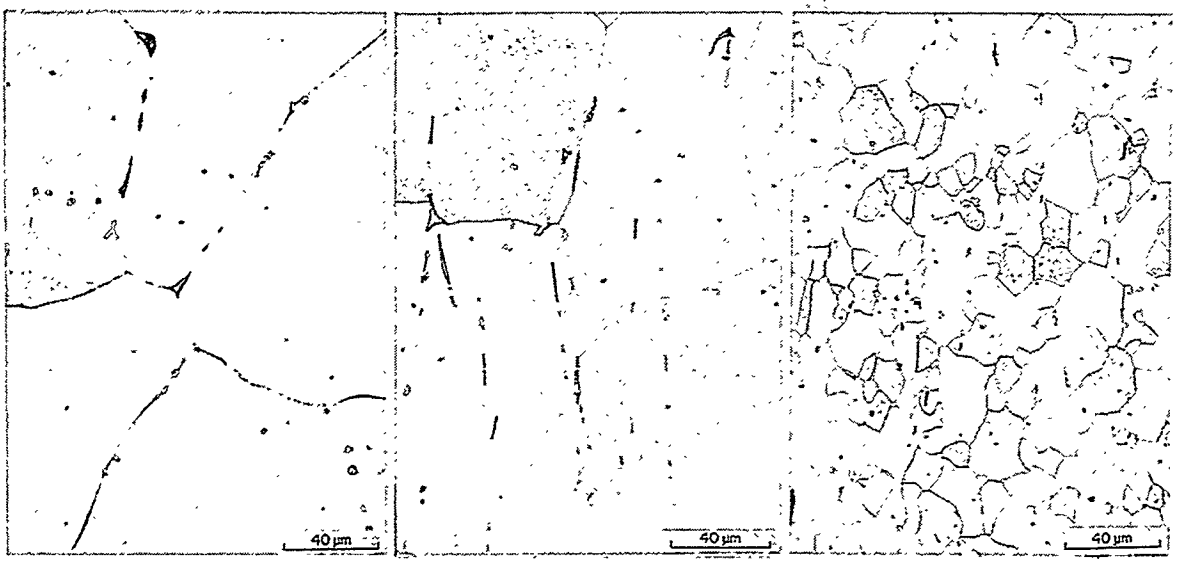

(a) 96-0509-006 (b) 96-0508-006 (c) 96-0507-006

Fig. 5. Comparison of high-magnification optical micrographs of: (*a*) as-cast, (*b*) cast and hot-worked, and (*c*) cold-rolled FAPY samples of heat 899-21690.

ORNL Photo 2181-96

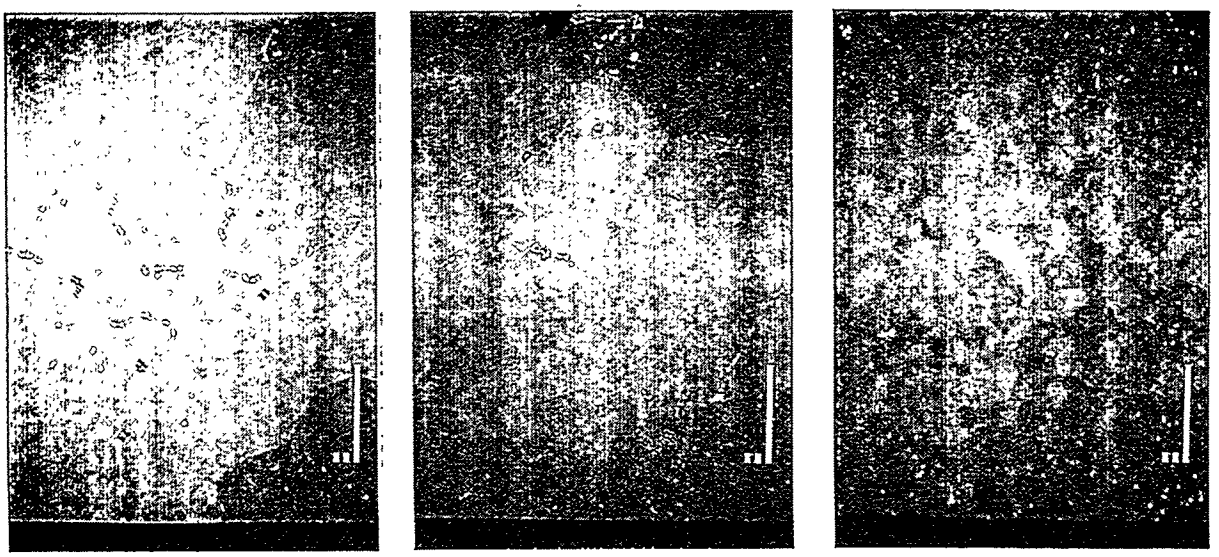

(a) 96-0509 (b) 96-0508 (c) 96-0507

Fig. 6. Backscattered electron images of FAPY alloy in: (*c*) as-cast, (*b*) cast and hot-worked, and (*c*) cold-rolled conditions.

Scanning electron microscope (SEM) analysis was carried out to determine the composition of the precipitates. The back-scattered electron images for the cast, hot-worked, and cold-rolled sheet are compared in Fig. 6. Two types of inclusions {bright [higher atomic number (Z)] and gray in color [intermediate atomic number (Z)]} were observed. Detailed compositional analyses at ten locations in the matrix and the particles are shown in Table 2. Based on these semiquantitive analyses, the bright particles are primarily ZrC with a very small amount of Fe and Y. The darker particles are highly enriched with Y and contain substantial amounts of Fe, Al, Cr, and C. The atomic percentages of various elements suggest that the Y-containing particles may be $(FeCrC)_3(AlY)$. The back-scattered electron images in Fig. 6 show that the ZrC- and Y-containing particle sizes become smaller with hot- and cold-processing, but their total estimated amount by area appears to remain nearly the same.

Table 2. Chemical analyses of matrix and precipitates[a] in the as-cast sample of FAPY heat 899-21689

Fe	Al	Cr	Mo	Zr	Y	C	Total
			Matrix				
75.8[b]	15.0	5.5	1.1	0.0	0.0	2.6	
84.6[c]	8.1	5.7	2.0	0.0	0.0	0.6	101.1
0.5[d]	0.1	0.1	0.1	–	–	0.2	
			High-Z Precipitates				
3.8	0.3	0.4	0.4	42.5	0.4	52.1	
4.6	0.2	0.4	0.8	83.6	0.9	13.5	104.1
2.7	0.2	0.2	0.2	3.6	0.7	0.2	
			Intermediate-Z Precipitates				
59.4	16.5	3.7	0.8	0.1	9.0	10.5	
67.9	9.1	4.0	1.5	0.2	16.3	2.6	101.6
0.4	0.1	0.2	0.1	0.1	0.2	0.1	

[a]The same precipitates were observed in the hot- and cold-worked specimens.
[b]Mean composition in normalized atomic percent.
[c]Mean composition in weight percent.
[d]SD = one standard deviation based on ten analyses and expressed in weight percent.

The fracture surface analysis by SEM (see Figs. 7 through 9) of specimens tested at room temperature yielded the following observations:

ORNL Photo 2182-96

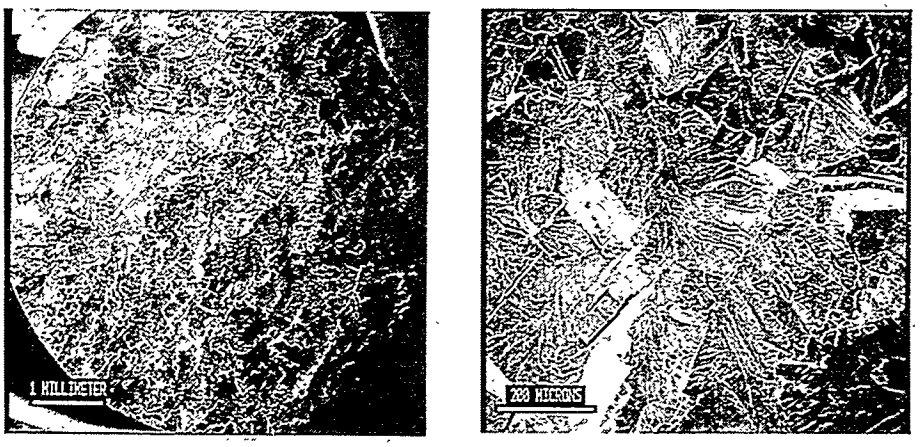

(*a*) 527 (*b*) 526

Fig. 7. Fracture surface of FAPY heat specimen 899-21690 in as-cast and hot-worked conditions tested at room temperature: (*a*) low and (*b*) high magnifications.

ORNL Photo 2183-96

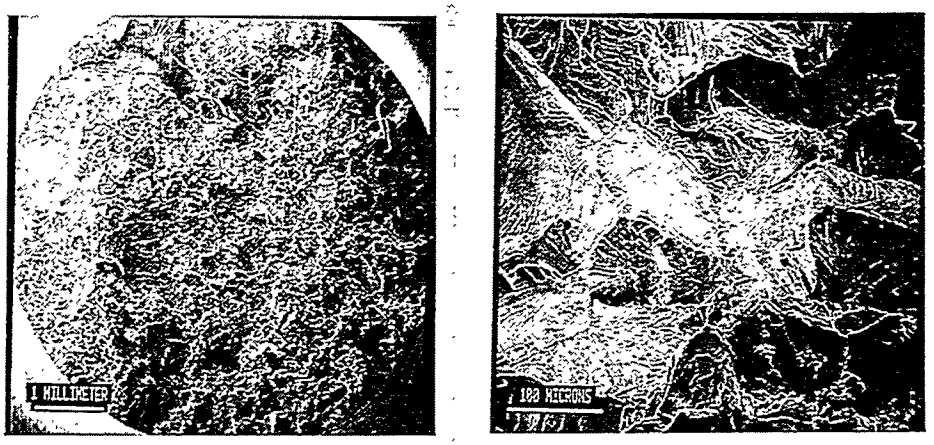

(*a*) 522 (*b*) 520

Fig. 8. Fracture surface of FAPY heat specimen 899-21690 in as-cast and hot-worked conditions tested at room temperature: (*a*) low and (*b*) high magnifications.

1. As cast: a mixed mode fracture consisting of intergranular separation with some cleavage occurring at the grain faces.
2. Cast and hot-worked: a mixed mode fracture consisting of intergranular separation with possibly more cleavage than the as-cast specimen.

ORNL Photo 2184-96

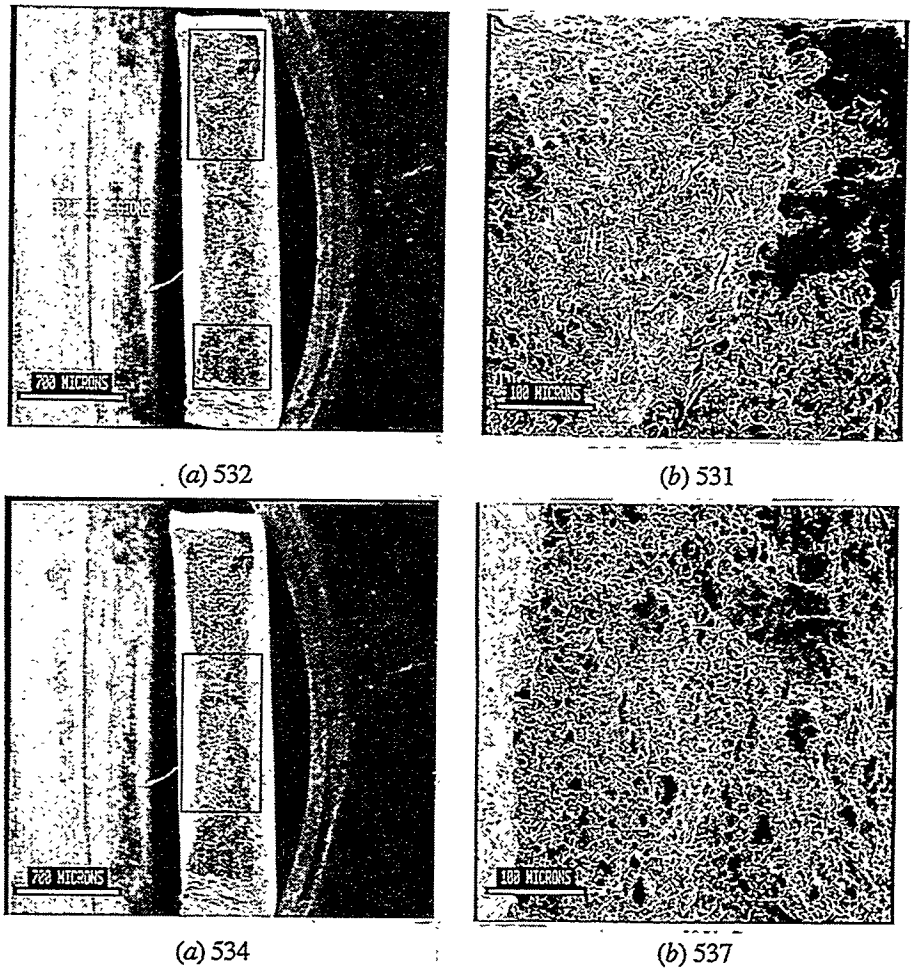

(*a*) 532 (*b*) 531

(*a*) 534 (*b*) 537

Fig. 9. Fracture surface of FAPY heat specimen 899-21690 in cold-worked condition tested at room temperature: (*a*) and (*b*) end location, and (*c*) and (*d*) midsection location.

3. Cold-rolled sheet: a mixed mode fracture consisting of brittle regions (cleavage) and a ductile region in the midsection of the tensile specimen.

The energy-dispersive X-ray spectra of the fracture surfaces showed little difference in composition for the three specimens.

SUMMARY AND CONCLUSIONS

Two commercial-size heats of the FAPY alloy were processed by AIM at Hoskins and one at United Defense. One ingot from each of the heats was sent to ORNL for processing, properties, and microstructural characterization. A 127-mm-long section was cut from each of the ingots. A 51-mm-thick slab section was cut from each of the 127-mm-long ingot sections for processing. The remaining ingot

section was used to machine specimens in the as-cast condition. The slab was forged and rolled to obtain a plate in the cast and hot-worked condition. Part of the hot-rolled plate was cold rolled into 0.76-mm-thick sheet to obtain a fine-grained wrought microstructure. Tensile tests were conducted from room temperature to 800°C on material in three different conditions. Tests were also conducted on a cast and hot-rolled bar processed at Hoskins. All of the materials were tested after annealing at 800°C for 1 h. One sheet was also tested in the 40% cold-worked condition. The as-cast, cast and hot-worked, and cold-rolled materials were characterized by optical and SEM. The following conclusions are drawn from this work:

1. The fine-grained sheet showed 20% elongation at room temperature. For cast and hot-worked conditions, 20% elongation as reached at 100°C. For the cast condition, the fine-grained sheet reached a value of only 10% at 200°C.
2. While the cast and cast and hot-worked conditions showed a transition from brittle-to-ductile behavior in tensile ductility, the cold-worked material showed only a reduction in ductility.
3. The cast grain size of 305 μm was refined to only 254 μm by hot-working. However, the cold-working refined the microstructure to 13 μm. The grain refinement occurs through recrystallization of warm- and cold-rolled sheet.
4. All three conditions showed the particles believed to be ZrC and FeCrAlY precipitates. Both particles were primarily at the grain boundaries in the as-cast condition. Processing by hot- and cold-working relocated the precipitates from the grain boundaries to matrix and refined their size. However, the total area fraction of the particles appears to remain the same in all three conditions.
5. Based on the ductility data, the fine-grained material can be cold-worked while the hot-worked material can be worked by warming up the work piece to ≥ 100°C.

ACKNOWLEDGMENTS

The authors thank D. C. Harper and K. S. Blakely for cutting and processing the ingots, H. F. Longmire for optical metallography, L. R. Walker for SEM work, C. A. Blue and D. J. Alexander for paper review, K. Spence for editing, and M. L. Atchley for preparing the manuscript.

Research sponsored by the U.S. Department of Energy, Office of Fossil Energy, Advanced Research and Technology Development Materials Program [DOE/FE AA 15 10 10 0, Work Breakdown Structure Element ORNL-2(H)], under contract DE-AC05-96OR22464 with Lockheed Martin Energy Research Corp.

MICROSTRUCTURAL AND MECHANICAL CHARACTERIZATION OF ALUMINA SCALES THERMALLY DEVELOPED ON IRON ALUMINIDE ALLOYS*

K. Natesan, K. L. Klug, D. Renusch, M. Grimsditch, and B. W. Veal
Argonne National Laboratory
Argonne, IL 60439

ABSTRACT

An understanding of the underlying phenomena when characterizing material performance requires knowledge in several areas, including the chemistry and physics of the early stages of oxidation, chemistry and bonding at the substrate/oxide interface, effect of segregants on the strength of bonding, transport processes through the scales that are formed during corrosion, mechanisms of residual stress generation and relief, and fracture behavior at the oxide/substrate interface. Specific objectives of the program described here are to (a) systematically investigate the relationships among substrate composition and properties and scale/coating adherence, damage tolerance, and micromechanical properties; (b) use results from the investigation to prevent scale/coating failure at elevated temperatures; and (c) identify conditions that lead to more damage-tolerant coatings and scales that are amenable to legitimate synthesis routes. The paper presents experimental data on microstructural characteristics of alumina scales that have been thermally developed on several Fe-based alumina-forming intermetallic alloys. In addition, adhesion data developed on the scales are presented, along with determinations of strain from data obtained by ruby fluorescence.

INTRODUCTION

Protection from corrosion and environmental effects arising from reactions with gases and condensed products is required to fully exploit the potential of advanced high-temperature materials designed to improve energy efficiency and minimize deleterious environmental impact. This protection is best afforded either by formation of stable surface oxides that are slow-growing, sound, and adherent to the substrate or by deposition of coatings that contain or develop oxides with similar characteristics. The benefits of certain alloying additions on the growth and adherence of protective oxide scales on metallic substrates are well known, but there remains the need for a detailed understanding of the mechanisms by which scale properties and coating integrity are improved by compositional, microstructural, and processing modifications. The ultimate objective of this program is to systematically generate a scientific basis for designing and synthesizing improved protective oxide scales/coatings (slow-growing, adherent, sound) on high-temperature materials without compromising the requisite properties of the bulk materials. Specific objectives are to (a) systematically investigate the relationships among substrate composition and properties and scale/coating adherence, damage tolerance, and micromechanical properties; (b) use such information to predict scale/coating failure; and (c) identify conditions that lead to more damage-tolerant coatings and scales that are amenable to legitimate synthesis routes. The objectives of the ANL program are to correlate actual oxidation performance with stresses, voids, segregants, interface roughness, initial stages of oxidation, and microstructures; study such behavior in growing or as-grown films; and define prescriptive design and synthesis routes to mechanically reliable surface oxides.[1,2] Several techniques are used in the studies, including Auger electron spectroscopy, X-ray diffraction, X-ray grazing incidence reflectance, grazing-angle

*Work supported by the U.S. Department of Energy, Office of Fossil Energy, Advanced Research and Technology Development Materials Program, Work Breakdown Structure Element ANL–4A and Basic Energy Sciences Materials Program, under Contract W–31–109–Eng–38.

X-ray fluorescence, optical fluorescence, and Raman spectroscopy. The project has selected Fe-25 wt.% Cr-20 wt.% Ni and Fe-Cr-Al alloys, which are chromia- and alumina-formers, respectively, for the studies. This paper presents selected results on alumina scale morphologies that develop on several Fe-Al based intermetallic alloys, their adhesion strength, and stresses in scales that can lead to spallation of the scales.

EXPERIMENTAL PROCEDURE

The experimental study has focused on iron aluminide (Fe-Al) intermetallic alloys, which are of interest for application in coal-gasification and coal-combustion systems. Iron aluminide alloys, which are alumina-formers, are in various stages of development under the sponsorship of the DOE. These alloys can be used as either structural material or cladding to protect structural material against corrosion. Sheets of several Fe_3Al-based alloys were procured from Oak Ridge National Laboratory. Table 1 lists the compositions of the alloys used in the study. Alloy FA 186 is a ternary alloy that contains Fe, Cr, and Al and is considered a base alloy. Alloy FA 129 is designed to exhibit high ductility at room temperature while retaining its strength at high temperatures, whereas FAL is designed for improved oxidation resistance through addition of Zr. Alloy FAS is designed to resist sulfidation, and FAX is designed for improved resistance in aqueous environments by deliberate addition of Mo. Coupon specimens were cut from sheet material for thermogravimetric oxidation experiments and for spectroscopic studies.

Specimens of the intermetallic alloys were oxidized at 1000°C for up to 100 h in oxygen bubbled through water at room temperature to examine the morphologies of the alumina scales that form on alloys with different bulk compositions. Thermogravimetric experiments were performed with an electrobalance having a sensitivity of 0.1 μg, to evaluate the rate of oxidation in different alloys and to establish the scaling kinetics. Specimens were suspended from the balance in a vertical furnace and held for the desired exposure period. Upon completion of the oxidation test, the furnace was opened and the specimens were rapidly cooled to room temperature. Following thermogravimetric measurement of oxidation, scale surfaces and cross sections of specimens were examined with a scanning electron microscope equipped with an energy-dispersive X-ray analyzer. Further, the oxidized specimens were cooled to liquid nitrogen temperature and fractured to examine the fracture morphologies of the scales and to evaluate the scale/metal interface.

A Sebastian-Five multipurpose tester (fromQuad Group Inc.) was used to evaluate the strength of the scale/substrate interface of each oxidized specimen. In this technique, an epoxy-coated pin is attached to the surface of interest at a temperature sufficient to cure the epoxy. The pin is subsequently separated from the sample at room temperature by applying a tensile load. Prior to testing the oxidized samples, the

Table 1. Nominal composition (wt.%) of alloys used in corrosion tests

Material	Cr	Al	Fe[a]	Other
FA 186	2.2	15.9	Bal.	-
FAS	2.2	15.9	Bal.	B 0.01
FA 129	5.5	15.9	Bal.	Nb 1.0, C 0.05
FAL	5.5	15.9	Bal.	Zr 0.1, B 0.05
FAX	5.5	15.9	Bal.	Nb 1.0, Mo 1.0, Zr 0.15, B 0.04

[a]Bal. = balance.

the procedure was evaluated using several flat unoxidized 316 stainless steel samples. This was done to establish the reliability of the technique and the absolute strength of the epoxy. In addition, epoxy-coated pins that had been at room temperature for varying lengths of time (as opposed to being in a freezer, where they are normally held) were used to evaluate the effect of this variable (room temperature degradation of the epoxy) on the strength data. Strength data from these tests were consistent; the maximum strength that could be measured by this procedure was ≈71±3 MPa. No significant variation in data was noted for pins exposed to room temperature for up to four days. Adhesion testing was then performed on each of the oxidized Fe-Al specimens.

The oxidized samples were also examined by a ruby luminescence at room temperature. By exploiting the strain dependence of the ruby fluorescence line, strains in the thermally grown oxides were determined for scales that developed on different substrates.[3,4] Fluorescence radiation from unstrained α-Al_2O_3, doped with Cr^{3+}, appears as a very sharp doublet, detectable at very low levels of Cr doping, with peaks at 14402 and 14432 cm^{-1}. The peak positions are strongly dependent on the state of strain in the sample but very weakly dependent on Cr concentration. Depending on scale-growth conditions, the doublet shifts and broadens, apparently as a consequence of varying strains in the alumina scale. The shifts provide a sensitive measure of strain accumulation in the scales and clearly indicate when strain relief occurs.

RESULTS AND DISCUSSION

Oxidation Behavior

Oxidation weight change of the intermetallic alloys was generally parabolic for ≈20 h, followed by much slower weight change for the rest of the exposure period. However, the scales in FA 186 and FAS exhibited significant spallation during oxidation at 1000°C and therefore, no weight change data could be obtained. For example, FA 186 showed a small weight gain up to 60 h of exposure, after which the weight of the sample decreased and showed a loss after 100 h of exposure. Assuming a parabolic behavior for the alloys with no spallation, rate constants calculated for FA 129, FAL, and FAX at 1000°C were 6.0×10^{-5}, 4.2×10^{-5}, and 4.2×10^{-5} $\mu g^2/mm^4 s$, respectively. X-ray diffraction data showed α-Al_2O_3 as the scale in all of the oxidized samples.

Microstructures of Oxide Scales

The surfaces of the oxidized samples were examined by scanning electron microscopy (SEM). Subsequently, the specimens were cooled to liquid nitrogen temperature and fractured. The freshly fractured surfaces of scale and substrate were then analyzed by SEM. Figures 1 and 2 show SEM photomicrographs of the fractured and oxidized surfaces of specimens. The fracture microphotograph of FA 186 shows a wavy oxide structure and the oxidized surface of the structure also indicates a fine distribution of oxide crystals or nodules. The fracture photomicrograph of the FAS specimen has an appearance similar to that of FA 186 but the surface shows a few large particles of oxide surrounded by a fine distribution of oxide precipitates. The morphologies in these specimens indicate that the scale is bonded to the substrate, probably at these large particles, and a two-dimensional bonding between the scale and substrate may not be present. In contrast, the fracture surface of the FA 129 alloy shows a dense, ≈2-μm-thick oxide scale, bonded well to the

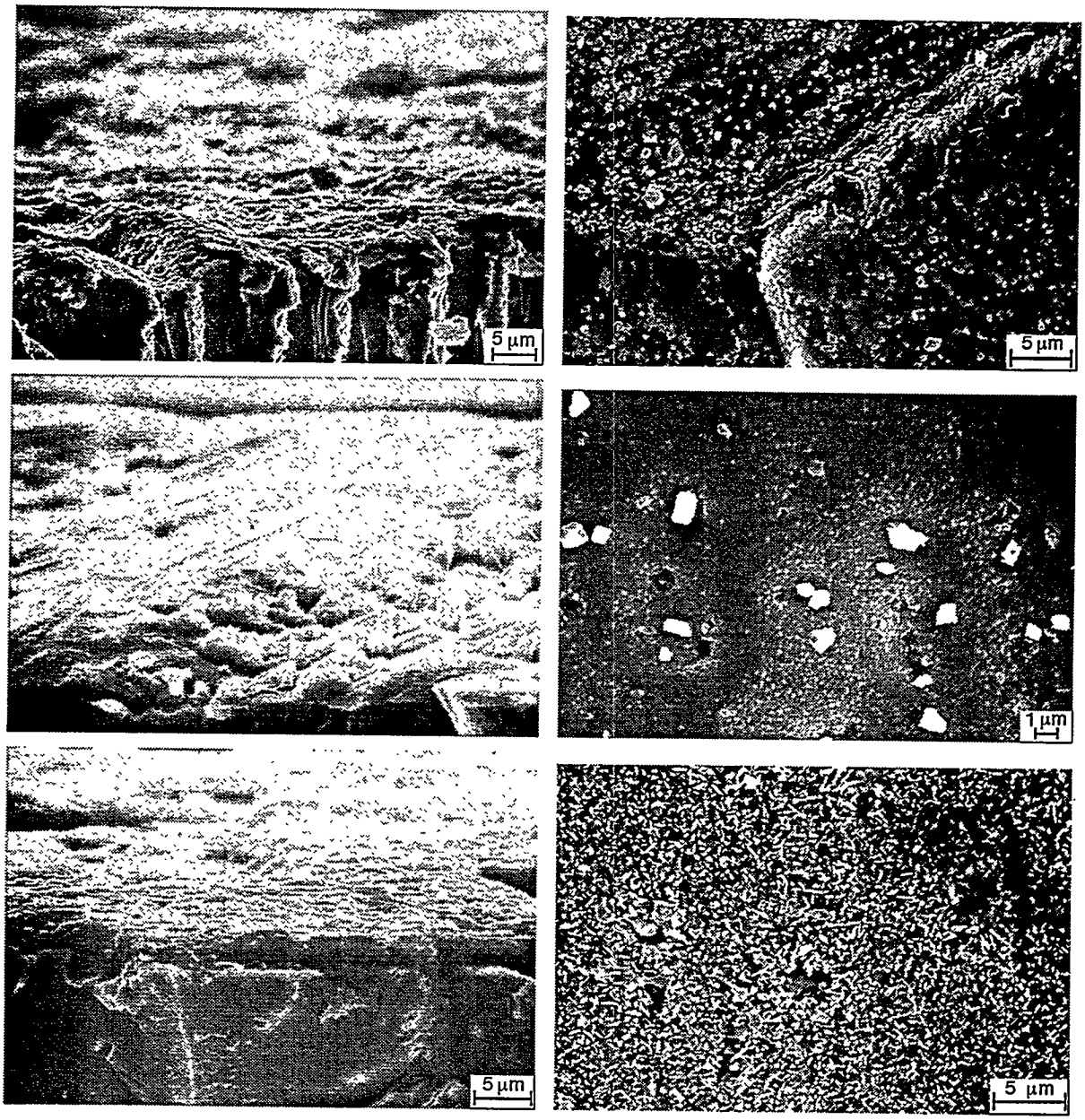

Fig. 1. SEM photomicrographs of (left) fracture surfaces and (right) oxidized surfaces of (top) FA 186, (middle) FAS, and (bottom) FA 129 alloys oxidized for 100 h at 1000°C

substrate. However, the surface of oxide exhibits some clumps of oxide, but not as many as in FAS alloy. The oxide morphology in FAL differs significantly from the morphologies of FA 186, FAS, and FA 129 alloys. Oxide growth is much more uniform and a distribution of fine oxide particles is present rather than spikes or clumps of oxide as observed in other samples. The oxide morphology in the FAX sample is much like that of the FAL sample but the fracture photomicrograph shows some voids at the scale/metal interface, which may be detrimental in the long run from an adhesion standpoint.

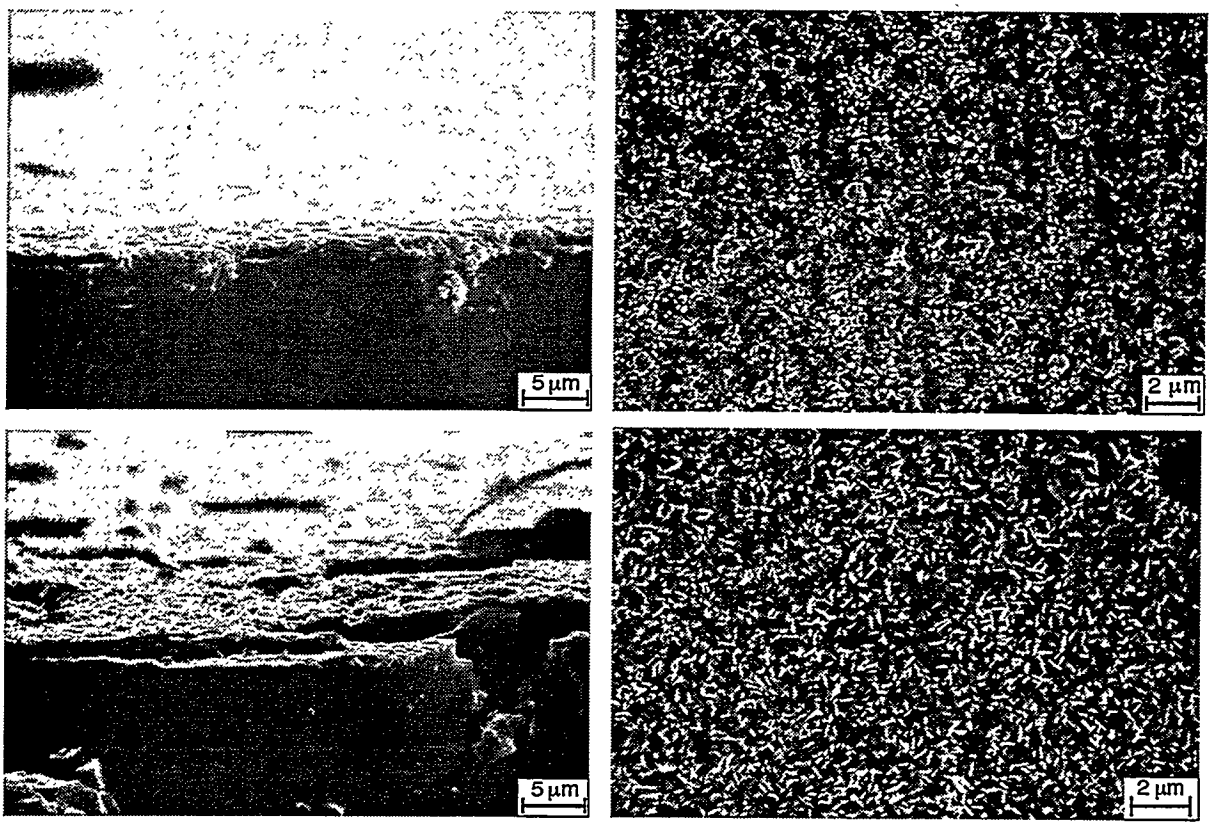

Fig. 2. SEM photomicrographs of (left) fracture surfaces and (right) oxidized surfaces of (top) FAL and (bottom) FAX alloys oxidized for 100 h at 1000°C

Adhesion of Scale to Substrate

To examine the adhesion characteristics of the thermally grown scales to the substrate, a Sebastian multipurpose tester was used to apply a tensile pull to separate the scale from the substrate. The surfaces of pulled pins were examined to assess whether the debonding occurred in the scale itself or at the scale/metal interface. Five measurements were taken for each specimen. The highest and lowest values for the load were discarded, and an average of the other three values and deviations from the mean were calculated. Knowing the pin area of contact, the stresses needed to pull the scale from the substrate were calculated. Figure 3 shows plots of the maximum stress endured by scale for the alloys oxidized at 800, 1000, and 1200°C as a function of alloy exposure temperature. The results show that Alloys FAS, FA 186, and FA 129 exhibit a peak in maximum stress value for specimens exposed at 1000°C. On the other hand, maximum stress values for FAL and FAX specimens are almost independent of exposure temperature. Even though the total exposure time of 100 h was used for all the specimens at all temperatures, the rates of disappearance of transient oxides and development of stable alumina scale will be different for different exposure temperatures and may be influenced by the composition of the bulk alloy, especially by the presence of reactive elements such as Zr and Nb.

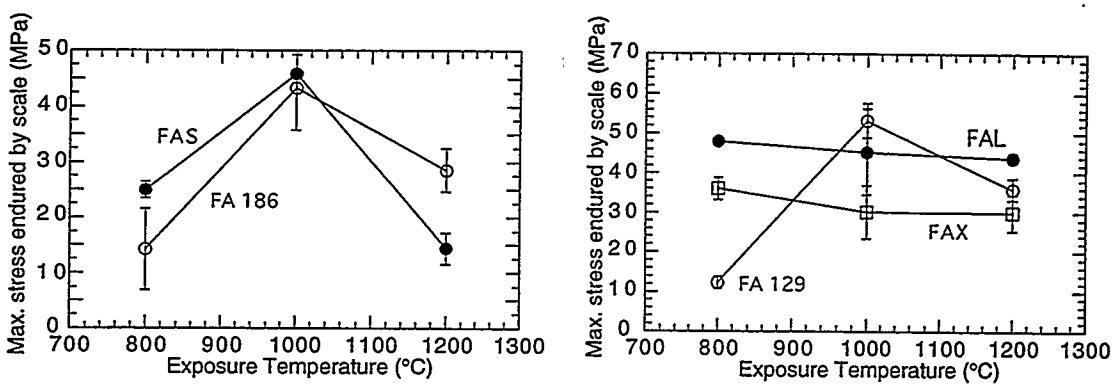

Fig. 3. Maximum sress endured by oxide scales on Fe-Al alloys determined by adhesion tests

Fluorescence Spectroscopy - Strain Analysis

Stress determination in thermally grown alumina scales by ruby luminescence has been recently addressed.[3,4] The technique has shown potential to elucidate our understanding of the strains that develop in thermally grown scales. The basic premise is that one can quantitatively assess the shift in the peaks of a relatively sharp fluorescence doublet obtained from the alumina scale, and, assuming a plane strain condition, calculate the strain in the scale. It is difficult to assess the importance of the measured strain values in scale fracture because little or no quantitative data are available for films of alumina in the literature. Nonetheless, the technique can be used to compare the strain values for specimens that have received differing treatment or compare the values obtained for different alloy specimens that have been oxidized under the same conditions. The trends identified in such an approach can shed light on the important variables responsible for the observed microstructure, alloying-element effect, adhesion, and time-dependent variations in the scale and at the scale/metal interface. The frequency shift ($\Delta\nu$ in cm^{-1}) is related to the in-plane strain by the expression

$$\Delta\nu = 2810\ \varepsilon_{in}.$$

Figure 4 shows the fluorescence spectra for various alloys oxidized for 100 h at 1000°C. The three spectra for each alloy are measurements taken at three different locations on the same specimen. The extreme variability in the spectra of FA 186 and FAS specimens indicates that the scale has spalled from various areas of the specimen. The spectra for FA 129, FAL, and FAX are fairly consistent. Figure 5 shows the in-plane strain, calculated from the peak shifts, for the five alloys oxidized for 100 h at 1000°C. The results show low strain values for FA 186 and FAS alloys, indicating significant spallation of the scale. This observation confirms the SEM analysis of the fracture surfaces and thermogravimetric test data for these alloys. The in-plane strain values for FA 129, FAL, and FAX are consistently high and indicate that the scales developed in these alloys can accommodate the deformation, as evidenced by the lack of spalling in the oxidized alloys.

A comparison of the stress needed to pull the scale away from substrate and the strain that was accommodated in the scale of various oxidized specimens is attempted in Fig. 6. It is evident that the maximum stress needed to pull the scale from various alloys is in the range of 30-52 MPa and the

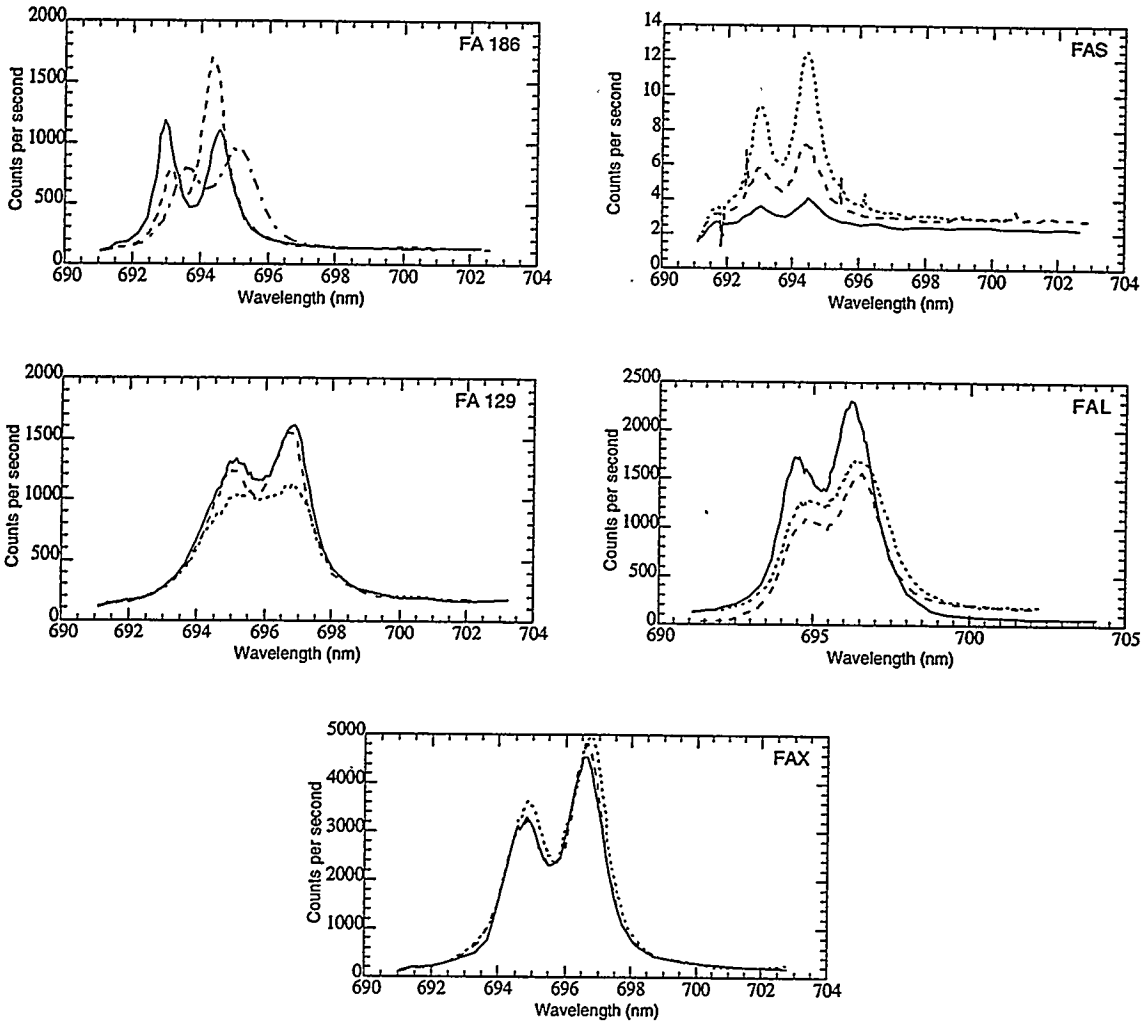

Fig. 4. "Ruby" fluorescence spectra for several Fe-Al alloys after oxidation for 100 h at 1000°C

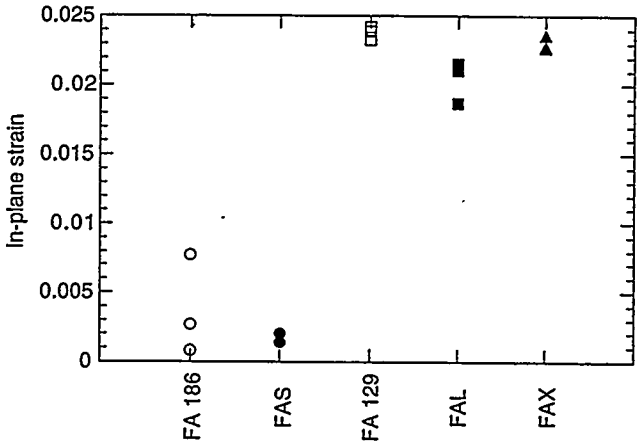

Fig. 5. In-plane strain values for oxide scales calculated from peak shifts in fluorescence spectra

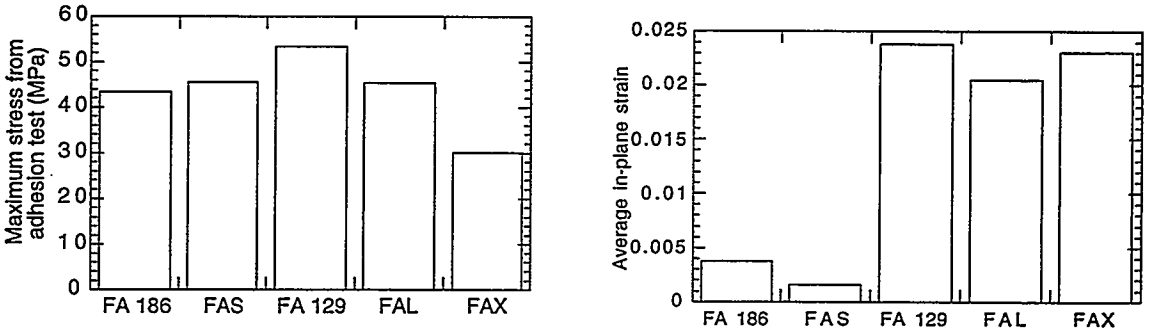

Fig. 6. Comparison of maximum stress needed to pull scale from substrate, and in-plane strain values for oxides that developed on several Fe-Al alloys

microstructural characteristics cannot be correlated with the stress values from the limited adhesion tests. Additional tests are underway with specimens exposed at 800 and 1200°C to develop a better understanding of scaling kinetics, adhesion of scale to substrate, and scale failure.

SUMMARY

Several alumina-forming Fe-Al intermetallic alloys have been oxidized in oxygen for 100 h at 1000°C to elucidate our understanding of the scaling kinetics, scale morphology, scale adhesion characteristics, and strain accommodation in the scales. Oxidation studies were conducted by the thermogravimetry technique, followed by detailed analyses of the surfaces of oxide scales. In addition, samples were cooled to liquid nitrogen temperature and then fractured; subsequently, their scale/metal interfaces were analyzed. Some of the scales were adhesion-tested by applying a tensile load to pull the scale away from the substrate. Finally, ruby fluorescence was used to measure in-plane strains in the oxide scales and the values were correlated with the scale microstructures.

REFERENCES

1. K. Natesan, B. W. Veal, M. Grimsditch, D. Renusch, and A. P. Paulikas, "Mechanically Reliable Surface Oxides for High-Temperature Corrosion Resistance," Proc. 9thAnnual Conf. on Fossil Energy Materials, CONF-9505204, ORNL/FMP-95/1, p. 225 (1995).

2. K. Natesan, C. Richier, B. W. Veal, M. Grimsditch, D. Renusch, and A. P. Paulikas, "Chemical and Microstructural Characterization of Thermally Grown Alumina Scales," Argonne National Laboratory Report ANL/FE-95/02 (1995).

3. D. Renusch, B. W. Veal, I. Koshelev, K. Natesan, M. Grimsditch, and P. Y. Hou, "Stress Determination in Thermally Grown Alumina Scales Using Ruby Luminescence," Proc. Spring Meeting of MRS Society, San Francisco, CA, April 8-12, 1996.

4. D. M. Lipkin and D. R. Clarke, "Measurement of the Stress in Oxide Scales Formed by Oxidation of Aluminum-Containing Alloys", Oxid. Metals (in press), and Q. Ma and D. R. Clarke, "Stress Measurement in Single and Polycrystalline Ceramics using Their Optical Fluorescence", J. Am. Ceram. Soc., 77 (2), 298-302 (1994).

OVERVIEW OF THE CARBON PRODUCTS CONSORTIUM (CPC)

Caulton L. Irwin (Carl)

Carbon Products Consortium
P.O. Box 6064
West Virginia University
Morgantown, WV 26506

ABSTRACT

The Carbon Products Consortium (CPC) is an industry, university, government cooperative research team which has evolved over the past seven years to produce and evaluate coal-derived feedstocks for carbon products. The members of the Carbon Products Consortium are UCAR Carbon Company, Koppers Industries, CONOCO, Aluminum Company of America, AMOCO Polymers, and West Virginia University. The Carbon and Insulation Materials Technology Group at Oak Ridge National Laboratory, Fiber Materials Inc., and BASF Corporation are affiliates of the CPC. The initial work on coal-derived nuclear graphites was supported by a grant to WVU, UCAR Carbon, and ORNL from the U.S. DOE New Production Reactor program. More recently, the CPC program has been supported through the Fossil Energy Materials program and through PETC's Liquefaction program. The coal processing technologies involve hydrogenation, extraction by solvents such as N-methyl pyrolidone and toluene, material blending, and calcination. The breadth of carbon science expertise and manufacturing capability available in the CPC enables it to address virtually all research and development issues of importance to the carbon products industry.

INTRODUCTION

Section 1304 of the National Energy Policy Act of 1992 authorizes a research and development program on non-fuel uses of coal. The objective is to develop coal-based feedstocks for a wide variety of materials and chemicals. The work of the CPC includes the production of high-value carbon materials from feedstocks derived from coal via solvent extraction and hydrogenation technologies. Tables 1 and 2 summarize the types of carbon products which are being developed by the CPC.

PARTICIPANTS

Figure 1 shows the feedstock and product linkages within the Carbon Products Consortium. A brief discussion of the CPC membership follows.

UCAR Carbon Company is the world's largest manufacturer of bulk carbon materials, with approximately one-third of the world's market in graphite electrodes, and has the broadest range of commercial carbon products of any domestic carbon company. UCAR is the only domestic carbon

Table 1. Feedstock and Product Summary for Intermediate Products.

Intermediate Products	Unit Price	Current Feedstock	Feedstock Status	Domestic Annual Sales	Worldwide Annual Sales	Comments
Binder Pitch	$300-$400 per ton	CTP from coke ovens	Declining supply of CT	500,000 T $175M	1,500,000 T $525M	SECP could replace CTP
Impregnating Pitch	$250-$350 per ton	PP (USA) CTP (elsewhere)	Adequate for demand	30,000 T $9M	125,000 T $37M	SECP could replace CTP and PP
Matrix Pitch (D)	$300-$400 per ton	75% CTP 25% PP	Declining supply of CT. PP quality declining			SECP could replace CTP and PP
Mesophase Pitch (D)	$10 per lb. (Japanese prices) No domestic price	PP (USA) CTP (Japan, Korea)	No CT mesophase pitch produced in USA	No domestic sales of mesophase CTP	Japanese production all used internally	SECP could replace CTP and PP
Calcined Coke	$250 per ton (calcined)	PT (USA) CT (Japan)	Declining quality. 4% annual increase in demand	2,000,000 T $300M	5,900,000 T $885M	SECP could replace CT and PT
Isotropic Coke	$150-$250 per ton	PT in USA CT in Japan		30,000 T $6M	100,000 T $20M	SECP could replace CT and PT
Needle Coke	$350-$600 per ton	PT in USA PT & CT in Japan		250,000 T $106, 250M	1,300,000T $552.5M	SECP could replace CT and PT

CT: coal tar
PT: petroleum tar
T: tons
D: dual use
CTP: coal tar pitch
PP: petroleum pitch
SECP: solvent extracted coal pitch

manufacturer that has developed technical expertise in raw materials for the complete scope of carbon products ranging from needle coke for electrodes, isotropic coke for specialty graphite, binder and impregnation pitches, active carbons, and pitches for high performance carbon fibers. UCAR would use precursors developed from coal extracts to produce carbon and graphite end-products. The availability of coal-based cokes with a controllable structure, would allow UCAR to customize graphite properties to fit desired market applications.

KOPPERS Industries is the largest domestic producer of binder for carbon and graphite used in the production of aluminum and in the production of steel by the electric arc process. The conventional feedstocks for binder pitch are crude tars produced as a by-product during coking of metallurgical coal.

Table 2. Feedstock and Product Summary for Final Products.

Final Products	Unit Price	Current Feedstock	Feedstock Status	Domestic Annual Sales	Worldwide Annual Sales	Comments
Carbon Anodes	$300-$400 per ton	Calcined coke binder pitch	Declining quality of petroleum coke	2,300,000 T $805M	6,900,000 T $2,415M	Alcoa has 32% of domestic market and 11% of world-wide market
Graphite Electrodes	$1 per lb.	Needle coke binder pitch impregnating pitch	Electrode Consumption cut in half over last decade	400,000 T $800 M	1,100,000 T $2,200M	UCAR has 1/3 of world market
Specialty Graphite (D)	$5-$50 per lb.	Cokes binder pitch impregnating pitch	Adequate	$0.2M	$0.6M	
Activated Carbon	$1-2 per lb. (avg) $80 per lb. (max) $0.20 per lb.(min)	Various organic precursors including coal and cellulostic material		146,000 T	375,000 T (excluding E. Europe and China)	China exporting up to 25,000 TPY
Carbon Fibers Low Cost CF	$10-$12 per lb. (isotropic)	70% PP 30% CTP (Japan)	Isotropic pitch fibers no longer produced in USA	150,000 lbs $1.65M 400,000 lbs	1,500,000 lbs $1.65M 650,000 lbs	CTP & SECP fibers show promise for advanced molecular sieves. SECP could replace CTP
High Performance CF (D)	$500-$3,000 per lb.	75% PP 25% CTP (Japan)	Only PP feedstocks available in USA from one source	$400M	$650M	SECP could replace CTP
Carbon-Carbon Composites (D)	$150-$2,000 per lb.	Carbon fibers & matrix pitch		$100M Brakes $ 50M Other		

Closure of by-product coke ovens has caused domestic production of coke and tar to decline at 3% to 4% per annum during the first half of the 1990s. By the year 2010, it is projected that domestic coal tar sourcing will have decreased 15% from today, crude petroleum will continue to increase in sulfur and metals, and pitch and coke supply requirements for carbon and graphite will increase by 100%. Therefore, Koppers is concerned about the United States retaining a dominant worldwide position in key industrial businesses such as aluminum and steel. Koppers' main objective for participating in the CPC is to develop dependable domestic coal-based raw materials for the production of binder pitches for aluminum cell anodes and commercial carbon and graphite products, impregnating pitches for commercial carbon, graphite and specialty materials; oils for wood treatment and carbon black production; feedstock for phthalic anhydride and other chemicals; and metallurgical and foundry grade

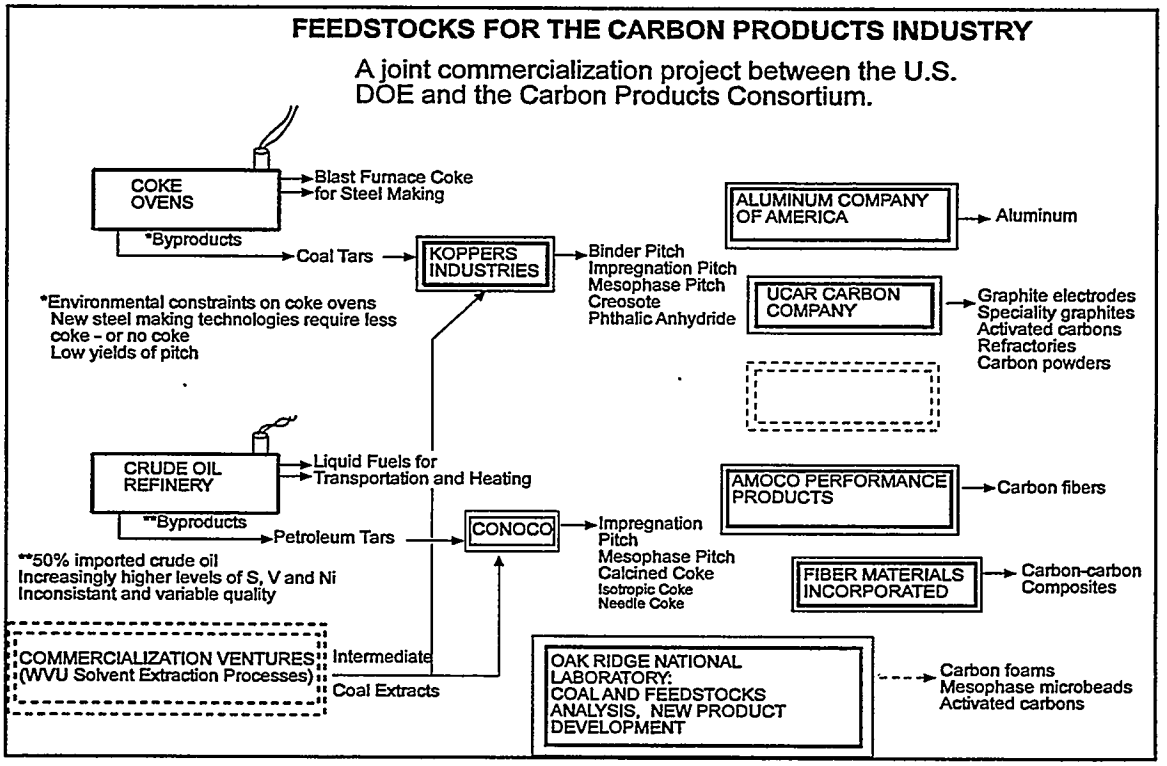

Figure 1. Feedstocks and Product Linkages within the Carbon Products Consortium.

cokes.

CONOCO is a fully integrated energy corporation with worldwide marketing and production facilities. Today, Conoco has annual worldwide petroleum coke sales in the 2-3 million ton range. Conoco coke is manufactured in five refineries located on three continents and a sixth refining/coking operation is under construction in Malaysia. Conoco is co-owner of a calcining plant in Moundsville, WV. In the petroleum coke area, Conoco is a world market leader, especially in regular coke for aluminum anodes and the TiO_2 process, and in specialty premium cokes for the graphite industry. Conoco's large, efficient manufacturing plants are technically supported from extensive Research and Engineering facilities in Ponca City, Oklahoma. Conoco believes that coal-based feedstocks being developed through CPC programs offer an abundant, promising alternate source of carbon products for the future.

ALCOA is the largest U.S. aluminum company with approximately one-third market share of the 4,600,000 tons per year domestic production. The aluminum industry is a major user of carbon since approximately 0.43 pounds of carbon are consumed in the production of one pound of aluminum. Reduction cell electrodes are produced from a baked coke and pitch mixture. The cokes and pitches are currently produced as by-products from coke ovens or from oil refining residues. Even a small improvement in carbon electrode quality for this very high volume, competitive industry would result in

considerable savings in aluminum manufacturing and electricity costs. Environmental pressures on coke ovens and the declining quality of imported crude oil (increased sulfur and metals content) have jeopardized existing raw material sources; therefore, ALCOA is highly interested in the development of consistent quality coal-derived carbon products that can improve electrodes and make production more efficient.

AMOCO Polymers has over 20 years experience in the development and commercial production of pitch based carbon fibers and is the only domestic producer of ultra-high thermal conductivity carbon fibers made from petroleum pitch. Ultra-high thermal conductivity carbon fiber and composites are the basis for components which offer unique performance advantages in the electronic packaging and spacecraft business areas. The combination of stiffness, strength, passive thermal management, dimensional stability, and machinability afford the potential to meet the thermal performance and reliability demands imposed by high density electronic packaging and small, high performance satellites. Hence, any innovations in high thermal conductivity carbon fibers directly impact both the commercial and defense industries. Mesophase pitch derived from coal affords AMOCO the opportunity to be more competitive through lower cost and higher quality. A domestic source for coal derived pitch serves defense interests and is consistent with reliability/robust processing goals. Coal-based materials should favorably impact processing costs since they are more graphitizable than petroleum pitches and afford fibers with better crystallinity. Thus, lower costs will result from less demanding furnacing (lower temperatures and shorter times) and improved product quality. Coal-derived precursors would be immediately employed for high thermal conductivity pitch fibers and materials. Cost and performance enhancements, linked with a secure source of raw materials and maintenance of an on-shore technology base, compel industrial and government support for this technology.

West Virginia University (WVU) coal processing technologies, developed in the Department of Chemical Engineering have been tested and proven over the past 10 years with support through the WVU Coal and Energy Research Program, the U.S. DOE's Consortium for Fossil Fuel Liquefaction Science, and the U.S. DOE's New Production Reactor Program. The work is currently supported through the U.S. DOE Advanced Research and Technology Development Materials Program and through PETC's Non Fuel Use of Coal Program. The main focus of the WVU program is to develop an economical process to obtain a high (50% to 80%) yield of ash-free coal-derived extract. The WVU process involves the use of a novel dipolar, aprotic solvent, N-methyl-2-pyrolidone (NMP) at a mild temperature of 202 deg C and one atmosphere pressure to extract organic coal material selectively and obtain an ultra low ash, low sulfur carbonaceous product. Hydrogenation of coal prior to extraction by NMP substantially increases the yield and alters properties of the extract. A flow chart indicating the three step solvent extraction process developed by WVU is shown in Figure 2. The WVU research team produces a wide

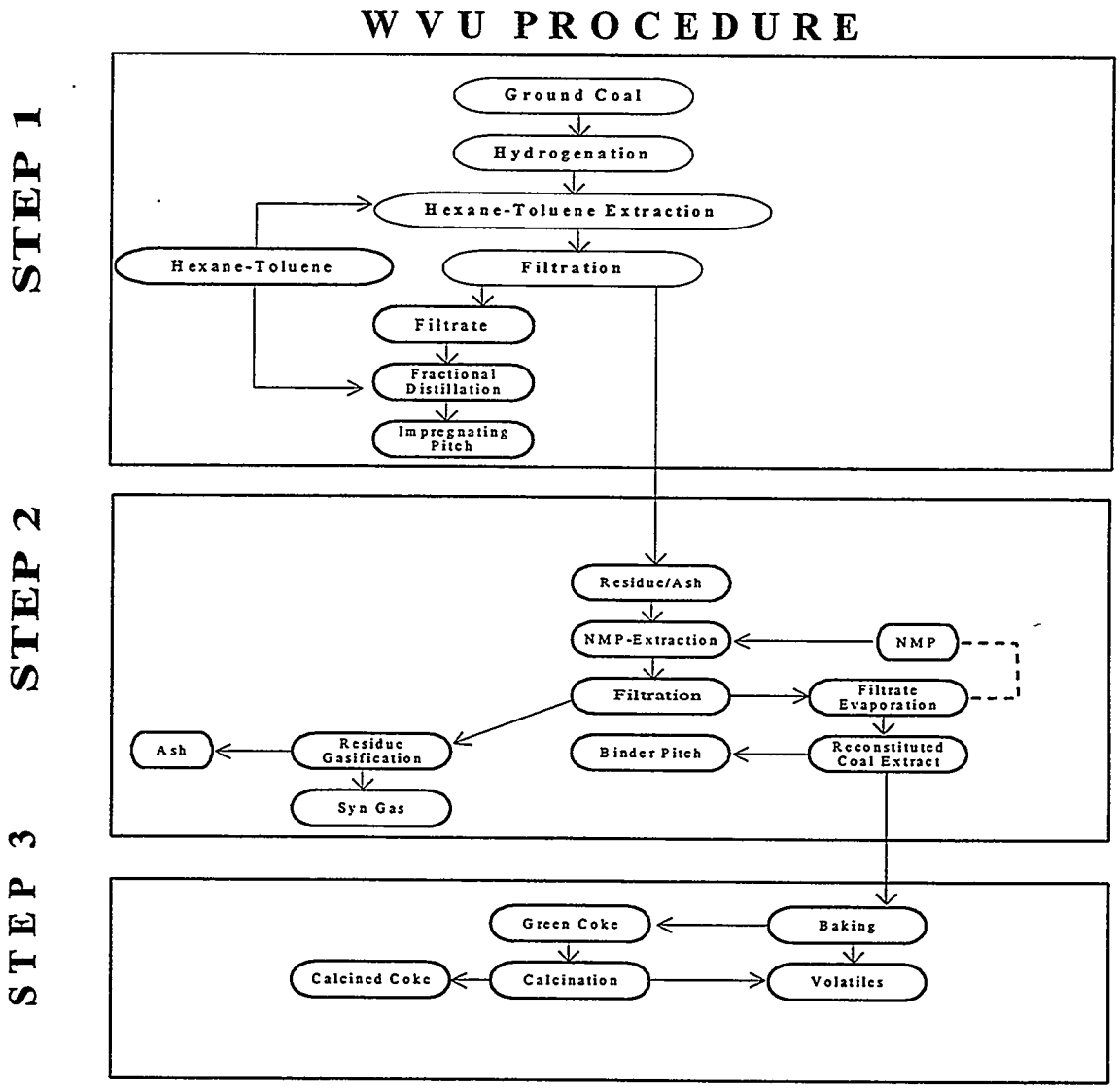

Figure 2. WVU Solvent Extraction Procedure

variety of coal extracts. The CPC industrial participants evaluate the suitability of the extracts as feedstocks for their particular product lines, and work with WVU to further optimize the process.

Fiber Materials Inc. (FMI) is a world leader in the manufacture of multidirectional carbon-carbon composites with over 25 years experience using both petroleum and coal tar pitches from companies such as Allied Signal, Ashland, and Koppers. FMI is the largest producer of pitch based carbon-carbon composites in the U.S. and has developed many specialized laboratories and processing techniques. The manufacture of carbon-carbon (C/C) composites for use in the defense industry has relied heavily on petroleum and coal-tar pitches as the matrix material. Over the past decade the properties of pitches have changed, resulting in changes to the composites fabricated. The reason is that

pitches come from the residual tars of other manufacturing processes (oil, gas and coke production). Process changes in manufacturing the primary products result in changes to the residual tars. In addition to defense, there are other new applications for C/C composites appearing in the commercial sector, including: biomedical, automotive, fusion and fission energy, and test equipment. It is important that the WVU process be put to practical use in the manufacture of composites for these new applications.

The Carbon and Insulation Materials Technology Group (CMT) at the Oak Ridge National Laboratory (ORNL) has extensive experience in the qualification of high performance graphite and carbon-carbon composite materials and products. ORNL houses many advanced materials testing facilities and CMT personnel have been involved with the analysis of coal structures for many years. The CMT group will develop relations between various coals and solvent extracted coal products and furthermore, is particularly interested in the development of monolithic carbon fiber composite molecular sieves for gas separations and heavy oil upgrading.

PROGRAMS

The CPC has conducted programs with several agencies and organizations. The participants involved in the project entitled, "Coal-based Nuclear Graphites for the New Production Gas Cooled Reactors", (DOE Grant No. DE-FG02-91NP00159) sponsored by U.S. DOE Office of New Production Reactors, included the West Virginia University Departments of Chemical Engineering, Physics, and Chemistry; West Virginia Geological and Economic Survey; UCAR Carbon Company; and the ORNL Carbon and Graphite Materials Group. The objective was to produce nuclear grade isotropic graphite from coal based feedstocks. During the course of the two and one half year project, UCAR produced 14 CTE graphite test bars using isotropic cokes obtained via the WVU coal extraction process. Conventional binder bitch was used in fabricating the CTE test bars. It was discovered during this project that by varying the extent of hydrogenation prior to extraction, the isotropy of the resultant graphite could be made to range from isotropic (CTE ~ 4.5x10-6) to anisotropic (CTE ~ 0.5x10-6). Prior to this project, domestic isotropic graphites had only been produced from petroleum cokes.

"Coal-based Precursors for Production of Carbon and Graphite Products", (DOE/PETC Contract No. DE-AC22-95PC94063) sponsored by U.S. DOE Fossil Energy Materials and Pittsburgh Energy Technology Center, initiated a three-phase project in partnership with the CPC to explore and develop the possibilities of making commercially acceptable carbon products from coal. The project is in part a response to a mandate of the National Energy Policy Act of 1992 that the country initiate programs involving research, development, demonstration, and commercial application of technologies for the nonfuel-use of coal rich resources in the United States.

The materials characterization shown in Tables 3 and 4 were developed by the industrial participants during the current U.S. DOE program. As part of this project, the MITRE Center for Environment,

Table 3. Comparison of WVU Coal Extract with Commercial Pitches

	WVU Extract	Coal Binder	Petroleum Impregnant
Softening Point (°C)	105	112	120
Modified Conradson Carbon (wt %)	53	58	52
Carbon (wt %)	88.9	93.8	91.5
Hydrogen (wt %)	5.85	3.92	5
Nitrogen (wt %)	2.2	0.7	0.6
Oxygen (wt %)	2.74	0.93	0.5
Sulfur (wt %)	0.45	0.56	2.5
Aromatic Hydrocarbon (%)	45	85	55
Molecular Weight	370	410	500

Table 4. Comparison of WVU Pitch with Commercial Impregnation Pitches

	WVU	Ashland A240	Allied 15V
Coking Value (wt %)	49.3	50.2	46.7
Ash Content (wt %)	0.02	0.03	0.17
Quinoline Insoluble (wt %)	0.39	0.15	4.3
Toluene Insoluble (wt %)	1.12	6.52	14.8
Sulfur (wt %)	0.4	2	0.54
Softening Point (°C)	117	117	88
Specific Gravity	1.22	1.26	1.28
Viscosity (sec)	****	16	19

Resources, and Space conducted a review and cost analysis of the WVU coal extraction process. Preliminary conclusions and recommendations include: (1) the extract is a suitable precursor for production of isotropic anode coke, (2) the product cost of the coal extract is estimated by MITRE to be

$77 per ton at a scale of 500,000 tons per year, and after further coking and calcining the estimated cost of calcined coke is $173 per ton, (3) it is extremely important that the unhydrogenated coal extract be further evaluated by the CPC for production of anode coke, (4) research on the production of isotropic carbon fibers ($8 to $10 per pound) from the coal extracts is recommended, and (5) it is recommended to examine the economics of dual production of both hydrotreated and unhydrotreated coal extracts simultaneously. Such an integrated process could be a significant process development for maximizing value added products from domestic coal.

As part of its DOE sponsored program, UCAR has recently produced an all coal-based CTE graphite test bar, i.e. the anistropic coke, binder and impregnation pitch were all derived from WVU coal extracts. Some properties of the test bar are shown in table 5.

Table 5. Properties of All Coal-Based CTE Graphite Test Bar.

CTE (10^{-6}/°C)	0.26
Specific Resistance (μohm-m)	9.55
Density	1.376

The CPC is co-organizer of a workshop entitled, "Applications of Carbon Products for Efficient Operation of Heavy Trucks, Buses, and Other Commercial Vehicles", (DOE Contract No. DE-AF05-96OR22500) sponsored by the U.S. DOE Office of Heavy Vehicle Technologies, which will be held on September 4 - 5, 1996. The objective of the workshop is to explore the various ways in which carbon products can improve productivity, safety, fuel efficiency, and cost effectiveness of heavy vehicle operations.

The CPC is pursuing the role of carbon products in the Industries of the Future program with the U.S. DOE Office of Industrial Technologies. Table 6 indicates some of the carbon products which have applications in the seven industries of the future.

The CPC in cooperation with the Pittsburgh Energy Technology Center is pursuing a coal refinery scheme which would co-produce advanced materials from coal and fuel for IGCC power plants. Figure 3 illustrates this coal refinery concept.

ACKNOWLEDGMENTS

The contributions of Irwin Lewis and John Chang of UCAR, Ron McHenry of KOPPERS, Ken Tucker and Gene Harlacher of CONOCO, David Belitskus of ALCOA, Mike Michno and Girish

Table 6. Role of Carbon Products in the U.S. DOE Industries of the Future

	Anodes	Electrodes	Molds	Crucibles	Heating Elements	Refractories	Filters	Catalysts Supports	Molecular Sieves	Fiber Reinforce-ments
Aluminum										
Steel										
Metal Casting										
Glass										
Chemicals										
Refining										
Forest Products										

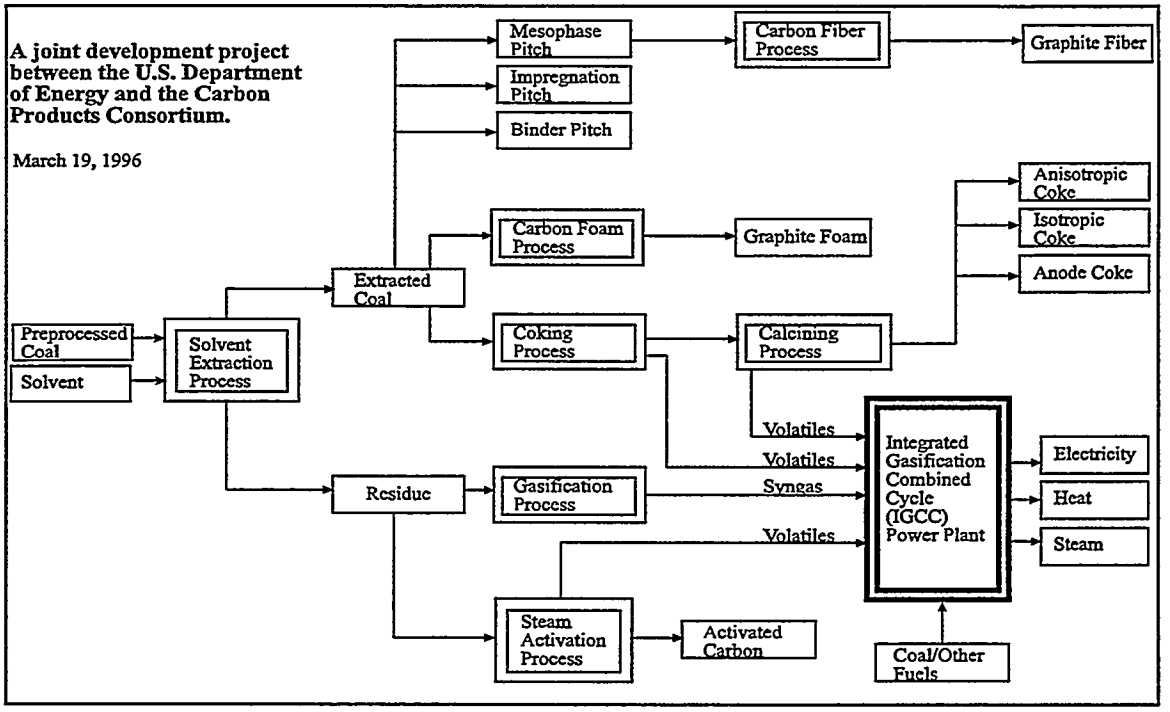

Figure 3. Coal Refinery Scheme To Co-Produce Carbon Products and Fuel for IGCC Power Plants

Deshpande of AMOCO, Cliff Baker of FMI, Tim Burchell of ORNL, and John Zondlo and Al Stiller of WVU to this article and to the CPC programs are gratefully acknowledged.